TECHNISCHE UNIVERSITÄT DRESDEN

Faculty of Civil Engineering Institute for Structural Analysis

Master's Thesis

MODELLING OF MECHANO-ELECTRIC FEEDBACK IN CARDIAC TISSUE

Yongjae Lee

Master's Thesis

Modelling of Mechano-electric Feedback in Cardiac Tissue

Modelling der elektromechanischen Reaktion in Herzgewebe

Yongjae Lee

Supervised by:
Univ.-Prof. Dr.-Ing. habil. Michael Kaliske
and
M.Sc. Barış Cansız

Submitted on June 4, 2018

TECHNISCHE UNIVERSITÄT DRESDEN

Faculty of Civil Engineering Institute for Structural Analysis

Conceptual Formulation of the Master Thesis MT04/17

Name: Yongjae Lee
Field of Study: ACCESS Master Course

Topic: **Modelling of Mechano-electric Feedback in Cardiac Tissue**
(Modelliering der elektromechanischen Reaktion in Herzgewebe)

Objective:

The human heart is one of the most studied organs of the body. This is due to the fact that failure of the heart is the number one cause of death in the developed countries. Any malfunctions might cause sudden death and understanding of the working mechanisms of the heart is a challenging task due to its complexity. On that account, the mathematical modelling of the heart can noninvasively assist cardiologists to develop effective and inexpensive personalized treatment techniques.

The pumping function of the heart arises as a result of the coupling between the electrical wave propagation and mechanical deformation. Both occurrences by themselves as well as their mutual interaction comprise a large research interest. The initiation and propagation of excitation waves are governed by opening and closing of ion channels located in the cell membrane. Ion transmission through the channels is initiated by depolarization of nearby cells. Additionally, these channels can be also activated upon mechanical deformation which is crucial for functioning of the heart. This phenomenon is known as mechano-electric feedback (MEF).

In this master thesis, we aim to develop more realistic MEF formulation in the light of physical observations. As a novel aspect, MEF will be reformulated by considering the strain rate along the fibre direction. Apart from the dependency on the fibre strain/strain rate, the contribution of the cross fibre strain will be also incorporated. We will further investigate the influence of MEF on regular cardiac activity and cardiac arrhythmias through finite element analysis of patient-specific bi-ventricular heart models. Morever, we will study 'Commotio cordis' which arises as a result of abnormal deformation of the heart resulting in ventricular fibrillation. In the simulations, electrocardiograms and left ventricular volume-time curves will be recorded. At the end, we will compare the results of existing MEF formulations in the literature with our novel approach.

Scientific consultant: M.Sc. Baris Cansiz Tel.: 0351-463 33234

DRESDEN concept

Date of issue: 09.02.2018

Date of submission: 11.06.2018

Univ.-Prof. Dr.-Ing. habil. Michael Kaliske
First examiner

Prof. Dr.-Ing. Wolfgang Graf
Second examiner

Declaration of originality

I confirm that this assignment is my own work and I have not sought or used inadmissible help of third parties to produce this work and I have clearly referenced all sources used in the work. I have fully referenced and used inverted commas for all text directly or indirectly quoted from a source.

This work has not yet been submitted to another examination institution – neither in Germany nor outside Germany – neither in the same nor in a similar way and has not yet been published.

Lee, Yongjae
Dresden, June 4, 2018

Abstract

The heart's pumping action can be successfully performed by the well-coordinated relationship between Excitation Contraction Coupling (ECC) by which electrical activation of cardiac cells triggers the mechanical contraction of heart and Mechano Electric Feedback (MEF), a mechanical alteration influences cardiac electrical activity. While ECC is rather well characterized, less is known about the cellular mechanisms of MEF. Nevertheless, the significance of MEF can't be disregarded. In the work, MEF is compuationally investigated in cell and organ scales by using the modified Hill model describing the orthotropic electro-visco-elastic respose of myocardium where the active (electrical) and mechanical (viscous and elastic) deformations were decomposed in a multiplicative format [1, 2]. At cell scale, it is reveald that MEF contributes to the synchronized contractions of the cardiac tissue by decreasing the dispersion of repolarization. Furthermore, as a novel aspect, the mathematical models of Stretch-Activated ion Channels (SACs) responsible for MEF are reformulated in terms of the strain rate along $\boldsymbol{f}$ ($\dot{\lambda}_{\mathrm{f}}$) and the stretch along $\boldsymbol{s}$ (λ_{s}). The influence on the biventricular heart model is studied with electrocardiogram (ECG) and volume-time curve (v-t curve) during normal cardiac cycles. It is observed that MEF is activated in the different area of the biventricular heart. Afterwards, Ventricular fibrillation (VF) due to "Commotio Cordis" and its termination by "Precordial Thump" are simulated. Finally, Premature Ventricular Contractions (PVCs) is simulated with the hemodynamical disturbance by using the left ventricular heart model. The adverse influence of the PVCs on the cardiac performance is studied and Postextrasystolic Potentiation (PESP) is detected during the PVCs.

Contents

1 Introduction

The heart is the most important component of our cardiovascular system in human body in terms of its anatomy and function. It consists of four different chambers responsible for receiving and pumping blood. The chambers to which blood entering are called atria and the other two chambers that pump blood around the body are called ventricles.

The pumping of the heart with the four chambers is the result of a synchronized contraction and relaxation of about 10 billion muscle cells called cardiomyocytes. They can be divided into several different types depending on their function, which is closely related to their anatomy. Also, the cardiomycytes consist of the various celluar components due to functional reasons. One of the significant components called intercalated discs has the specialized contacts with its neiboring cardiomyocytes which enables mechanical and electrical coupling by faciliating the cooperation between the cardiac cells. In order to contract, electrical activation is mandatory. Normally, the pacemaker cells located at the sinoatrial node (SA node) generate the electrical impulse travelling to His bundle through the atrioventricular node (AV node). Then, the wave is divided and travels to the right and left bundle branch connected to Purkinje fibers at which the velocity is four times faster than normal cardiac muscle cell. The conduction system makes it possible for synchronous and coordinated contractions. The heart is structurally and functionally a highly non-homogeneous, yet its main functions to circulate blood and nourish every single cell are achieved by relatively synchronous and coordinated contraction of the numerous ventricular cells [3]. Dyssynchronous contraction compromise the coordination required to eject blood efficiently, leading to reduced pump function and ultimately heart failure [4, 5, 6, 7].

In order to pump in the synchronized way, the proper relationship between cardiac electrophysiology and the mechanics is required [8, 9]. In case that the reciprocal action is hindered, cardiovascular diseases are caused such as arrhythmia, hypertrophy and acute myocardial infarction. According to Benjamin et al, [10], cardiovascular disease is the leading global cause of death, accounting for more than 17.9 million deaths in 2015, a number that is expected to grow to more than 23.6 million by 2030. Also, direct and indirect costs of total cardiovascular diseases and stroke are estimated to total more than $329.7 billion [10].

As mentioned, the pumping function of the heart arises as a result of the association between the electrical wave propagation and the mechanical deformation. These interactions operate with two-way coupling: ECC and MEF (see Figure 1.1). The mechanical contraction is due to the electrical activation through an intracellular calcium-dependent process in the sarcoplasmic reticulum, ECC [11, 12]. The reverse coupling between the cardiac mechanics and the electrophysiology is known as MEF that the electrophysiological changes may result from the regional mechanical stretch or global hemodynamic overload [3, 7, 13, 14].

MEF may have an important role in a normal regulation of the heart and the coordination of cardiomyocyte contraction. There are a few of ways to control the cardiac-electromechanical activity such as autonomic and hormonal mechanism. However the regulatory modulation that occurs within the heart itself are essential for a beat-by-beat adaptation

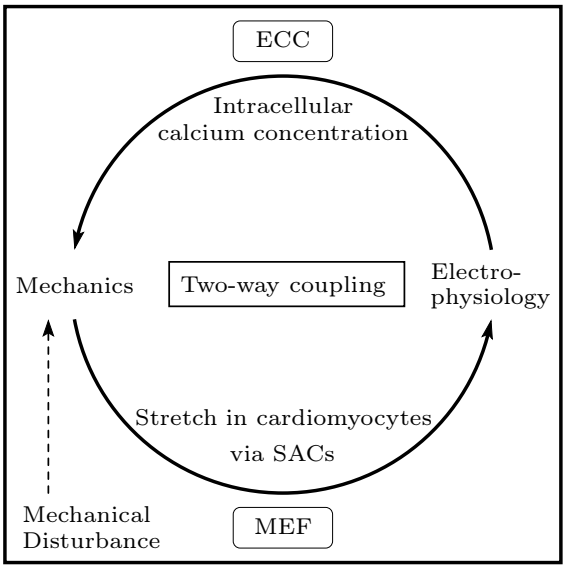

Figure 1.1: Conversion of mechanical change into an electrical change is decribed as a feedback return loop [9].

to changes in physiological demand, which can be attained by MEF [12, 15].

Apart from these positive findings, MEF and SACs also have the potential to disturb the cardiac rhythm in pathophysiological conditions. MEF has been considered as an important contributor to the increased risk of arrhythmia during the pathological conditions including heart failure [7, 16, 17]. Abnormal deformation may induce ventricular premature beats and fibrillations in an ischemic heart [18]. Moreover, even in the healthy heart a moderate precordial mechanical blow can cause sudden cardiac death in the absence of morphological damage, "Commotio cordis" [19, 20].

Nevertheless, the role of MEF at a physiological level is quite not clear. Although a lot of scientific work is devoted to understand the functioning mechanisms of MEF, they have not been fully revealed due to the complexity as well as the difficulties accompanying *in-vivo* experiment. The varying characteristics of the cardiac tissue within a mechanically and electrically dynamic environment also contribute to the unclearness. In this context, computational modelling of the cardiovascular system is particularly useful in quantifying results that are difficult or impossible to measure in *in-vivo* experiments [21]. Actually, computer simulations have gained increasing popularity and have the potential to visualise regional cardiac electrophysiology.

In this work, MEF is computationally investigated at cell and organ scale. To do so, the monodomain based finite element formulation for the coupled electromechanical heart tissue is adopted, which incorporates the modified Hill model that describes the electro-visco-elasticity of the myocardium at material level where the total deformation gradient is decomposed into the active part (electrical) and the mechanical part (viscous and elastic) [1, 2] for the rheology. In order to illustrate ventricular blood pressure, the surface element formulation accounting for the blood pressure evolution is incorporated into the finite element formulation. Afterwards, it is aimed at developing more realistic SACs models in view of physical observations. SACs are computed originally in terms of stretch along fiber direction (λ_f). Apart from the traditional SACs model, SACs models are newly reformulated in consideration of strain rate along fiber direction ($\dot{\lambda}_\mathrm{f}$) and stretch along cross fiber direction (λ_s). Furthermore, the simulations that adopt MEF with these different

SACs models are compared by using ECG and v-t curve. Since the SACs considering λ_{f} is proposed in [22, 23], relatively recent studies report that the effect of MEF is also dependent on the velocity at which stretch is applied. The biventricular heart model also gives the validity to the MEF reformulations in which SACs consider $\dot{\lambda}_{\mathrm{f}}$ and λ_{s} because the regions under tension are not consistent with the regions experiencing positive $\dot{\lambda}_{\mathrm{f}}$ as well as the regions with compressive λ_{s}. The inconsistencies may cause the MEF effect to be activated in the different region, which consequently alters the electrophysiology of the heart model. Subsequently, a moderate mechanical loading on the biventricular heart and a transiently increased hemodynamic loading in the left ventricular heart model are simulated in order to see how the mechanical disturabances in the heart affect its electrical domain. The former interrupts the cardiac electrophysiology, and consequently, results in the arrhythmia and the ventricular fibrillation due to MEF effect. The latter also interrupts the electrophysiology and causes the premature ventricular contraction (PVCs) with the malfunctioned cardiac pumping.

The outline of the thesis is as follows. Chapter 2 presents the governing equations of the electromechanics of the heart and the linearization of the governing equations with finite element formulation of coupled problem that includes the deformation dependent traction term. Chapter 3 explains the constitutive equations of the two field variables with its sensitivities. Also, the reformulated SACs models are suggested. Chapter 4 introduces the numerical examples to reveal MEF effect on the heart by using the adopted FEM model and the constitutive equations. Firstly, it is investigated that how MEF affect the AP in the small cardiac tissue bar with the assumption that MEF contributes to the cardiac electrophysiology and plays a important role in the coordinated contraction of the tissue. The simulations are carried out using different material properties (elastic and viscoelastic) and the different level of discretization. Next, the regular normal cycles using the biventricular heart model are simulated with the newly suggested SACs model and in order to observe how the suggested SACs models influence differently on the biventricular heart. Also, in order to investigate the role of MEF in the normal healthy heart under pathological condition, the ventricular fibrillation is simulated by applying the morderate mechanical impact on the heart "Commotio cordis". The termination of fibrillation "Precordial thump" is subsequently simulated as well. In the example using left ventricular heart model, the influence of hemodynamical disturbances on the cardiac performance is investigated. ECGs and v-t curves are recored during all the simulations using the heart model . PV curves are additionally recorded in the left ventricular heart simulation.

2 The finite element approximation of cardiac electromechanics

In this section, the fundamental equations of the coupled problem of cardiac electromechanics are introduced. Subsequently, the weak integral forms of the non-linear governing equations are constructed and linearized consistently by employing a conventional Galerkin procedure. Each weak form is linearized along its own variable, the placement field $\boldsymbol{\varphi}(\boldsymbol{X}, t)$ and the transmembrane potential $\Phi(\boldsymbol{X}, t)$ for the cardiac electrophysiology. Then, we make use of isoparametric shape functions for the discretization of the two field variables, so that the non-linear weighted residual equations in integral form are converted to a set of coupled and discretized algebraic equations.

2.1 Fundamental equations

A equilibrium state of the continuum body can be expressed by the conservation of linear momentum

$$J \operatorname{div}\left[J^{-1}\hat{\boldsymbol{\tau}}\right] + \boldsymbol{b} = \boldsymbol{0} \quad \text{in } \mathcal{B} \tag{2.1}$$

in terms of the Kirchhoff stress tensor $\hat{\boldsymbol{\tau}}$ and the volume-specific body forces $\boldsymbol{b}$ in the reference configuration, respectively. Note that the balance of linear momentum depends non-linearly on the primary field variables through the Kirchhoff stress tensor $\hat{\boldsymbol{\tau}}$. The balance of linear momentum has the essential boundary condition

$$\boldsymbol{\varphi} = \bar{\boldsymbol{\varphi}} \quad \text{on } \mathcal{S}_{\varphi} \tag{2.2}$$

and the natural boundary conditions

$$\boldsymbol{t} = \bar{\boldsymbol{t}} \quad \text{on } \mathcal{S}_t \quad \text{and} \quad \boldsymbol{t} = -\hat{\boldsymbol{p}}_{\mathrm{i}}(\boldsymbol{\varphi}) \quad \text{on } \mathcal{S}_{\mathrm{it}} \tag{2.3}$$

where the surface stress traction vector $\boldsymbol{t}$ is expressed by using the Cauchy stress theorem as $\bar{\boldsymbol{t}} \coloneqq J^{-1}\hat{\boldsymbol{\tau}} \cdot \boldsymbol{n}$ and the subscript i designates left ventricle (LV) or right ventricle (RV), $\mathrm{i} = \{\mathrm{lv}, \mathrm{rv}\}$. The former traction term is prescribed while the latter one depends on the deformation field and describres the load on the endocardial surface $\mathcal{S}_{\mathrm{en}}$ due to the blood pressure in the ventricular cavities during the cardiac cycle. Furthermore, the following relations are established: $\mathcal{S}_{\mathrm{en}} \subset \mathcal{S}$ and $\mathcal{S}_{\mathrm{en}} = \mathcal{S}_{\mathrm{lv}} \cup \mathcal{S}_{\mathrm{rv}}$. Therein, $\mathcal{S}_{\mathrm{lv}}$ and $\mathcal{S}_{\mathrm{rv}}$ mean the LV and RV endocardial surfaces, respectively. The expressions $\mathcal{S} = \mathcal{S}_{\varphi} \cup \mathcal{S}_t$ and $\mathcal{S}_{\varphi} \cap \mathcal{S}_t = \emptyset$ required to be satisfied by the surface subdomains. Additionally, the phenomenological excitation equation for the potential difference between intracelluar domain and the extracelluar domain within a monodomain setting is introduced as

$$\dot{\Phi} = J \operatorname{div}\left[J^{-1}\hat{\boldsymbol{q}}\right] + \hat{F}^{\phi} \quad \text{in } \mathcal{B} \tag{2.4}$$

where $J \operatorname{div}\left[J^{-1}\hat{\boldsymbol{q}}\right]$ is diffusion term by means of the flux vector $\hat{\boldsymbol{q}}$ to describe the propagating polarization waves and $\hat{F}^{\phi}$ is the non-linear source term. Similar to the balance of

linear momentum, the governing equation of the cardiac electrophysiology is subjected to the essential and natural boundary conditions

$$\Phi = \bar{\Phi} \quad \text{on } \mathcal{S}_\phi \quad \text{and} \quad q = \bar{q} \quad \text{on } \mathcal{S}_q \tag{2.5}$$

with complementary characteristics $\mathcal{S} = \mathcal{S}_\phi \cup \mathcal{S}_q$ and disjoint characteristics $\mathcal{S}_\phi \cap \mathcal{S}_q = \emptyset$ of the subdomains. The electrical surface flux term q and the spatial flux vector $\hat{\boldsymbol{q}}$ are linked through tge Cauchy-type formular $\bar{q} \coloneqq J^{-1}\hat{\boldsymbol{q}} \cdot \boldsymbol{n}$. Furthermore, the solution of the ordinary differential equation represented in Equation (2.4) requires the initial transmembrane potential value of material points at an initial state ($t = t_0$)

$$\Phi_0 = \Phi(X, t_0) \quad \text{in } \mathcal{B}. \tag{2.6}$$

2.2 The weak integral forms

To construct the weak forms of the strong forms in Equation (2.1) and in Equation (2.4), the conventional Galerkin method is applied. The weighted residual equations are achieved by multiplying the square integrable weight functions $\delta\boldsymbol{\varphi}$ and $\delta\Phi$. These two weight functions vanish at the essential boundaries $\delta\boldsymbol{\varphi} = \boldsymbol{0}$ and $\delta\Phi = 0$. Then, the weight residual equations are integrated over the domain of interest and the integration by parts is executed to obtain the following non-linear weighted residual expressions as

$$\begin{aligned}
G^{\boldsymbol{\varphi}}(\delta\boldsymbol{\varphi}, \boldsymbol{\varphi}, \Phi) &\coloneqq \int_{\mathcal{B}} \nabla\delta\boldsymbol{\varphi} : \hat{\boldsymbol{\tau}}\, dV - \int_{\mathcal{B}} \delta\boldsymbol{\varphi} \cdot \boldsymbol{b}\, dV - \int_{\mathcal{S}_t} \delta\boldsymbol{\varphi} \cdot \bar{\boldsymbol{t}}\, da - \sum_{\mathrm{i=lv,rv}} \int_{\mathcal{S}_{\mathrm{it}}} \delta\boldsymbol{\varphi} \cdot -\hat{\boldsymbol{p}}_{\mathrm{i}}\, da = 0, \\
G^{\phi}(\delta\Phi, \boldsymbol{\varphi}, \Phi) &\coloneqq \int_{\mathcal{B}} (\delta\Phi\, \dot{\Phi} + \nabla\delta\,\Phi \cdot \hat{\boldsymbol{q}}) dV - \int_{\mathcal{B}} \delta\Phi\, \hat{F}^{\phi}\, dV - \int_{\mathcal{S}_q} \delta\Phi\, \bar{q}\, da = 0,
\end{aligned} \tag{2.7}$$

where $\hat{\boldsymbol{p}}_{\mathrm{i}}$ designates the pressure applying on the endocardial surface walls. The terms responsible for internal response of body have positive sign, whereas the terms for external effects are indicated with negative sign. All the external source terms, such as the body force $\boldsymbol{b}$, the traction $\bar{\boldsymbol{t}}$, and surface flux terms $\bar{q}$ are prescribed, except the electrical source term $\hat{F}^{\phi}$ which is dependent on the field variables. Additionally, a non-conservative pressure load $\hat{\boldsymbol{p}}_{\mathrm{i}}(\boldsymbol{\varphi}) = \hat{p}_{\mathrm{i}}\boldsymbol{n}$ acting on the endocardial surfaces, where both components $\hat{p}_{\mathrm{i}}$ and $\boldsymbol{n}$ are determined rigorously by the deformation state of the ventricles. Now, the aim is to modify the non-linear residual equation represented in Equation (2.7) to equations consisting of linear terms with increments of the field variables $\Delta\boldsymbol{\varphi}$ and $\Delta\Phi$ at an equilibrium state $\boldsymbol{\varphi} = \tilde{\boldsymbol{\varphi}}$ and $\Phi = \tilde{\Phi}$. For this purpose, by taking advantage of the directional derivative of Equation $(2.7)_1$ along the increment $\Delta\boldsymbol{\varphi}$ and Equation $(2.7)_2$ along the increment $\Delta\Phi$, the linearized forms are obtained as

$$\begin{aligned}
L[G^{\boldsymbol{\varphi}}](\delta\boldsymbol{\varphi}, \tilde{\boldsymbol{\varphi}}, \tilde{\boldsymbol{\varphi}}, \Delta\boldsymbol{\varphi}) &\coloneqq G^{\boldsymbol{\varphi}}(\delta\boldsymbol{\varphi}, \tilde{\boldsymbol{\varphi}}, \tilde{\Phi}) + \Delta G^{\boldsymbol{\varphi}}(\delta\boldsymbol{\varphi}, \tilde{\boldsymbol{\varphi}}, \tilde{\Phi}, \Delta\boldsymbol{\varphi}) = 0, \\
L[G^{\phi}](\delta\Phi, \tilde{\boldsymbol{\varphi}}, \tilde{\Phi}, \Delta\Phi) &\coloneqq G^{\phi}(\delta\Phi, \tilde{\boldsymbol{\varphi}}, \tilde{\Phi}) + \Delta G^{\phi}(\delta\Phi, \tilde{\boldsymbol{\varphi}}, \tilde{\Phi}, \Delta\Phi) = 0,
\end{aligned} \tag{2.8}$$

where

$$\begin{aligned}
\Delta G^{\boldsymbol{\varphi}}(\delta\boldsymbol{\varphi}, \tilde{\boldsymbol{\varphi}}, \tilde{\Phi}, \Delta\boldsymbol{\varphi}) &= D[G^{\boldsymbol{\varphi}}](\delta\boldsymbol{\varphi}, \tilde{\boldsymbol{\varphi}}, \tilde{\Phi}) \cdot \Delta\boldsymbol{\varphi}, \\
\Delta G^{\phi}(\delta\Phi, \tilde{\boldsymbol{\varphi}}, \tilde{\Phi}, \Delta\Phi) &= D[G^{\phi}](\delta\Phi, \tilde{\boldsymbol{\varphi}}, \tilde{\Phi}) \cdot \Delta\Phi.
\end{aligned} \tag{2.9}$$

L and D allocate the linearization and directional derivative of the residual quantities, respectively.

2.3 Linearization in the solid domain

Firstly, the incremental form of the non-linear gradient term in Equation $(2.7)_1$ is derived as

$$\Delta\nabla\delta\boldsymbol{\varphi} = -\nabla\delta\boldsymbol{\varphi}\nabla\Delta\boldsymbol{\varphi} \tag{2.10}$$

where the two following correlations are exploited

$$\nabla\delta\boldsymbol{\varphi} = \nabla_{\boldsymbol{X}}\delta\boldsymbol{\varphi}\boldsymbol{F}^{-1} \quad \text{and} \quad \Delta\boldsymbol{F}^{-1} = -\boldsymbol{F}^{-1}\nabla\Delta\boldsymbol{\varphi}. \tag{2.11}$$

Furthermore, the objective Lie derivative of the Kirchhoff stresses $\mathscr{L}_{\Delta\boldsymbol{\varphi}}\hat{\boldsymbol{\tau}}$ and the current metric $\mathscr{L}_{\Delta\boldsymbol{\varphi}}\hat{\mathbf{g}}$ along the increment $\Delta\boldsymbol{\varphi}$ are considered as

$$\mathscr{L}_{\Delta\boldsymbol{\varphi}}\hat{\boldsymbol{\tau}} = 2\partial_{\mathbf{g}}\hat{\boldsymbol{\tau}} : \frac{1}{2}\mathscr{L}_{\Delta\boldsymbol{\varphi}}\mathbf{g} \quad \text{and} \quad \mathscr{L}_{\Delta\boldsymbol{\varphi}}\mathbf{g} = \mathbf{g}\nabla\Delta\boldsymbol{\varphi} + (\nabla\Delta\boldsymbol{\varphi})^{\top}\mathbf{g}\,. \tag{2.12}$$

Then, linearization of the Kirchhoff stresses can be obtained as follows

$$\Delta\hat{\boldsymbol{\tau}} = \mathbb{C}^{\boldsymbol{\varphi}\boldsymbol{\varphi}} : \mathbf{g}\nabla\Delta\boldsymbol{\varphi} + \nabla\Delta\boldsymbol{\varphi}\,\hat{\boldsymbol{\tau}} + \hat{\boldsymbol{\tau}}(\nabla\Delta\boldsymbol{\varphi})^{\top} \tag{2.13}$$

where the tangent moduli $\mathbb{C}^{\boldsymbol{\varphi}\boldsymbol{\varphi}}$ is defined as

$$\mathbb{C}^{\boldsymbol{\varphi}\boldsymbol{\varphi}} \coloneqq 2\partial_{\mathbf{g}}\hat{\boldsymbol{\tau}}. \tag{2.14}$$

Now, the second residual expression Equation $(2.7)_2$ is linearizd by deriving the incremental form of the non-linear gradient term in similar way to Equation (2.10)

$$\Delta\nabla\delta\Phi = -\nabla\delta\Phi\,\nabla\Delta\boldsymbol{\varphi}. \tag{2.15}$$

In similar manner, the Lie derivative of the electrical flux vector $\hat{\boldsymbol{q}}$ in the contravariant space is derived

$$\mathscr{L}_{\Delta\boldsymbol{\varphi}}\hat{\boldsymbol{q}} = 2\frac{\partial\hat{\boldsymbol{q}}}{\partial\mathbf{g}} : \frac{1}{2}\mathscr{L}_{\Delta\boldsymbol{\varphi}}\mathbf{g}\,. \tag{2.16}$$

Then, the increment of the electrical flux term can be obtained as

$$\Delta\hat{\boldsymbol{q}} = \boldsymbol{D}\cdot\nabla\Delta\Phi, \tag{2.17}$$

where the conduction tensor is defined as $\boldsymbol{D} \coloneqq \partial_{\nabla\Phi}\,\hat{\boldsymbol{q}}$. In order to achieve Equation $(2.9)_2$, the electrical source term $\hat{F}^{\phi}$ is linearized. Straightforwardly, the incremental form of $\hat{F}^{\phi}$ and the sensitivity with respect to the electrical field are calculated as

$$\Delta\hat{F}^{\phi} = H\Delta\Phi \quad \text{with} \quad H = \partial_{\Phi}\hat{F}^{\phi}. \tag{2.18}$$

2.4 Linearization in the surface domain

Furthermore, the deformation dependent traction term in Equation $(2.7)_1$ is linearized. In order to clarify the derivations, the term is written in different way as

$$\int_{\mathcal{S}_{\mathrm{it}}} \delta\boldsymbol{\varphi}\cdot\hat{p}_{\mathrm{i}}\,\boldsymbol{n}\,da = \int_{\bar{\mathcal{S}}_{\mathrm{it}}} \delta\boldsymbol{\varphi}\cdot\hat{p}_{\mathrm{i}}\,\boldsymbol{n}^{*}dA \quad \text{with} \quad \boldsymbol{n}^{*} \coloneqq \boldsymbol{n}\frac{da}{dA} = J\boldsymbol{F}^{-\top}\boldsymbol{N}, \tag{2.19}$$

for i = lv,rv. The subscript t is dropped for a simplified notation. It is assumed that the pressure load $\hat{p}_{\mathrm{i}}$ is dependent on the cavity volume of the ventricles $\mathcal{V}_{\mathrm{i}}$,

$$p_{\mathrm{i}} = \hat{p}_{\mathrm{i}}(\mathcal{V}) \quad \text{with} \quad \mathcal{V}_{\mathrm{i}} \coloneqq \frac{1}{3}\int_{\bar{\mathcal{S}}_{\mathrm{i}}} \boldsymbol{\varphi}\cdot\boldsymbol{n}^{*}dA. \tag{2.20}$$

The incremental form of Equation (2.20) is achieved as

$$\Delta\hat{p}_{\mathrm{i}} = \frac{\hat{p}_{\mathrm{i}}^{'}}{3}\int_{\bar{\mathcal{S}}_{\mathrm{i}}} (\boldsymbol{n}^{*}\cdot\Delta\boldsymbol{\varphi} + \boldsymbol{\varphi}\cdot\Delta\boldsymbol{n}^{*})\, dA \quad \text{with} \quad \hat{p}_{\mathrm{i}}^{'} = \frac{\partial\hat{p}_{\mathrm{i}}}{\partial\mathcal{V}_{\mathrm{i}}}. \tag{2.21}$$

Linearization of the covariant vector $\boldsymbol{n}^{*}$ is obtained by the objective Lie derivative $\mathscr{L}_{\Delta\boldsymbol{\varphi}}\boldsymbol{n}^{*}$ along the increment $\Delta\boldsymbol{\varphi}$,

$$\mathscr{L}_{\Delta\boldsymbol{\varphi}}\boldsymbol{n}^{*} = 2\frac{\partial\boldsymbol{n}^{*}}{\partial\mathbf{g}} : \frac{1}{2}\mathscr{L}_{\Delta\boldsymbol{\varphi}}\mathbf{g} = \Delta\boldsymbol{n}^{*} + (\nabla\Delta\boldsymbol{\varphi})^{\top}\boldsymbol{n}^{*}. \tag{2.22}$$

By using the relation $2\partial_{\mathbf{g}}J = J\mathbf{g}^{-1}$, one can derive

$$\Delta\boldsymbol{n}^{*} = \boldsymbol{n}^{*}\otimes\mathbf{g}^{-1} : \mathbf{g}\nabla\Delta\boldsymbol{\varphi} - (\nabla\Delta\boldsymbol{\varphi})^{\top}\boldsymbol{n}^{*}. \tag{2.23}$$

Consequently, all the non-linear terms in Equation $(2.7)_1$ and Equation $(2.7)_2$ are linearized, so that incremental forms in Equation $(2.9)_1$ and Equation $(2.9)_2$ can be respectively written as

$$\begin{aligned}
\Delta G^{\boldsymbol{\varphi}} = &\int_{\mathcal{B}} \nabla\delta\boldsymbol{\varphi} : \nabla\Delta\boldsymbol{\varphi}\,\hat{\boldsymbol{\tau}}\, dV + \int_{\mathcal{B}} \nabla\delta\boldsymbol{\varphi} : \mathbb{C}^{\boldsymbol{\varphi}\boldsymbol{\varphi}} : \mathbf{g}\nabla\Delta\boldsymbol{\varphi}\, dV \\
&+ \sum_{\mathrm{i=lv,rv}} \int_{\mathcal{S}_{\mathrm{i}}} \delta\boldsymbol{\varphi}\cdot\boldsymbol{n}\, da\, \frac{\hat{p}_{\mathrm{i}}^{'}}{3}\int_{\mathcal{S}_{\mathrm{i}}} \Big[\boldsymbol{n}\cdot\Delta\boldsymbol{\varphi} + (\boldsymbol{\varphi}\cdot\boldsymbol{n})\,\mathbf{g}^{-1} : \mathbf{g}\,\nabla\Delta\boldsymbol{\varphi} - \boldsymbol{n}\otimes\boldsymbol{\varphi} : \nabla\Delta\boldsymbol{\varphi}\Big] da \\
&+ \sum_{\mathrm{i=lv,rv}} \int_{\mathcal{S}_{\mathrm{i}}} \delta\boldsymbol{\varphi}\cdot\hat{p}_{\mathrm{i}}(\boldsymbol{n}\otimes\mathbf{g}^{-1} : \mathbf{g}\,\nabla\Delta\boldsymbol{\varphi} - \boldsymbol{n}\nabla\Delta\boldsymbol{\varphi})\, da
\end{aligned} \tag{2.24}$$

and

$$\Delta G^{\phi} = \int_{\mathcal{B}} \delta\Phi\,\dot{\Phi}\, dV + \int_{\mathcal{B}} \nabla\delta\Phi\cdot\boldsymbol{D}\cdot\nabla\Delta\Phi\, dV - \int_{\mathcal{B}} \delta\Phi\, H\,\Delta\Phi\, dV\,. \tag{2.25}$$

2.5 Time and space discretization

The discretizations of the residual terms in time and space are operated in the framework of the finite difference and finite element method by using the incremental forms in Equation (2.24) and Equation (2.25). Firstly, we consider the incremental time domain $[t, t_{n+1}]$, which is interpreted as the difference between the current and previous solution time $\Delta t \coloneqq t_{n+1} - t_n$. The subscript $n+1$ is cleared away for compactness so that the transmembrane potential terms in time t_{n+1} and in time t_n are written as

$$\Phi = \Phi(\boldsymbol{X}, t_{n+1}) \quad \text{and} \quad \Phi_n = \Phi(\boldsymbol{X}, t_n)\,. \tag{2.26}$$

Through the implicit Euler scheme, the approximation of the time derivative of the electrical field is written as

$$\dot{\Phi} \approx \frac{\Phi - \Phi_n}{\Delta t} \tag{2.27}$$

where all of the values at t_n are known and the rate of the transmembrane potential is constant during Δt. Next, when it comes to the space discretization, the solid domain of interest $\mathcal{B}$ is divided into subdomains, so that $\mathcal{B} \approx \cup_{k=1}^{n}\mathcal{B}^{k}$ holds. Furthermore, regarding inner surface boundaries, i.e. the endocardium placed in LV and RV, $\mathcal{S}_{\mathrm{lv}} \approx \cup_{k=1}^{n_{\mathrm{lv}}}\mathcal{S}_{\mathrm{lv}}^{k}$ and $\mathcal{S}_{\mathrm{rv}} \approx \cup_{k=1}^{n_{\mathrm{rv}}}\mathcal{S}_{\mathrm{rv}}^{k}$ are established, where n_{lv} and n_{rv} are the number of the surface element

on LV and RV endocardium, respectively. Subsequently, the unknown fields are interpolated, i.e. the placement $\boldsymbol{\varphi}^k$ and the transmemebrane potential field Φ^k, as well as the corresponding weight functions over each element domain by introducing the isoparametric concept on element level in terms of generalized nodal placement $\boldsymbol{\varphi}^i$ and transmembrane potential Φ^i. That is,

$$\begin{aligned} \boldsymbol{\varphi}^k &= \sum_{i=1}^{n_{\text{en}}} N^i \boldsymbol{\varphi}^i, \qquad \delta\boldsymbol{\varphi}^k = \sum_{i=1}^{n_{\text{en}}} N^i \delta\boldsymbol{\varphi}^i, \\ \Phi^k &= \sum_{i=1}^{n_{\text{en}}} N^i \Phi^i, \qquad \delta\Phi^k = \sum_{i=1}^{n_{\text{en}}} N^i \delta\Phi^i, \end{aligned} \tag{2.28}$$

where n_{en} stands for the number of element nodes. Furthermore, the spatial gradient of the corresponding weight functions and increments of the field variables are discretized as

$$\begin{aligned} \nabla\delta\boldsymbol{\varphi}^k &= \sum_{i=1}^{n_{\text{en}}} \delta\boldsymbol{\varphi}^i \otimes \nabla N^i, \qquad \nabla\Delta\boldsymbol{\varphi}^k = \sum_{i=1}^{n_{\text{en}}} \Delta\boldsymbol{\varphi}^i \otimes \nabla N^i, \\ \nabla\delta\Phi^k &= \sum_{i=1}^{n_{\text{en}}} \delta\Phi^i \otimes \nabla N^i, \qquad \nabla\Delta\Phi^k = \sum_{i=1}^{n_{\text{en}}} \Delta\Phi^i \otimes \nabla N^i \,. \end{aligned} \tag{2.29}$$

Similarly, ventricular cavity volumes are interpolated as

$$\mathcal{V}_{\text{i}} \coloneqq \frac{1}{3}\mathbf{A}_{k=1}^{n_{\text{i}}} \int_{\mathcal{S}_{\text{i}}^k} N^i \boldsymbol{\varphi}^i \cdot \boldsymbol{n}\, da, \tag{2.30}$$

which is conceptualized as the integration of all trigonal pyramid volumes created by linking the edges of discrete surface elements with a vertex located at the basal surface.
Finally, the global residual vector $\mathbf{R}$ can be represented in terms of the interpolated field variables,

$$\mathbf{R} = \mathbf{A}_{k=1}^{n}\mathbf{R}_{\text{el}} + \mathbf{A}_{k=1}^{n_{\text{i}}}\boldsymbol{\mathcal{R}}_{\text{el}} = 0 \quad \text{where} \quad \mathbf{R}_{\text{el}} \coloneqq \left\{ \begin{array}{c} \mathbf{R}^{\boldsymbol{\varphi}} \\ \mathbf{R}^{\phi} \end{array} \right\}; \quad \boldsymbol{\mathcal{R}}_{\text{el}} \coloneqq \left\{ \begin{array}{c} \boldsymbol{\mathcal{R}}_{\text{i}}^{\boldsymbol{\varphi}} \\ \mathbf{0} \end{array} \right\}, \tag{2.31}$$

where

$$\begin{aligned} \mathbf{R}^{\boldsymbol{\varphi}} &\coloneqq \int_{\mathcal{B}^k} \nabla N^i \cdot \hat{\boldsymbol{\tau}}\, dV - \int_{\mathcal{B}^k} N^i\, \boldsymbol{b}\, dV - \int_{\mathcal{S}_{\text{t}}^k} N^i\, \bar{\boldsymbol{t}}\, da, \\ \mathbf{R}^{\phi} &\coloneqq \int_{\mathcal{B}^k} \left(N^i\, \frac{\Phi - \Phi_n}{\Delta t} + \nabla N^i \cdot \hat{\boldsymbol{q}} \right) dV - \int_{\mathcal{B}^k} N^i\, \hat{F}^{\phi} dV - \int_{\mathcal{S}_q^k} N^i\, \bar{q}\, da, \\ \boldsymbol{\mathcal{R}}_{\text{i}}^{\varphi} &\coloneqq \int_{\mathcal{S}_{\text{i}}^k} N^i\, \hat{p}_{\text{i}} \boldsymbol{n}\, da, \end{aligned} \tag{2.32}$$

for $\text{i} = \{\text{lv}, \text{rv}\}$. Furthermore, each component of the global residual vector is assembled by using $\mathbf{A}$, which are calculated at the local element node level. Equivalently, the discretized representation of the global tangent matrix $\mathbf{K}$ can be constructed from Equation (2.9)

$$\mathbf{K} = \mathbf{A}_{k=1}^{n}\mathbf{K}_{\text{el}} + \mathbf{A}_{k=1}^{n_{\text{i}}}\boldsymbol{\mathcal{K}}_{\text{el}} + \mathbf{A}_{k=1}^{n_{\text{i}}}\tilde{\boldsymbol{\mathcal{K}}}_{\text{el}}. \tag{2.33}$$

The global tangent matrices are composed by

$$\mathbf{K}_{\text{el}} \coloneqq \left[\begin{array}{cc} \mathbf{K}^{\boldsymbol{\varphi}\boldsymbol{\varphi}} & \mathbf{0} \\ \mathbf{0} & \mathbf{K}^{\phi\phi} \end{array} \right], \quad \boldsymbol{\mathcal{K}}_{\text{el}} \coloneqq \left[\begin{array}{cc} \boldsymbol{\mathcal{K}}_{\text{i}}^{\boldsymbol{\varphi}\boldsymbol{\varphi}} & \mathbf{0} \\ \mathbf{0} & \mathbf{0} \end{array} \right], \quad \tilde{\boldsymbol{\mathcal{K}}}_{\text{el}} \coloneqq \left[\begin{array}{cc} \tilde{\boldsymbol{\mathcal{K}}}_{\text{i}}^{\boldsymbol{\varphi}\boldsymbol{\varphi}} & \mathbf{0} \\ \mathbf{0} & \mathbf{0} \end{array} \right] \tag{2.34}$$

with

$$
\begin{aligned}
\mathbf{K}^{\boldsymbol{\varphi\varphi}} &\coloneqq \int_{\mathcal{B}^k} (\nabla N^i \cdot \mathbb{C}^{\boldsymbol{\varphi\varphi}} \cdot \nabla N^j + \nabla N^i \cdot \hat{\boldsymbol{\tau}} \cdot \nabla N^j) dV, \\
\mathbf{K}^{\phi\phi} &\coloneqq \int_{\mathcal{B}^k} \left[N^i \left(\frac{1}{\Delta t} - H \right) N^j + \nabla N^i \cdot \boldsymbol{D} \cdot \nabla N^j \right] dV, \\
\boldsymbol{\mathcal{K}}_{\mathrm{i}}^{\boldsymbol{\varphi\varphi}} &\coloneqq \int_{\mathcal{S}_{\mathrm{i}}^k} N^i \hat{p}_{\mathrm{i}} (\boldsymbol{n} \otimes \mathbf{g}^{-1} \cdot \nabla N^j - \boldsymbol{n} \nabla N^j) da, \\
\tilde{\boldsymbol{\mathcal{K}}}_{\mathrm{i}}^{\boldsymbol{\varphi\varphi}} &\coloneqq \int_{\mathcal{S}_{\mathrm{i}}^k} N^i \boldsymbol{n} da \otimes \mathbf{A}_{k=1}^{n_{\mathrm{i}}} \frac{\hat{p}_{\mathrm{i}}^{'}}{3} \int_{\mathcal{S}_{\mathrm{i}}^k} \left[\mathbf{N}^j + (\boldsymbol{\varphi} \cdot \boldsymbol{n}) \mathbf{g}^{-1} \cdot \nabla N^j - \boldsymbol{n} \otimes \boldsymbol{\varphi} \cdot \nabla N^j \right] da \, .
\end{aligned}
\tag{2.35}
$$

Remark. A non-local effect is caused because the pressure load is dependent on the ventricular cavitiy volume during the cardiac cycles. The non-local effect emerges from the corresponding surface elements, which is induced by all element on that surface. Therefore, the dyadic product of $\boldsymbol{n}$ of the discrete element and globally assembled sensitivities of $\hat{p}_{\mathrm{i}}$ with respect to the deformation field is required on the associated surface domain, which is included in $\tilde{\boldsymbol{\mathcal{K}}}_{\mathrm{i}}^{\boldsymbol{\varphi\varphi}}$ as represented in Equation $(2.35)_4$ and contributes the non-local effect. In order to reduce the compatational workload, only non-zero tangent terms are stored in general finite element analysis programs [24]. However, in contrast with other contributions in Equation (2.33), the mechanical part of $\mathbf{A}_{k=1}^{n_{\mathrm{i}}} \tilde{\boldsymbol{\mathcal{K}}}_{\mathrm{el}}$, is entirely occupied due to the interaction between the non-adjacent surface elements. Hence the computational effort is inevitably increased due to the escalation of the number of the non-zero terms in global tangent matrix.

3 Constitutive equations

Due to the characteristics of cardiac tissue, orthotropic hyperelastic model is employed to establish the constitutive relations denoting the electro-visco-elastic behaviour of the myocardium. The constitutive equations are incorporated into the coupled finite element formulation represented in Chapter 2 in order to complete the framework which is utilized to implement numerical examples in Chapter 4. To do this, it is necessary to clearly define the specific forms of the constitutive equations associated with the Kirchhoff stress tensor $\hat{\boldsymbol{\tau}}$, the ventricular pressure $\hat{\boldsymbol{p}}_{\mathrm{i}}$, the current source $\hat{F}^{\phi}$ and the transmembrane potential flux $\hat{\boldsymbol{q}}$. The constitutive equations, except the equation for $\hat{\boldsymbol{p}}_{\mathrm{i}}$, include supplementary terms which are responsible for the reciprocal influence between the two primary fields, the deformation field and electric field. For the equations including ordinary differential equations, it is required to establish algorithmic procedures at gauss quadrature point level to update the temporal variation of the internal variables. An implicit Euler backward integration method is exploited to solve the temporal evolution equations. Furthermore, the Eulerian fourth order tangent moduli for each part, the passive and the visco-active part, are derived.

3.1 Kinematics and rheology

In the section, the rheology for the coupled electro-visco-elastic response of the myocardium is presented. The total deformation gradient $\boldsymbol{F}$ is decomposed into purely elastic, viscous and active parts in multiplicative way. By prescribing the viscous and active deformation gradients along fiber, sheet and normal direction, one dimensional evolution equations in each orthognal orientations are adopted and updated easily in a time-discrete setting. The isotropic response of hyperelastic material is described by the three invariants,

$$I_1 \coloneqq \mathrm{tr}\boldsymbol{C}, \quad I_2 \coloneqq \frac{1}{2}\Big[I_1^2 - \mathrm{tr}(\boldsymbol{C})^2\Big], \quad \text{and} \quad I_3 \coloneqq \det\boldsymbol{C}\,. \tag{3.1}$$

Furthermore, in order to represent the deformation state of the orthotropic microstructure of the myocardium, the additional invariants are required as

$$I_{4\mathrm{f}} = \boldsymbol{f}_0 \cdot \boldsymbol{C}\boldsymbol{f}_0, \quad I_{4\mathrm{s}} = \boldsymbol{s}_0 \cdot \boldsymbol{C}\boldsymbol{s}_0, \quad I_{4\mathrm{n}} = \boldsymbol{n}_0 \cdot \boldsymbol{C}\boldsymbol{n}_0 \quad \text{and} \quad I_{8\mathrm{fs}} = \boldsymbol{f}_0 \cdot \boldsymbol{C}\boldsymbol{s}_0 \tag{3.2}$$

in terms of three reference unit vectors $\boldsymbol{f}_0$, $\boldsymbol{s}_0$ and $\boldsymbol{n}_0$. The non-equilibrium responses of the material along the fiber, sheet and normal direction respectively are described by the three logarithmic strains

$$\epsilon_{\boldsymbol{f}} \coloneqq \frac{1}{2}\ln(I_{4\mathrm{f}}), \quad \epsilon_{\boldsymbol{s}} \coloneqq \frac{1}{2}\ln(I_{4\mathrm{s}}), \quad \epsilon_{\boldsymbol{n}} \coloneqq \frac{1}{2}\ln(I_{4\mathrm{n}})\,. \tag{3.3}$$

The deformation of myocardium is acquired by assuming the fictitious configuration between the reference and current configuration [25]. Consequently, the total deformation gradient is multiplicatively decomposed as

$$\boldsymbol{F} = \boldsymbol{F}^m\,\boldsymbol{F}^a \quad \text{and} \quad \boldsymbol{F}^m = \boldsymbol{F}^e\,\boldsymbol{F}^v \tag{3.4}$$

where $\boldsymbol{F}^m$, $\boldsymbol{F}^a$, $\boldsymbol{F}^e$ and $\boldsymbol{F}^v$ are the mechanical, active, elastic and viscoealstic part of deformation gradient, respectively. $\boldsymbol{F}^a$ is formulated in terms of the prescribed deformation arising due to the myocardial contraction that is solely govenrned by the transmembrane potential Φ. The mechanical deformation $\boldsymbol{F}^m$ is further decomposed into elastic part $\boldsymbol{F}^e$ and viscous part $\boldsymbol{F}^v$. Based on the microstructure of the myocardium, the following mechanical deformation gradient and right Cauchy-Green tensor are defined as

$$\boldsymbol{F}^m \coloneqq \boldsymbol{F}\boldsymbol{F}^{a^{-1}} \quad \text{and} \quad \boldsymbol{C}^m \coloneqq \boldsymbol{F}^{m^T}\boldsymbol{g}\boldsymbol{F}^m \,. \tag{3.5}$$

The active part of the deformation gradient $\boldsymbol{F}^a$ is concerned with the fiber direction and defined as

$$\boldsymbol{F}^a \coloneqq \boldsymbol{1} + (\lambda_f^a - 1)\boldsymbol{f}_0 \otimes \boldsymbol{f}_0 \tag{3.6}$$

where λ_f^a is the stretch generated along the fiber direction responsible for the contraction. By use of Equation $(3.5)_1$, the mechanical part of the deformation gradient is achieved as

$$\boldsymbol{F}^m = \boldsymbol{F} + \left(\frac{1}{\lambda_f^a} - 1\right)\boldsymbol{F}\boldsymbol{f}_0 \otimes \boldsymbol{f}_0 \,. \tag{3.7}$$

Additionally, the viscous part of deformation gradient $\boldsymbol{F}^v$ is defined as

$$\boldsymbol{F}^v \coloneqq \boldsymbol{1} + (\lambda_{\mathrm{f}}^v - 1)\boldsymbol{f}_0 \otimes \boldsymbol{f}_0 + (\lambda_{\mathrm{s}}^v - 1)\boldsymbol{s}_0 \otimes \boldsymbol{s}_0 + (\lambda_{\mathrm{n}}^v - 1)\boldsymbol{n}_0 \otimes \boldsymbol{n}_0 \,. \tag{3.8}$$

in terms of viscous stretchs λ_f^v, λ_s^v and λ_n^v, respectively. Consequently, using Equation (3.8), the elastic part of the deformation gradient is obtained as

$$\boldsymbol{F}^e = \boldsymbol{F}^m + \left(\frac{1}{\lambda_f^v} - 1\right)\boldsymbol{F}^m\boldsymbol{f}_0 \otimes \boldsymbol{f}_0 + \left(\frac{1}{\lambda_s^v} - 1\right)\boldsymbol{F}^m\boldsymbol{s}_0 \otimes \boldsymbol{s}_0 + \left(\frac{1}{\lambda_n^v} - 1\right)\boldsymbol{F}^m\boldsymbol{n}_0 \otimes \boldsymbol{n}_0 \,. \tag{3.9}$$

Note that the orthogonality of Equation (3.6) and Equation (3.8) makes $\boldsymbol{F}^e$ insensitive to the order of $\boldsymbol{F}^v$ and $\boldsymbol{F}^a$ in Equation (3.4) which are rotation free tensors. By the push-forward of the mutually orthogonal Lagrangian orientation vectors $\boldsymbol{f}_0$, $\boldsymbol{s}_0$ and $\boldsymbol{n}_0$, the corresponding Eulerian vectors and corresponding stretches are achieved as follows

$$\begin{array}{llllllll} \boldsymbol{f} & = \boldsymbol{F}\boldsymbol{f}_0 & \rightarrow & \lambda_{\mathrm{f}} \coloneqq & |\boldsymbol{f}| & = \sqrt{\boldsymbol{f}\cdot\boldsymbol{f}} & = \sqrt{I_{4\mathrm{f}}}\,, \\ \boldsymbol{s} & = \boldsymbol{F}\boldsymbol{s}_0 & \rightarrow & \lambda_{\mathrm{s}} \coloneqq & |\boldsymbol{s}| & = \sqrt{\boldsymbol{s}\cdot\boldsymbol{s}} & = \sqrt{I_{4\mathrm{s}}}\,, \\ \boldsymbol{n} & = \boldsymbol{F}\boldsymbol{n}_0 & \rightarrow & \lambda_{\mathrm{n}} \coloneqq & |\boldsymbol{n}| & = \sqrt{\boldsymbol{n}\cdot\boldsymbol{n}} & = \sqrt{I_{4\mathrm{n}}}\,. \end{array} \tag{3.10}$$

Due to the feature of the diagonalized tensors $\boldsymbol{F}^a$ and $\boldsymbol{F}^v$, it is allowed to multiplicatively decompose the stretches along the mutually orthogonal directions as follows

$$\lambda_{\mathrm{f}} = \lambda_{\mathrm{f}}^e\lambda_{\mathrm{f}}^v\lambda_{\mathrm{f}}^a, \quad \lambda_{\mathrm{s}} = \lambda_{\mathrm{s}}^e\lambda_{\mathrm{s}}^v \quad \text{and} \quad \lambda_{\mathrm{n}} = \lambda_{\mathrm{n}}^e\lambda_{\mathrm{n}}^v \,. \tag{3.11}$$

Note that the stretch along the fiber direction (λ_{f}) is decomposed into active, viscous and elastic part while the stretches along the cross fiber (λ_{s}) and normal direction (λ_{n}) are decomposed into the viscous and the elastic part. The multiplicative decomposition and the rheology representing the electro-visco-elastic behaviour of myocardium are shown in Figure 3.1. Alternatively, the multiplicative decomposition of strethces along the orthogonal directions can be rewritten in additive format using logarithmic strain in Equation (3.3) as follows

$$\epsilon_{\mathrm{f}} = \epsilon_{\mathrm{f}}^e + \epsilon_{\mathrm{f}}^v + \epsilon_{\mathrm{f}}^a, \quad \epsilon_{\mathrm{s}} = \epsilon_{\mathrm{s}}^e + \epsilon_{\mathrm{s}}^v \quad \text{and} \quad \epsilon_{\mathrm{n}} = \epsilon_{\mathrm{n}}^e + \epsilon_{\mathrm{n}}^v \tag{3.12}$$

with

$$\epsilon_{\mathrm{f}} = \ln\lambda_{\mathrm{f}}, \quad \epsilon_{\mathrm{s}} = \ln\lambda_{\mathrm{s}} \quad \text{and} \quad \epsilon_{\mathrm{n}} = \ln\lambda_{\mathrm{n}} \,. \tag{3.13}$$

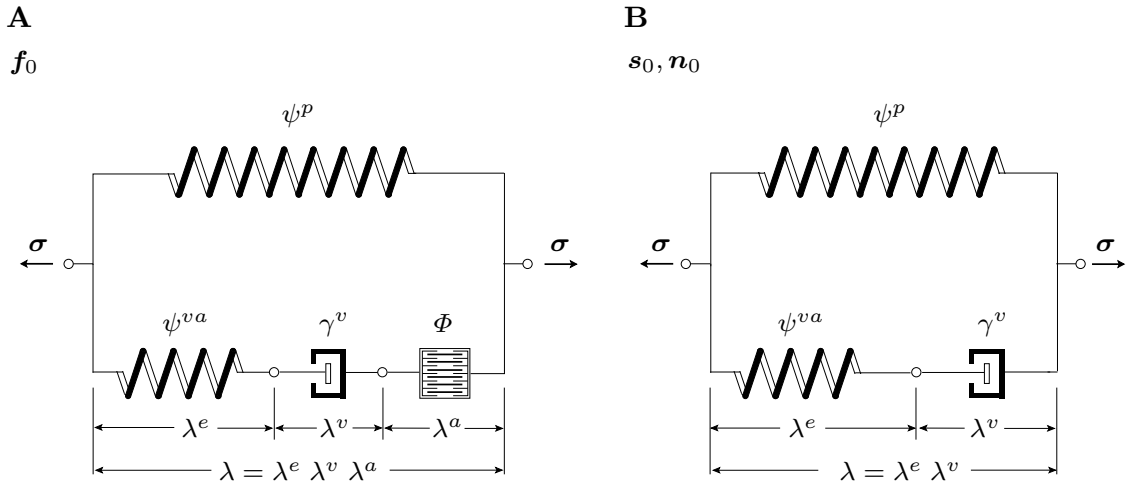

Figure 3.1: Rheology for electro-visco-elastic response for the fiber direction (**A**) and for the sheet and normal directions (**B**).

3.2 Stress responses

The modified Hill model [1] describes the distinctive orthotropic stress responses of cardiac cells where the myocardium responses distinctly along three mutually orthogonal direction, fiber $\boldsymbol{f}_0$, sheet $\boldsymbol{s}_0$ and normal $\boldsymbol{n}_0$ as depicted in Figure 3.1. By adopting the rheology from the Hill model, the total deformation gradient is multiplicatively decomposed into elastic, viscous and active parts. Additionally, the free energy function is decomposed into passive and visco-active contributions

$$\psi(\mathbf{g}, \mathfrak{s}; \boldsymbol{F}, \boldsymbol{F}^e) = \hat{\psi}^p(\mathbf{g}, \mathfrak{s}; \boldsymbol{F}) + \hat{\psi}^{va}(\mathbf{g}, \mathfrak{s}; \boldsymbol{F}^e). \tag{3.14}$$

Due to the fact that the formulation is performed in the Eulerian setting, the covariant Eulerian metric $\mathbf{g}$ is unequivocally included as one of the arguments of the constitutive functions. The passive part $\hat{\psi}^p$ is a function of the total deformation gradient $\boldsymbol{F}$ and the visco-active part $\hat{\psi}^p$ is a function of the elastic part of the deformation gradient $\boldsymbol{F}^e = \boldsymbol{F}(\boldsymbol{F}^v\boldsymbol{F}^a)^{-1}$. Furthermore, the set of structural tensors $\mathfrak{s}$, which are responsible for the description of orthotropic micro-structure of the myocardium, is

$$\mathfrak{s} = \{\boldsymbol{f}_0 \otimes \boldsymbol{f}_0, \boldsymbol{s}_0 \otimes \boldsymbol{s}_0, \boldsymbol{n}_0 \otimes \boldsymbol{n}_0, \boldsymbol{f}_0 \otimes \boldsymbol{s}_0\}. \tag{3.15}$$

By utilizing the method of Coleman and Noll and exploiting the Doyle-Ericksen formula [26], the Kirchhoff stresses are derived from Equation (3.14) as follows

$$\hat{\boldsymbol{\tau}} = \hat{\boldsymbol{\tau}}^p + \hat{\boldsymbol{\tau}}^{va} \quad \rightarrow \quad \hat{\boldsymbol{\tau}}^p \coloneqq 2\partial_{\mathbf{g}}\hat{\psi}^p(\mathbf{g}, \mathfrak{s}; \boldsymbol{F}) \quad \text{and} \quad \hat{\boldsymbol{\tau}} \coloneqq 2\partial_{\mathbf{g}}\hat{\psi}^{va}(\mathbf{g}, \mathfrak{s}; \boldsymbol{F}, \boldsymbol{F}^e) \tag{3.16}$$

with the passive stress $\hat{\boldsymbol{\tau}}^p$ and visco-active stress $\hat{\boldsymbol{\tau}}^{va}$. Similarly, the fourth order spatial moduli can be derived as follows

$$\mathbb{C}^{\boldsymbol{\varphi}\boldsymbol{\varphi}} = \mathbb{C}^p + \mathbb{C}^{va}_{\text{algo}} \quad \rightarrow \quad \mathbb{C}^p \coloneqq 2\partial_{\mathbf{g}}\hat{\boldsymbol{\tau}}^p(\mathbf{g}, \mathfrak{s}; \boldsymbol{F}) \quad \text{and} \quad \mathbb{C}^{va}_{\text{algo}} \coloneqq 2\partial_{\mathbf{g}}\hat{\boldsymbol{\tau}}^{va}(\mathbf{g}, \mathfrak{s}; \boldsymbol{F}, \boldsymbol{F}^e) \tag{3.17}$$

where $\mathbb{C}^p$ and $\mathbb{C}^{va}_{\text{algo}}$ are the passive part and the visco-active part, respectively.

3.2.1 Passive stress

The passive response is decomposed into a pure volumetric part which acts as a penalty term and orthotropic hyperelastic part

$$\hat{\psi}^p(\mathbf{g}, \mathfrak{s}; \boldsymbol{F}) = U(J) + \bar{\psi}^p(I_1, I_{4\mathrm{f}}, I_{4\mathrm{s}}, I_{8\mathrm{fs}}). \tag{3.18}$$

Therein, $U(J)$, depending explicitly on the volume map $J \coloneqq \det(\boldsymbol{F})$, is the volumetric part used to represent quasi-incompressibile behavior as follow

$$U(J) = \frac{\kappa}{2}\left(\frac{J^2-1}{2} - \ln J\right) - a \ln J. \tag{3.19}$$

To model the orthotropic hyperelastic part of the passive response of the myocardium $\bar{\psi}^p(I_1, I_{4\mathrm{f}}, I_{4\mathrm{s}}, I_{8\mathrm{fs}})$, Fung-type free energy functions of Holzapfel and Ogden [27] is adopted as

$$\begin{aligned}\bar{\psi}^p(I_1, I_{4\mathrm{f}}, I_{4\mathrm{s}}, I_{8\mathrm{fs}}) \quad &= \frac{a}{2b}[\exp[b(I_1-3)]-1] + \sum_{\mathrm{i=f,s}} \frac{a_\mathrm{i}}{2b_\mathrm{i}}\left[\exp\left(b_\mathrm{i}\left\langle I_{4\mathrm{i}}-1\right\rangle^2\right)-1\right] \\ &+ \frac{a_{8\mathrm{fs}}}{2b_{8\mathrm{fs}}}\left[\exp\left(b_{8\mathrm{fs}} I_{8\mathrm{fs}}^2\right)-1\right]\end{aligned} \tag{3.20}$$

where a, b, $a_\mathrm{f}, b_\mathrm{f}, a_\mathrm{s}, b_\mathrm{s}, a_\mathrm{n}, b_\mathrm{n}, a_{8\mathrm{fs}}$ and $b_{8\mathrm{fs}}$ are the non-negative material parameters responsible for describing the deformation state of the isotropic and orthotropic microstructure of the myocardium. Also, Macaulay brackets $\langle x\rangle = (x+|x|)/2$ which exclude the negative values of $I_{4\mathrm{i}} - 1$ are adopted. Beacuse the collagen fibers in the cardiac muscle cells are buckled, they do not support any compressive load [27]. In similar manner with Equation (3.18) The passive Kirchhoff tensor in Equation (3.16) is additively decomposed into its volumetric part and the orthotropic part as

$$\hat{\boldsymbol{\tau}}^p = \boldsymbol{\tau}^{vol} + \bar{\boldsymbol{\tau}}^p \tag{3.21}$$

where

$$\begin{aligned}\boldsymbol{\tau}^{vol} \quad &\coloneqq 2\partial_{\mathbf{g}} U(J) = \hat{p}\,\mathbf{g}^{-1} \quad \text{and} \\ \bar{\boldsymbol{\tau}}^p \quad &\coloneqq 2\partial_{\mathbf{g}}\bar{\psi}^p = \Psi_1 \boldsymbol{b} + \Psi_{4\mathrm{f}}\boldsymbol{f}\otimes\boldsymbol{f} + \Psi_{4\mathrm{s}}\boldsymbol{s}\otimes\boldsymbol{s} + \Psi_{8\mathrm{fs}}\mathrm{sym}(\boldsymbol{f}\otimes\boldsymbol{s})\end{aligned} \tag{3.22}$$

by means of the deformation dependent scalar coefficients

$$\begin{aligned}\Psi_1 \quad &\coloneqq 2\partial_{I_1}\bar{\psi}^p \quad &&= a\exp[b(I_1-3)], \\ \Psi_{4\mathrm{f}} \quad &\coloneqq 2\partial_{I_{4\mathrm{f}}}\bar{\psi}^p \quad &&= a_\mathrm{f}\left\langle I_{4\mathrm{f}}-1\right\rangle \exp[b_\mathrm{f}\left\langle I_{4\mathrm{f}}-1\right\rangle^2], \\ \Psi_{4\mathrm{s}} \quad &\coloneqq 2\partial_{I_{4\mathrm{s}}}\bar{\psi}^p \quad &&= a_\mathrm{s}\left\langle I_{4\mathrm{s}}-1\right\rangle \exp[b_\mathrm{s}\left\langle I_{4\mathrm{s}}-1\right\rangle^2], \\ \Psi_{8\mathrm{fs}} \quad &\coloneqq 2\partial_{I_{8\mathrm{fs}}}\bar{\psi}^p \quad &&= 2a_{8\mathrm{fs}} I_{8\mathrm{fs}} \exp[b_{8\mathrm{fs}} I_{8\mathrm{fs}}^2], \\ \hat{p} \quad &\coloneqq J\partial_J U \quad &&= \frac{\kappa}{2}(J^2-1) - a.\end{aligned} \tag{3.23}$$

As stated in Equation (3.17), the passive part of tangent moduli are calculated as

$$\mathbb{C}^p = \mathbb{C}^{vol} + \bar{\mathbb{C}}^p \tag{3.24}$$

where $\mathbb{C}^{vol} = (\hat{p}+\hat{\kappa})\mathbf{g}^{-1}\otimes\mathbf{g}^{-1} - 2\hat{p}\mathbb{I}_{\mathbf{g}^{-1}}$ is attained by taking derivative of the volumetric part of the passive stress. Therein, $\hat{\kappa} \coloneqq J^2\partial_{JJ}^2 U(J)$ is volumetric modulus and the fourth-order symmetric identity tensor is

$$\mathbb{I}_{\mathbf{g}^{-1}} \coloneqq -\partial_{\mathbf{g}}\mathbf{g}^{-1} \quad \text{with} \quad \mathbb{I}_{\mathbf{g}^{-1}}^{abcd} = \frac{1}{2}\left[\delta^{ac}\delta^{bd} + \delta^{ad}\delta^{bc}\right]. \tag{3.25}$$

The tangent term for the passive myocardium behaviour is defined as

$$\bar{\mathbb{C}}^p = \Psi_1' \boldsymbol{b} \otimes \boldsymbol{b} + \Psi_{4\mathrm{f}}' \mathbb{F} + \Psi_{4\mathrm{s}} \mathbb{S} + \Psi_{8\mathrm{fs}}' \mathrm{sym}(\boldsymbol{f} \otimes \boldsymbol{s}) \otimes \mathrm{sym}(\boldsymbol{s} \otimes \boldsymbol{f}) \tag{3.26}$$

in terms of the second derivative of the free energy with respect to the invariants

$$\begin{array}{lll} \Psi_1' & \coloneqq 4\partial_{I_1} \bar{\psi}^p & = 2ab \exp[b(I_1 - 3)], \\ \Psi_{4\mathrm{f}}' & \coloneqq 4\partial_{I_{4\mathrm{f}}} \bar{\psi}^p & = 4a_\mathrm{f} \exp[b_\mathrm{f} \langle I_{4\mathrm{f}} - 1 \rangle^2](2b_\mathrm{f} \langle I_{4\mathrm{f}} - 1 \rangle^2 + 1), \\ \Psi_{4\mathrm{s}}' & \coloneqq 4\partial_{I_{4\mathrm{s}}} \bar{\psi}^p & = 4a_\mathrm{s} \exp[b_\mathrm{s} \langle I_{4\mathrm{s}} - 1 \rangle^2](2b_\mathrm{s} \langle I_{4\mathrm{s}} - 1 \rangle^2 + 1), \\ \Psi_{8\mathrm{fs}}' & \coloneqq 4\partial_{I_{8\mathrm{fs}}} \bar{\psi}^p & = 4a_\mathrm{fs} \exp[b_\mathrm{fs} I_{8\mathrm{fs}}^2](2b_\mathrm{fs} I_{8\mathrm{fs}}^2 + 1) \end{array} \tag{3.27}$$

and the fourth order structural tensors

$$\mathbb{F} \coloneqq \boldsymbol{f} \otimes \boldsymbol{f} \otimes \boldsymbol{f} \otimes \boldsymbol{f} \quad \text{and} \quad \mathbb{S} \coloneqq \boldsymbol{s} \otimes \boldsymbol{s} \otimes \boldsymbol{s} \otimes \boldsymbol{s}. \tag{3.28}$$

3.2.2 Visco-active stress

In the subsection, for the visco-active stress response being found to be present in the myocardium due to electrical excitation, a simple quadratic equation is adopted [28]

$$\hat{\psi}^{va}(\mathbf{g}, \mathfrak{s}; \boldsymbol{F}^e) = \sum_{\mathrm{i=f,s,n}} \bar{\psi}_\mathrm{i}^{va}(\epsilon_\mathrm{i}^e) = \frac{1}{2} \sum_{\mathrm{i=f,s,n}} \mu_\mathrm{i} \epsilon_\mathrm{i}^e \epsilon_\mathrm{i}^e \tag{3.29}$$

in terms of the shear moduli μ_i and the lastic logarithmic strains in the mutually orthogonal direction of myocardium

$$\begin{aligned} \epsilon_\mathrm{f}^e &= \epsilon_\mathrm{f} - \epsilon_\mathrm{f}^v - \epsilon_\mathrm{f}^a, \\ \epsilon_\mathrm{s}^e &= \epsilon_\mathrm{s} - \epsilon_\mathrm{s}^v, \\ \epsilon_\mathrm{n}^e &= \epsilon_\mathrm{n} - \epsilon_\mathrm{n}^v \,. \end{aligned} \tag{3.30}$$

As mentioned in, Equation (3.16), the visco-active part of the Kirchhoff stress tensor is described as

$$\boldsymbol{\tau}^{va} = \tau_\mathrm{f} \boldsymbol{f} \otimes \boldsymbol{f} + \tau_\mathrm{s} \boldsymbol{s} \otimes \boldsymbol{s} + \tau_\mathrm{n} \boldsymbol{n} \otimes \boldsymbol{n} \tag{3.31}$$

and the coefficients are defined as

$$\tau_\mathrm{i} \coloneqq 2\partial_{I_{4\mathrm{i}}} \bar{\psi}_\mathrm{i}^{va} = \frac{\sigma_\mathrm{i}}{I_{4\mathrm{i}}} \quad \text{with} \quad \sigma_\mathrm{i} = \mu_\mathrm{i} \epsilon_\mathrm{i}^e \,. \tag{3.32}$$

3.2.3 Evolution equation for viscous dashpot

The dissipation potential $\mathcal{D}$ which satisfies the Biot equation [29] is used to calculate the non-equilibrium response of the material as follows

$$\begin{aligned} &\partial_{\epsilon_\mathrm{f}^v} \bar{\psi}_\mathrm{f}^{va}(\epsilon_\mathrm{f}, \epsilon_\mathrm{f}^v, \epsilon_\mathrm{f}^a) + \partial_{\dot{\epsilon}_\mathrm{f}^v} \mathcal{D}(\dot{\epsilon}_\mathrm{f}^v) = 0 \quad \text{with} \quad \epsilon_\mathrm{f}^v(0) = \epsilon_\mathrm{f}^{v0}, \\ &\partial_{\epsilon_\mathrm{i}^v} \bar{\psi}_\mathrm{i}^{va}(\epsilon_\mathrm{i}, \epsilon_\mathrm{i}^v) + \partial_{\dot{\epsilon}_\mathrm{i}^v} \mathcal{D}(\dot{\epsilon}_\mathrm{i}^v) = 0 \quad \text{with} \quad \epsilon_\mathrm{i}^v(0) = \epsilon_\mathrm{i}^{v0}, \quad \text{for} \quad \mathrm{i} \coloneqq \{\mathrm{s}, \mathrm{n}\}. \end{aligned} \tag{3.33}$$

Herein, ϵ_i^v with $\mathrm{i} = \{\mathrm{f}, \mathrm{s}, \mathrm{n}\}$ are the strain-like internal variables. The logarithmic stresses σ_i and the thermodynamical force β_i conjugates to the internal variable are related to the free energy function as

$$\sigma_\mathrm{i} \coloneqq \partial_{\epsilon_\mathrm{i}} \psi_\mathrm{i}^{va}(\epsilon_\mathrm{i}^e) \quad \text{and} \quad \beta_\mathrm{i} \coloneqq -\partial_{\epsilon_\mathrm{i}}^v \psi_\mathrm{i}^{va}(\epsilon_\mathrm{i}^e) \,. \tag{3.34}$$

Therein, the particular form of dissipation potential $\mathcal{D}$ for the standard dissipative solids, proposed in [28], is expressed in terms of m_i, η_i and $\hat{\beta}$ as follows

$$\mathcal{D}(\dot{\epsilon}_\mathrm{i}^v) \coloneqq \sum_{\mathrm{i=f,s,n}} \frac{\hat{\beta}_\mathrm{i}^2}{\eta_\mathrm{i}} \frac{1+m_\mathrm{i}}{2+m_\mathrm{i}} \left(\frac{\eta_\mathrm{i}}{\hat{\beta}_\mathrm{i}} |\dot{\epsilon}_\mathrm{i}^v| \right)^{\frac{2+m_\mathrm{i}}{1+m_\mathrm{i}}} \tag{3.35}$$

Therein, m_i is parameter for transition from purely linear viscoelastic flow to nonlinear viscoplastic flow. η_i is the viscosity parameter. $\hat{\beta}$ is the activation stress and will be taken as unity for ensuring the consistent units. By exploiting Equation (3.29) and Equation (3.35) with some manipulations in Biot-equation, following temporal evolution equation for internal variables are derived as

$$\dot{\epsilon}_\mathrm{i}^v = \frac{1}{\eta_\mathrm{i}} \left| \frac{\beta_\mathrm{i}}{\hat{\beta}_\mathrm{i}} \right|^{m_\mathrm{i}} \beta_\mathrm{i} \tag{3.36}$$

in the fiber, sheet and normal directions. For $m_\mathrm{i} > 0$, the evolution equation in terms of β_i remains nonlinear. Therefore, the update iteration is operated at gauss point level to obtain the internal strain-like variable ϵ_i^v by using a Newton-Raphson method.

3.2.4 Evolution equation for active stretch

The characteristics of the $[Ca^{2+}]$ and myocardial contraction are nonuniform over the ventricles. The cardiomyocyte located on various location over the heart respectively have different the electrical and mechanical activation, duration and the magnitude of the contraction [30, 31]. These non-homegenity are likely to occur in order to circulate blood throughout the body efficiently and to reduce the possibility of malfunction of the ventricles. In this context, the developed evolution equations in [1] are applied. The active stretch is modelled by the following exponential type evolution equation

$$\dot{\lambda_\mathrm{f}^a} = f(\bar{c}) - (\lambda_\mathrm{f}^a - 1)k_2, \quad \text{with} \quad f(\bar{c}) = \xi[\exp(-q\bar{c}) - 1]. \tag{3.37}$$

Therein, k_2, ξ and q are material parameters. $\bar{c}$, the calcium concentration, is formulated by the following evolution equation

$$\dot{\bar{c}} = g(\phi) - \bar{c}k_1 \quad \text{with} \quad g(\phi) = -\zeta[\ln(1-\phi)]^p \tag{3.38}$$

with the material parameters k_1, ζ and p.

3.3 Visco-active stresses update algorithm

In the section, $\Delta t = t_{n+1} - t_n$ is used as the discrete time increment, where t_{n+1} and t_n symbolize for the current and previous time steps, respectively. Also, all variable without subscript n are considered as values calculated at time t. The update of the evolution equations for the viscous dashpot in Equation (3.36) and the active stretch in Equation (3.37) is required for the components of the visco-active Kirchhoff stress tensor Equation (3.31) in the fibre direction within a time-discrete setting. The component of the visco-active Kirchhoff stress tensor in sheet and normal directions requires only the update of the evolution equations for viscous stretches in Equation (3.36) in a time-discrete setting.

3.3.1 Update of active-stretch in the fibre direction by splitting-algorithm operator

The visco-active stresses in Equation (3.31) is obtained by employing a one-pass operator split algorithm as

$$ALGO_{\mathrm{VA}} = ALGO_{\mathrm{V}} \circ ALGO_{\mathrm{A}} \,. \tag{3.39}$$

where the mechanical stretches are computed as $\lambda_{\mathrm{f}}^{m} = \lambda_{\mathrm{f}}^{e}\lambda_{\mathrm{f}}^{v}$ for frozen viscous deformation $\dot{\lambda}_{\mathrm{f}} = 0$ from the evolution equation of active stretch Equation (3.43)

$$\lambda_{\mathrm{f}} = \lambda_{\mathrm{f}}^{m}\lambda_{\mathrm{f}}^{a} \quad \rightarrow \quad \lambda_{\mathrm{f}}^{m} = \lambda_{\mathrm{f}}\lambda_{\mathrm{f}}^{a-1} \tag{3.40}$$

and the current elastic stretches are computed through the evolution for viscous stretches Equation (3.36) for a frozen active stretch $\dot{\lambda}_{\mathrm{f}}^{a} = 0$

$$\lambda_{\mathrm{f}}^{m} = \lambda_{\mathrm{f}}^{e}\lambda_{\mathrm{f}}^{v} \quad \rightarrow \quad \lambda_{\mathrm{f}}^{e} = \lambda_{\mathrm{f}}^{m}\lambda_{\mathrm{f}}^{v-1} \tag{3.41}$$

The summary for the update algorithms for the one-pass operator splitting algorithm is

$$(V) : \begin{cases} \dot{\lambda}_{\mathrm{f}}^{v} = \dfrac{1}{\eta_{\mathrm{f}}}\left|\dfrac{\beta_{\mathrm{f}}}{\hat{\beta}_{\mathrm{f}}}\right|^{m_{\mathrm{f}}}\beta_{\mathrm{f}} \\ \dot{\lambda}_{\mathrm{f}}^{a} = 0 \\ \dot{\bar{c}} = 0 \end{cases} \quad \text{and} \quad (A) : \begin{cases} \dot{\lambda}_{\mathrm{f}}^{v} = 0 \\ \dot{\lambda}_{\mathrm{f}}^{a} = \xi[\exp(-q\bar{c}) - 1] - (\lambda_{\mathrm{f}}^{a} - 1)k_2 \\ \dot{\bar{c}} = -\zeta[\ln(1-\phi)]^{p} - \bar{c}k_1. \end{cases} \tag{3.42}$$

ALGO (A): Through the implicit Euler scheme in an incremental interval λ_{f}^{a} value at current timestep is computed as

$$\dot{\lambda}_{\mathrm{f}}^{a} \approx \frac{\lambda_{\mathrm{f}}^{a} - \lambda_{\mathrm{f}}^{a}|_{t_n}}{\Delta t} = f(\bar{c}) - (\lambda_{\mathrm{f}}^{a} - 1)k_2 \quad \rightarrow \quad \lambda_{\mathrm{f}}^{a}(\bar{c}) = \frac{f\Delta t + k_2\Delta t + \lambda_{\mathrm{f}}^{a}|_{t_{\mathrm{n}}}}{1 + k_2\Delta t}. \tag{3.43}$$

where $\bar{c}$ is the current value of the intra-cellular calcium concentration. $\bar{c}$ is updated by using the implicit Euler scheme to Equation (3.38)

$$\dot{\bar{c}} \approx \frac{\bar{c} - \bar{c}_n}{\Delta t} = g - \bar{c}\,k_1 \quad \rightarrow \quad \bar{c}(\phi) = \frac{g\Delta t + \bar{c}_n}{1 + k_1\Delta t}. \tag{3.44}$$

With the updated value of λ_{f}^{a}, one can compute the active part of the deformation gradient $\boldsymbol{F}^{a}$.

ALGO (V): In the following, a Newton-Raphson algorithm is utilized for the update of the viscous stretch

$$\dot{\epsilon}_{\mathrm{f}}^{v} \approx \frac{\epsilon_{\mathrm{f}}^{v} - \epsilon_{\mathrm{f}}^{v}|_{t_n}}{\Delta t} = \frac{1}{\eta_{\mathrm{f}}}\left|\frac{\beta_{\mathrm{f}}}{\hat{\beta}_{\mathrm{f}}}\right|^{m_{\mathrm{f}}}\beta_{\mathrm{f}} \quad \text{with} \quad \beta_{\mathrm{f}} \coloneqq -\partial_{\epsilon_{\mathrm{f}}^{v}}\bar{\Psi}^{va} = \mu_{\mathrm{f}}(\epsilon_{\mathrm{f}} - \epsilon_{\mathrm{f}}^{v} - \epsilon_{\mathrm{f}}^{a}). \tag{3.45}$$

The evolution equation with $m_{\mathrm{f}} > 0$, is nonlinear function of $\epsilon_{\mathrm{f}}^{v}$ with no closed form solution. Thus, in order to calculate $\epsilon_{\mathrm{f}}^{v}$, it is required to use a Newton-Raphson iteration method. To this end, a residual expression $\mathcal{R}_{\mathrm{f}}$ is defined in terms of the internal variable $\epsilon_{\mathrm{f}}^{v}$

$$\mathcal{R}(\epsilon_{\mathrm{f}}^{v}) \coloneqq \epsilon_{\mathrm{f}}^{v} - \epsilon_{\mathrm{f}}^{v}|_{t_n} - \Delta t\frac{1}{\eta_{\mathrm{f}}}\left|\frac{\beta_{\mathrm{f}}}{\hat{\beta}_{\mathrm{f}}}\right|\beta_{\mathrm{f}} \tag{3.46}$$

for its iterative solution the linearization is required as

$$L[\mathcal{R}_{\mathrm{f}}] = \mathcal{R}_{\mathrm{f}} + \mathcal{K}\Delta\epsilon_{\mathrm{f}}^{v} \quad \text{with} \quad \mathcal{K}_{\mathrm{f}} \coloneqq \frac{\partial\mathcal{R}_{\mathrm{f}}}{\partial\epsilon_{\mathrm{f}}^{v}}. \tag{3.47}$$

1. Set initial values	Internal variable: $\epsilon_{\mathrm{f}}^{v}(0) = \epsilon_{\mathrm{f}}^{v}\vert_{t_{\mathrm{n}}}$, counter $i = 1$
Do	
2. Compute residual	$\mathcal{R}_{\mathrm{f}}(i) \coloneqq \epsilon_{\mathrm{f}}^{v}(i) - \epsilon_{\mathrm{f}}^{v}\vert_{t_{\mathrm{n}}} - \Delta t \dfrac{1}{\eta_{\mathrm{f}}} \left\vert \dfrac{\beta_{\mathrm{f}}}{\hat{\beta}_{\mathrm{f}}} \right\vert^{m_{\mathrm{f}}} \beta_{\mathrm{f}}$
3. Linearize	$L[\mathcal{R}_{\mathrm{f}}(i)] = \mathcal{R}_{\mathrm{f}}(i) + \dfrac{\partial \mathcal{R}_{\mathrm{f}}(i)}{\partial \epsilon_{\mathrm{f}}^{v}} \Delta \epsilon_{\mathrm{f}}^{v}(i+1)$
4. Compute tangent	$\mathcal{K}_{\mathrm{f}}(i) = \dfrac{\partial \mathcal{R}_{\mathrm{f}}(i)}{\partial \epsilon_{\mathrm{f}}^{v}} = 1 + \Delta t \dfrac{\mu_{\mathrm{f}}(m_{\mathrm{f}}+1)}{\eta_{\mathrm{f}}} \left\vert \dfrac{\beta_{\mathrm{f}}}{\hat{\beta}_{\mathrm{f}}} \right\vert^{m_{\mathrm{f}}}$
5. Compute increment	$\Delta \epsilon_{\mathrm{f}}^{v}(i+1) = -\mathcal{K}_{\mathrm{f}}^{-1}(i) \mathcal{R}_{\mathrm{f}}(i)$
6. Update	$\epsilon_{\mathrm{f}}^{v}(i+1) \leftarrow \epsilon_{\mathrm{f}}^{v}(i) + \Delta \epsilon_{\mathrm{f}}^{v}(i+1) \quad \& \quad i \leftarrow i+1$
While	$\vert \mathcal{R}_{\mathrm{f}}(i) \vert \geq$ Tolerance

Table 3.1: Local Newton-Raphson iteration for the internal variable $\epsilon_{\mathrm{f}}^{v}$ (for i=f, s, n)

The whole Newton iteration step is described in Table 3.1. Note that in case $m_{\mathrm{f}} = 0$, the mentioned iteration is not required, instead, by making use of Equation (3.46), one obtains a closed-form expression for the viscous internal variable

$$\epsilon_{\mathrm{f}}^{v} = \frac{\epsilon_{\mathrm{f}}^{v}\vert_{t_{\mathrm{n}}} + \dfrac{\Delta t}{\eta_{\mathrm{f}}} \mu_{\mathrm{f}} (\epsilon_{\mathrm{f}} - \epsilon_{\mathrm{f}}^{a})}{1 + \dfrac{\Delta t}{\eta_{\mathrm{f}}} \mu_{\mathrm{f}}}. \tag{3.48}$$

3.3.2 Update algorithm for viscous-stretch in sheet and normal direction

The aforementioned recipe outlined from Equation (3.45) to Equation (3.48) with Table 3.1 is utilized for the update of the elastic stretches $\lambda_{\mathrm{i}}^{e} = \exp(\epsilon_{\mathrm{i}}^{e})$. Therein, the values for viscous-stretch in sheet and normal direction are updated as

$$\lambda_{\mathrm{i}}^{a} = 1 \qquad \text{leading to} \qquad \lambda_{\mathrm{i}}^{m} = \lambda_{\mathrm{i}}^{e} \lambda_{\mathrm{i}}^{v} \qquad \text{for} \qquad \mathrm{i} = \{\mathrm{s}, \mathrm{n}\}\,. \tag{3.49}$$

3.4 Algorithmic tangent moduli

Consequently, the visco-active part of the tangent moduli is achieved as

$$\mathbb{C}_{\mathrm{algo}}^{va} \coloneqq \Psi_{4\mathrm{f}}^{va\prime} \mathbb{F} + \Psi_{4\mathrm{s}}^{va\prime} \mathbb{S} + \Psi_{4\mathrm{n}}^{va\prime} \mathbb{N} \quad \text{with} \quad \mathbb{N} \coloneqq \boldsymbol{n} \otimes \boldsymbol{n} \otimes \boldsymbol{n} \otimes \boldsymbol{n}. \tag{3.50}$$

Therein, the deformation-dependent scalar visco-active moduli coefficients are defined as

$$\Psi_{4\mathrm{i}}^{va\prime} \coloneqq \frac{\hat{\mu}_{\mathrm{i}} - 2\sigma_{\mathrm{i}}}{I_{4\mathrm{i}}^{2}} \quad \text{with} \quad \hat{\mu}_{\mathrm{i}} = \mu_{\mathrm{i}} / \mathcal{K}_{\mathrm{i}}, \quad \text{for} \quad \mathrm{i} = \{\mathrm{f}, \mathrm{s}, \mathrm{n}\}. \tag{3.51}$$

3.5 Blood pressure in both ventricles

The heart is the most important muscular organ in the cardiovascular system and that pumps blood from the low-pressure venous side to the high-pressure atrial part in order

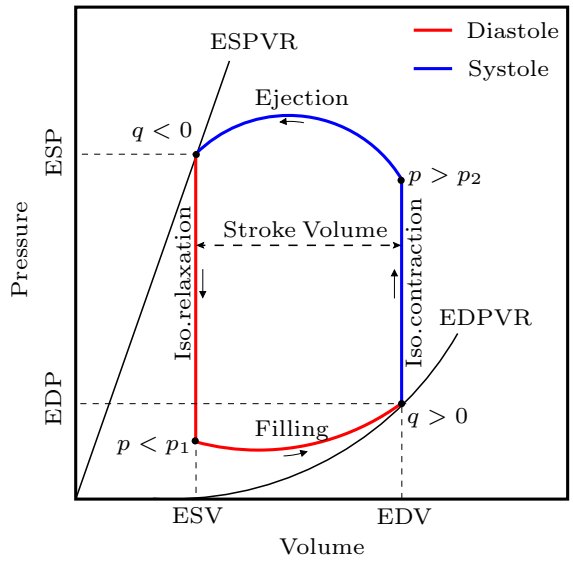

Figure 3.2: Pressure-Volume (PV) curve diagram of the ventricle during a normal cardiac cycle. Pressure-volume loop divided into 4 phases; isovolumetric contraction (systole), ejection (systole), isovolumetric relaxation (diastole), ventricular filling (diastole). The important clinical indices such as stroke volume (SV), end-diastolic volume (EDV), end-systolic volume (ESV), end-diastolic pressure (EDP), end-systolic pressure (ESP), end-diastolic pressure–volume relation (EDPVR) and end-systolic pressure–volume relation (ESPVR) are shown in the graph. Ejection fraction (EF) can be obtained as proportion of SV to EDV, i.e. SV/EDV. Switch conditions are shown as well. The phase shift from filling to isovolumetric contraction occurs if $q > 0$, from isovolumetric contraction to ejection if $p > p_2$, from ejection to isovolumetric relaxation if $q < 0$ and from isovolumetric relaxation to filling if $p < p_1$.

to circulate blood through the body so that all cells are provided with newly oxygenated blood and supplied by the proper nutrition in order to maintain the metabolism. To understand how cardiac function is achieved, one must comprehend the sequence of the mechanical events related to the pressure variation and the opening and closing valve. In the section, the contraction-relaxation characteristics of both ventricles roughly illustrated as well as the constitutive equations for computing ventricular blood pressure evolution are described.

3.5.1 Pressure-volume curve

For a healthy heart, the ventricle contracts and relaxes concurrently, and go through four different phases: isovolumetric contraction, ejection, isovolumetric relaxation, filling. The first two phases are classified as systole (contraction), the last two are labeled as diastole (relaxation), which are illustrated in Figure 3.2. It is assumed that the cardiac cycle starts from isovolumetric contraction as soon as the resting cardiomyocytes are provoked electrically. As the ventricles are depolarized the ventricular pressures rise rapidly without the ejection of blood into the aorta or pulmonary artery, which keep the volume of the ventricles constant. Thus, ventricular contraction in this phase is called “isovolumic” or “isovolumetric”. During this phase, some individual fibers shorten when they contract, whereas others generate force without shortening or can be mechanically stretched by the contracting cell around. This non-uniform contraction cause the geometry of ventricles changes significantly as the heart becomes more spheroid in shape. In this phase, the rate of pressure becomes maximal.

As the pressure in the ventricles rises, the semilunar valves are opened when the pressure

in the aorta and pulmonary artery is exceeded. Then, the semilunar valves open and the blood is ejected out of the ventricles. The ejection occurs as the total energy of the blood within the ventricles exceeds total energy of the blood in aorta. At the end of the phase, the ventricles has their own minimum volumes (ESV). The volume ejected in the phase is SV.

As the intraventricular pressures fall, the semilunar valves close. Since the total energy of blood within the ventricles is less than the energy of blood in the outflow tracts at this a point, systole ends and diastole begins. This phase is called isovolumetric relaxation. As the name suggests, the ventricular volumes remain constant (isovolumetric) during this phase and the ventricular pressure decreases because semilunar and AV valves are closed. The residual volume of blood that remains in a ventricle after ejection phase is ESV. The difference between the EDV and the ESV represents the SV of the ventricle. In a normal ventricle, about 50% or more of the EDV is ejected. The EF is obtained the SV divided by the EDV. When the ventricular pressure is lower than the atrial pressure, isovolumetric relaxation phase ends.

Then the AV valves open and ventricular filling begins. In this phase, the semilunar valves keep closed. Through the opened valves, the passive and rapid filling of the ventricles begins, which is accelerated by the high atrial pressures with decreased ventricular pressures. Once the ventricles are fully relaxed, their pressure begins to rise as they fill. The pressure at the end of the filling is EDP and the ventricles are filled to their EDV. The left ventricular EDV is associated with EDP.

3.5.2 Ventricular blood pressure evolution

In the following equations, 'lv' and 'rv' are replaced with 'v'. Also, the equations are applicable for both ventricles. Since the ventricular pressure is quasi-linearly dependent on the volume in isovolumetric phases and filling, the linear evolution law is given as

$$\dot{\hat{p}}_{\mathrm{v}} = \bar{\kappa}(\tilde{\theta} - \theta) \quad \text{with} \quad \tilde{\theta} \coloneqq \frac{\tilde{\mathcal{V}}}{\mathcal{V}_0} \quad \text{and} \quad \theta \coloneqq \frac{\mathcal{V}}{\mathcal{V}_0}. \tag{3.52}$$

Therein, $\bar{\kappa}$ is the material parameter having different values for each phase in order to enable the condition $\dot{\mathcal{V}} \approx 0$ during isovolumetric phases and $\dot{\hat{p}}_{\mathrm{v}} \approx 0$ during filling. Also, $\tilde{\theta}$, θ, $\tilde{\mathcal{V}}$ and $\mathcal{V}_0$ represent the dilatation at the end of the preceding phase, the current dilatation, the volume at the end of the previous phase and the volume of the ventricle cavity at the beginning of the cycle, respectively. By applying the implicit Euler method, the evolution equation for pressure is integrated as follows

$$\dot{\hat{p}} \approx \frac{\hat{p}_{\mathrm{v}} - p_{\mathrm{v}}|_{t_{\mathrm{n}}}}{\Delta t} = \bar{\kappa}(\tilde{\theta} - \theta) \quad \rightarrow \quad \hat{p_{\mathrm{v}}}(\mathcal{V}) = \bar{\kappa}(\tilde{\theta} - \theta)\Delta t + p_{\mathrm{v}}|_{t_{\mathrm{n}}}. \tag{3.53}$$

For the pressure evolution in the ejection phase, the three-element Windkessel model is applied

$$\dot{\hat{p}}_{\mathrm{v}} = \frac{1}{C_{ap}}\Big(1 + \frac{R_c}{R_p}\Big)q + R_c\,\dot{q} - \frac{\hat{p}_{\mathrm{v}}}{C_{ap}R_p} \quad \text{with} \quad q \coloneqq -\dot{\mathcal{V}}, \quad \dot{\mathcal{V}} \approx \frac{\mathcal{V} - \mathcal{V}_{\mathrm{n}}}{\Delta t} \quad \text{and} \quad \dot{q} = \frac{q - q_{\mathrm{n}}}{\Delta t}, \tag{3.54}$$

where the material parameters C_{ap}, R_c and R_p control the resistance and compliance properties of the blood flow and q depicts the outward blood volume rate from the ventricles. Similarly, the ventricular pressure is updated via the Euler integration method

$$\dot{\hat{p}}_{\mathrm{v}} \approx \frac{\hat{p}_{\mathrm{v}} - p_{\mathrm{v}}|_{t_n}}{\Delta t} \quad \rightarrow \quad \hat{p}_{\mathrm{v}}(\mathcal{V}) = \frac{(1 + R_c/R_p)q + C_{ap}(R_c\,\dot{q} + p_{\mathrm{v}}|_{t_n}/\Delta t)}{C_{ap}/\Delta t + 1/R_p} \tag{3.55}$$

Moreover, the equations for the sensitivity of $\hat{p}$ with respect to $\mathcal{V}$ for the ejection phase and the rest of the phases are

$$\hat{p}'_{\mathrm{v}} = -\frac{1 + R_c(1/R_p + C_{ap}/\Delta t)}{C_{ap} + \Delta t/R_p} \quad \text{and} \quad \hat{p}'_{\mathrm{v}} = -\bar{\kappa}\frac{\Delta t}{\mathcal{V}_0}. \tag{3.56}$$

Note that the negative sign in $\hat{p}'_{\mathrm{v}}$ equation occurs since the ventricular pressure is inversely proportional to the ventricular volume.

3.6 Current source

In this section, the electrical source term $\hat{F}^{\phi}$ is specified. For the phenomenological electrophysiology, it is helpful to set the model equations and parameters in the non-dimensional space. It is first devised the dimensionless transmembrane potential ϕ and dimensionless time τ through the following conversion formulation

$$\phi = \frac{\Phi + \delta_{\phi}}{\beta_{\phi}} \quad \text{and} \quad \tau = \frac{t}{\beta_t}\,. \tag{3.57}$$

The physical potential Φ is converted into dimensionless potential ϕ by using the constant β_{ϕ} and the potential difference δ_{ϕ}, which are measured in milivolt (mV). The unitless time τ is similarly related to the physical time t with the help of the scaling factor β_t measured in millisecond (ms). With the relation in Equation (3.57), the conversion equations are obtained as

$$\hat{F}^{\phi} = \frac{\beta_{\phi}}{\beta_t}\hat{f}^{\phi} \quad \text{and} \quad H = \frac{1}{\beta_t}h, \tag{3.58}$$

where $\hat{f}^{\phi}$ is the normalized source term described by a Fitzhugh-Nagumo type excitation equation, and the unitless counterparts $h = \partial_{\phi}\hat{f}^{\phi}$ of the physical tangent terms H in Equation (2.18). The normalized current source $\hat{f}^{\phi}$ is decomposed into two contributions, purely electrical part $\hat{f}^{\phi}_e(\phi, r)$ due to flow of ions across the membrane and mechano-electric feedback part $\hat{f}^{\phi}_m(\mathbf{g}; \boldsymbol{F}, \phi)$ due to stretch-activated-channels,

$$f^{\phi} = \hat{f}^{\phi}_e(\phi, r) + \hat{f}^{\phi}_m(\mathbf{g}; \boldsymbol{F}, \phi) \tag{3.59}$$

Analogously, the sensitivity of the normalized source term $h = \partial_{\phi}\hat{f}^{\phi}$ is also decomposed into two contributions as $h = \partial_{\phi}\hat{f}^{\phi}_e + \partial_{\phi}\hat{f}^{\phi}_m$.

3.6.1 Aliev-Panfilov model

For the computation of purely electrical part $\hat{f}^{\phi}_e$, Aliev-Panfilov model [32], which considers non-pacemaker cells by using two variables, is adopted. Also, the model favorably expresses the characteristic shape of the action potential in cardiomyocyte. Following two equations are used to calculate the transmembrane potential ϕ and the slow recovery variable r

$$\begin{aligned} \hat{f}^{\phi}_e =& \partial_{\tau}\phi = c\,\phi(\phi - \alpha)(1 - \phi) - r\phi + I, \\ \hat{f}^{r} =& \partial_{\tau}r = \Big[\gamma + \frac{\mu_1 r}{\mu_2 + \phi}\Big][-r - c\,\phi(\phi - b - 1)]. \end{aligned} \tag{3.60}$$

where c, α are material parameters. In Equation $(3.60)_2$, the coefficient term $[\gamma + \mu_1 r/\mu_2 + \phi]$ is to control the restitution characteristics of the model through μ_1, μ_2 and γ. Therein,

Φ, Φ_n and r_{n} are given
1. Calculate the dimensionless $\phi = (\Phi + \delta_\phi)/\beta_\phi$ in Eq.$(3.57)_1$
2. Set $r \leftarrow r_{\mathrm{n}}$
3. Calculate R^r and $\partial_r R^r$ in Eq.(3.62)
4. Update recovery variable $r \leftarrow r - [\partial_r R^r]^{-1} R^r$
5. Check if $\lvert R^r \rvert$ < TOL, if not, goto 3, continue otherwise
6. Update history for r_{n}
7. Compute $\partial_\phi R^r$ and $d_\phi r$ in Eq.(3.63)
8. Obtain f_e^ϕ in Eq.$(3.60)_1$ and $\partial_\phi f_e^\phi$ in Eq.(3.64)

Table 3.2: Local Newton raphson iteration for the internal variable r and determination of the corresponding source term f_e^ϕ and its linearization $\partial_\phi f_e^\phi$.

r is considered as an internal variable at gauss point level. Due to the non-linearity of the variable, a backward Euler integration is carried out to compute the current value of r at local material level. To perform this, following residual expression is required:

$$\mathrm{R}^r = r - r_n - \Delta\tau\Big[\Big[\gamma + \frac{\mu_1 r}{\mu_2 + \phi}\Big][-r - c\,\phi[\phi - b - 1]]\Big] \doteq 0 \tag{3.61}$$

Subsequently, to achieve the tangent term, it is required to find the derivative R_r in Equation (3.61) with respect to r,

$$\partial_r \mathrm{R}^r = 1 + \Delta\tau\Big[\gamma + \frac{\mu_1}{\mu_2 + \phi}[2r + c\,\phi + c\,\phi[\phi - b - 1]]\Big]. \tag{3.62}$$

The local update of the recovery variable r is done as $r \leftarrow r - [\partial_r \mathrm{R}^r]^{-1}\mathrm{R}^r$. Then $d_\phi r$ is calculated using the condition $d_\phi R^r = \partial_\phi R^r + \partial_r R^r d_\phi r \doteq 0$, where the partial derivative of R^r with respect to ϕ is

$$\partial_\phi R^r = \Delta\tau\Big[\Big[\gamma + \frac{\mu_1 r}{\mu_2 + \phi}\Big]\, c\,[\,2\phi - b - 1] - \frac{\mu_1 r}{[\mu_2 + \phi\,]^2}[\,r + c\,\phi[\phi - b - 1]]\Big] \doteq 0. \tag{3.63}$$

The tangent modulus regarding purely electrical part is then calculated as

$$\partial_\phi \hat{f}_e^\phi = c\,\Big[-3\phi^2 + 2[1 + \alpha]\phi + \alpha\Big] - r - \phi\; d_\phi r. \tag{3.64}$$

Table 3.2 summarizes the local Newton iteration to update the internal variable r and determines the corresponding source term f_e^ϕ and its linearization $d_\phi f_e^\phi$.

3.6.2 Mechano electric feedback

As described in Chapter 1, the electrical excitation trigger the contraction of the cardiomyocyte through the ECC. Furthermore, cardiac electrophysiological changes can also be triggered from a mechanical disturbance via MEF. Likely mediators of mechanoelectric feedback are stretch-activated ion channels (SACs) [33], which are opened in response to stretch in myocardium. The underlying mechanisms leading to SACs induced by stretching are not yet completely understood. Nevertheless, the pathophysiological role of cardiac

SACs is huge and, consequently, there are many clinical observations related to the cardiac MEF [7, 15, 17], such as stretch-induced ectopic excitation to mechanical induction of tachycardia and fibrillation. Besides, MEF is considered as a constituent part of the intrinsic electromechanical regulatory loop of the healthy heart [15, 34, 35]. Different mathmatical models for SACs are reported [36] for the several types of SACs such as cation permeable SACs [37] and potassium-selective one [38]. In the thesis, for the mechano electric feedback source term, the following mathematical model proposed in [22, 23, 39] is considered

$$\hat{f}^{\phi}_{\lambda_\mathrm{f}} = G_s \left\langle \lambda_\mathrm{f} - 1 \right\rangle (\phi_s - \phi) \tag{3.65}$$

where G_s is the maximum conductance and λ_f is the length of fiber at current time. 1 represent the length of fiber in undeformed setting. Since it is assumed that SACs is opened only under tension, Macaulay brackets are applied to enforce that the MEF is activated if $\lambda_\mathrm{f} > 1$. ϕ_s is the resting potential of the SACs. Under the tension, if the ϕ at the time of stimulation is below ϕ_s, SACs let the ion flux inward and results in depolarization. Despite the positive strain occur in the collagen of the myocardium, if the ϕ is above the resting potential, an outward (repolarizing) current ensues. This feature implies that the timing of stretch is important to create the premature depolarization in the myocardium.

In the formulation of MEF in Equation (3.65), SACs is simply related to the amount of stretch. In the thesis, reformulation of MEF is suggested based on physical observations as a novel aspect. Many studies indicates that SACs are dependent not only on the amount of stretch but also on the speed at which the stretch is applied [39, 40, 41, 42, 43]. Furthermore, it is hypothesized that the region with positive λ_f does not necessarily correspond to the region with positive $\dot{\lambda}_\mathrm{f}$, especially in case of viscoelastic simulation. Also, it is reported that stretch along cross fiber direction λ_s affects the cardiac behaviour, especially in infarcted heart [44].

Therefore, apart from Equation (3.65), the mathematical models for SACs in terms of $\dot{\lambda}_\mathrm{f}$ and λ_s are suggested for the MEF source term $\hat{f}^{\phi}_{m}$,

$$\begin{aligned} \hat{f}^{\phi}_{\dot{\lambda}_\mathrm{f}} &= G_s \left\langle \dot{\lambda}_\mathrm{f} \right\rangle (\phi_s - \phi) \quad \text{and} \\ \hat{f}^{\phi}_{\lambda_\mathrm{s}} &= G_s \left\langle \lambda_\mathrm{s} - 1 \right\rangle (\phi_s - \phi), \end{aligned} \tag{3.66}$$

where $\dot{\lambda}_\mathrm{f}$ is the strain rate calculated as $(\lambda_\mathrm{f} - \lambda_\mathrm{f}|_\mathrm{n})/\Delta t$ and λ_s is the stretch in cross fiber direction. Finally, the three different mathematical SACs models are used for the MEF source term $\hat{f}^{\phi}_{m}$ in the thesis. While the traditional SACs formulation in Equation (3.65) is taken into accounted only when the cardiomyocyte is in tension, MEF associated $\dot{\lambda}_\mathrm{f}$ Equation (3.66) turns on when current length of fiber is longer than the length in the previous step whether it is in tension or in compression. Moreover, due to the orthotropic characteristics of cardiomyocyte, it behaves distinctively in the cross fiber direction. Therefore, it is expected that both MEF reformulation bring the dissimilar electrophysiological effect throughout the heart. Next, the tangent terms of Equation (3.65) and Equation (3.66) are derived as

$$\begin{aligned} \partial_\phi \hat{f}^{\phi}_{\lambda_\mathrm{f}} &= -G_s \left\langle \lambda_\mathrm{f} - 1 \right\rangle, \\ \partial_\phi \hat{f}^{\phi}_{\dot{\lambda}_\mathrm{f}} &= -G_s \left\langle \dot{\lambda}_\mathrm{f} \right\rangle \quad \text{and} \\ \partial_\phi \hat{f}^{\phi}_{\lambda_\mathrm{s}} &= -G_s \left\langle \lambda_\mathrm{s} - 1 \right\rangle. \end{aligned} \tag{3.67}$$

With Equation (3.64) and Equation (3.67) in hand, the three different sensitivities of

Equation (3.59) are achieved as

$$h \coloneqq \partial_\phi \hat{f}^\phi = \begin{cases} \partial_\phi \hat{f}_e^\phi + \partial_\phi \hat{f}_{\lambda_\mathrm{f}}^\phi = c\,\big[-3\phi^2 + 2[1+\alpha]\phi + \alpha\big] - r - \phi\, d_\phi r - G_s\,\langle \lambda_\mathrm{f} - 1\rangle \\ \partial_\phi \hat{f}_e^\phi + \partial_\phi \hat{f}_{\dot{\lambda}_\mathrm{f}}^\phi = c\,\big[-3\phi^2 + 2[1+\alpha]\phi + \alpha\big] - r - \phi\, d_\phi r - G_s\left\langle \dot{\lambda}_\mathrm{f} \right\rangle \\ \partial_\phi \hat{f}_e^\phi + \partial_\phi \hat{f}_{\lambda_\mathrm{s}}^\phi = c\,\big[-3\phi^2 + 2[1+\alpha]\phi + \alpha\big] - r - \phi\, d_\phi r - G_s\,\langle \lambda_\mathrm{s} - 1\rangle\ . \end{cases} \tag{3.68}$$

Finally, the physical counterpart of Equation (3.59) and Equation (3.68) can be obtained by the conversion equations in Equation (3.58).

3.7 Electric flux

The electric potential flux $\hat{\boldsymbol{q}}$ represents the ion flow in a conductive medium that is induced by the potential difference between two points, describing the magnitude and direction of electrical charge. $\hat{\boldsymbol{q}}$ is assumed to linearly depend on the spatial potential gradient $\nabla\Phi$. Therefore $\hat{\boldsymbol{q}}$ is defined as

$$\hat{\boldsymbol{q}} = \boldsymbol{D} \cdot \nabla\Phi, \tag{3.69}$$

where $\boldsymbol{D}$ is the deformation-dependent spatial conduction tensor determining the conduction speed of the non-planar depolarization front in three-dimensional orthotropic cardiac tissue. Therefore, $\boldsymbol{D}$ is defined as

$$\boldsymbol{D} \coloneqq d_\mathrm{iso}\mathbf{g}^{-1} + d_\mathrm{ani}\boldsymbol{f} \otimes \boldsymbol{f}. \tag{3.70}$$

Therein, isotropic d_iso and anisotropic d_ani are conductivity speed.

4 Numerical examples

This chapter is devoted to demonstrate the effect of MEF by use of representative examples with the coupled electromechanical analysis established in the Chapter 2 and Chapter 3 that formulates the main physiological features of the overall response of the heart as well as the two way coupling; ECC and MEF. Firstly, the influence of MEF on cardiac action potential (AP) and dispersion of repolarization (DR) are examined at cell scale with the analysis of the rectangular bar of heart tissue. Secondly, normal cardiac cycles under MEF are simulated with the intact biventricular heart model. Furthermore, the MEF is formulated not only in terms of λ_{f} but also is reformulated in consideration of the strain rate along fiber direction ($\dot{\lambda}_{\mathrm{f}}$) and the cross fiber stretch in sheet fiber direction λ_{s}, as a novel aspect. As previously mentioned, the velocity at which stretch is applied has influence on MEF. It is also reported that the variation of cross fiber stretch in cardiac muscle cell has an impact on MEF. The variations of the cardiac electrophysiology and the cardiac performance are probed by AP, ECG and v-t curve which are recorded during the normal cardiac cycles. Moreover, VF(ventricular fibrillation) by application of moderate mechanical impact (Commotio cordis) and the termination of the VF by a mechanical impact (precordial thump) [**a**]re simulated with the biventricular heart model. Lastly, it is exemplified how the sudden increase of preload in the left ventricle affects the cardiac output and electrophysiology. The pressure, volume and the electrical flux are simultaneously recorded during cardiac cycles. Unless stated otherwise, the values of the Table 4.1 are used for the electromechanical analysis in the next sections. Particularly, in the heart simulations, the parameters for the electrophysiology are chosen to result in depolarization and repolarization phases fit well in following cardiac cycles each taking 800 ms. The elastic cases are formulated by assigning $\eta_{\mathrm{f}} \to \infty\,\mathrm{kPa\,s}$, $\mu_{\mathrm{s}} = 0\,\mathrm{kPa\,s}$ and $\mu_{\mathrm{n}} = 0\,\mathrm{kPa\,s}$.

4.1 MEF at cell-scale

This section investigates the influence of MEF in Equation (3.65) on the cardiac rectangular segment ($5\,\mathrm{mm} \times 5\,\mathrm{mm} \times 20\,\mathrm{mm}$) of the heart tissue by using the coupled finite element analysis using time steps of $\Delta t = 1\,\mathrm{ms}$. To perform this, 4 sets of simulations are consdiered: the elastic formulation without MEF application (EX), the viscoelastic formulation without MEF application (VX), the elastic formulation with MEF application (EM) and the viscoelastic formulation with MEF application (VM). For each of these sets, three different discretizations with element number 5, 10 and 20 are considered. So, in total 12 simulations are performed to assess the MEF effect. An example of geometry, the cardiac tissue segment consisting of 10 elements are shown in Figure 4.1**A**. As mechanical boundary conditions, the nodes on the plane $x = 0\,\mathrm{mm}$ in all direction are fixed and all the remaining nodes are constrained with directional linear springs having stiffness values as $k_{\mathrm{x}} = k_{\mathrm{y}} = k_{\mathrm{z}} = 8 \cdot 10^{-4}\,\mathrm{N/mm}$. The required parameters are taken from Table 4.1, except for $\gamma = 0.0002$. The transmural variation of the fiber directions is not considered as all the fibers in each element are aligned along x-direction. The depolarization planar wave fronts are commenced on the left edge ($x = 0\,\mathrm{mm}$) where the initial transmembrane potential value was assigned as $\Phi = -40\,\mathrm{mV}$ at $t = 0\,\mathrm{ms}$. Except these nodes, the remaining nodes are electrically in a resting state $\Phi = -80\,\mathrm{mV}$. As the nodes assigned as $\Phi = -40\,\mathrm{mV}$ at

Passive stress	$\kappa = 50$ kPa, $a = 0.309$ kPa, $b = 9.194$ [−]
	$a_\mathrm{f} = 12.093$ kPa, $a_\mathrm{s} = 1.383$ kPa, $a_\mathrm{fs} = 0.272$ kPa
	$b_\mathrm{f} = 20.407$ [−], $b_\mathrm{s} = 19.476$ [−], $b_\mathrm{fs} = 12.266$ [−]
Visco-active stress	$\mu_\mathrm{f} = 75.382$ kPa, $\mu_\mathrm{s} = 18.874$ kPa, $\mu_\mathrm{n} = 9.37$ kPa
	$\eta_\mathrm{f} = 98.157$ kPa s, $\eta_\mathrm{s} = 59.157$ kPa s, $\eta_\mathrm{n} = 29.793$ kPa s
	$m_\mathrm{f} = 0$ [−], $m_\mathrm{s} = 0$ [−], $m_\mathrm{n} = 0$ [−]
Calcium concentration	$k_1 = 0.008$ [−], $\zeta = 0.01$ [−], $p = 3$ [−]
Myocardial contraction	$k_2 = 0.025$ [−], $\xi = 0.030$ [−], $q = 0.001$ [−]
Excitation	
Aliev-Panfilov model	$\alpha = 0.01$ [−], $b = 0.1$ [−], $c = 8$ [−], $\gamma = 0.0005$ [−]
	$\mu_1 = 0.15$ [−], $\mu_2 = 0.3$ [−]
Mechano electric feedback	$G_s = 80$ [−], $\phi_\mathrm{s} = 0.5$ [−]
Conversion	$\beta_\phi = 100$ mV, $\delta_\phi = 80$ mV,$\beta_t = 12.9$ ms
Conduction	$d_\mathrm{iso} = 0.5$ mm^2/ms, $d_\mathrm{ani} = 5.0$ mm^2/ms
Ventricular pressure	
Isovolumetric contraction	$\bar{\kappa} = 500\,\mathrm{mmHg/ms}$
Ejection	$R_p = 1\,\mathrm{mmHg\,ms/mm^3}$, $R_c = 10^{-3}\,\mathrm{mmHg\,ms/mm^3}$
	$C_{ap} = 800\,\mathrm{mm^3/mmHg}$
Isovolumetric relaxation	$\bar{\kappa} = 2000\,\mathrm{mmHg/ms}$
Filling	$\bar{\kappa} = -0.05\,\mathrm{mmHg/ms}$
Switch pressures	$p_1 = 10\,\mathrm{mmHg}$, $p_2 = 70\,\mathrm{mmHg}$.

Table 4.1: Parameters used in the simulations

$t = 0\,\mathrm{ms}$ are depolarized, the potential difference between the transmembrane potential at the depolarized nodes and $-80\,\mathrm{mV}$ at the remaining nodes causes the planar depolarization wave front. The results of 12 simulations are shown in Figure 4.1**B**.

4.1.1 Dispersion of repolarization

Dispersion of repolarization (DR) has been defined as the difference between longest and shortest repolarization time in one area or segment and another [9, 45]. In intact heart, proper ejection of blood is achieved by relatively synchronous contraction of the cardiac cells [7]. Also, the DR in intact heart is small, but normally big enough to give the vectors for the T wave of the ECG [46], which is the most vulnerable area to the electrical and mechanical perturbation [19, 20]. Reentry is the most likely mechanism of arrhythmias facilitated by DR [47, 48]. In the subsection, the effect of MEF on the DR is investigated.

Set	Elastic		Elastic+MEF		Viscoelastic		Viscoelastic+MEF	
Elements	APD80	DR	APD80	DR	APD80	DR	APD80	DR
5	629.1	86.8	601.5	59.2	629.2	86.9	618.2	75.9
10	704.0	161.7	611.6	69.3	704.1	161.8	635.5	93.2
20	784.8	242.5	617.0	74.7	784.9	242.6	637.9	95.6

Table 4.2: The APD80 and the dispersion of repolarization in [ms]. DR is calculated by subtracting the time at which APD80 occurs in the first node from the time at which APD80 occurs in last node. The time of APD80 of the first node obatined in each simulation was not displayed in the table due to the negligible differences between them (542.3 ms is used as the representative value). Linear interpolation enables the value to have one decimal place.

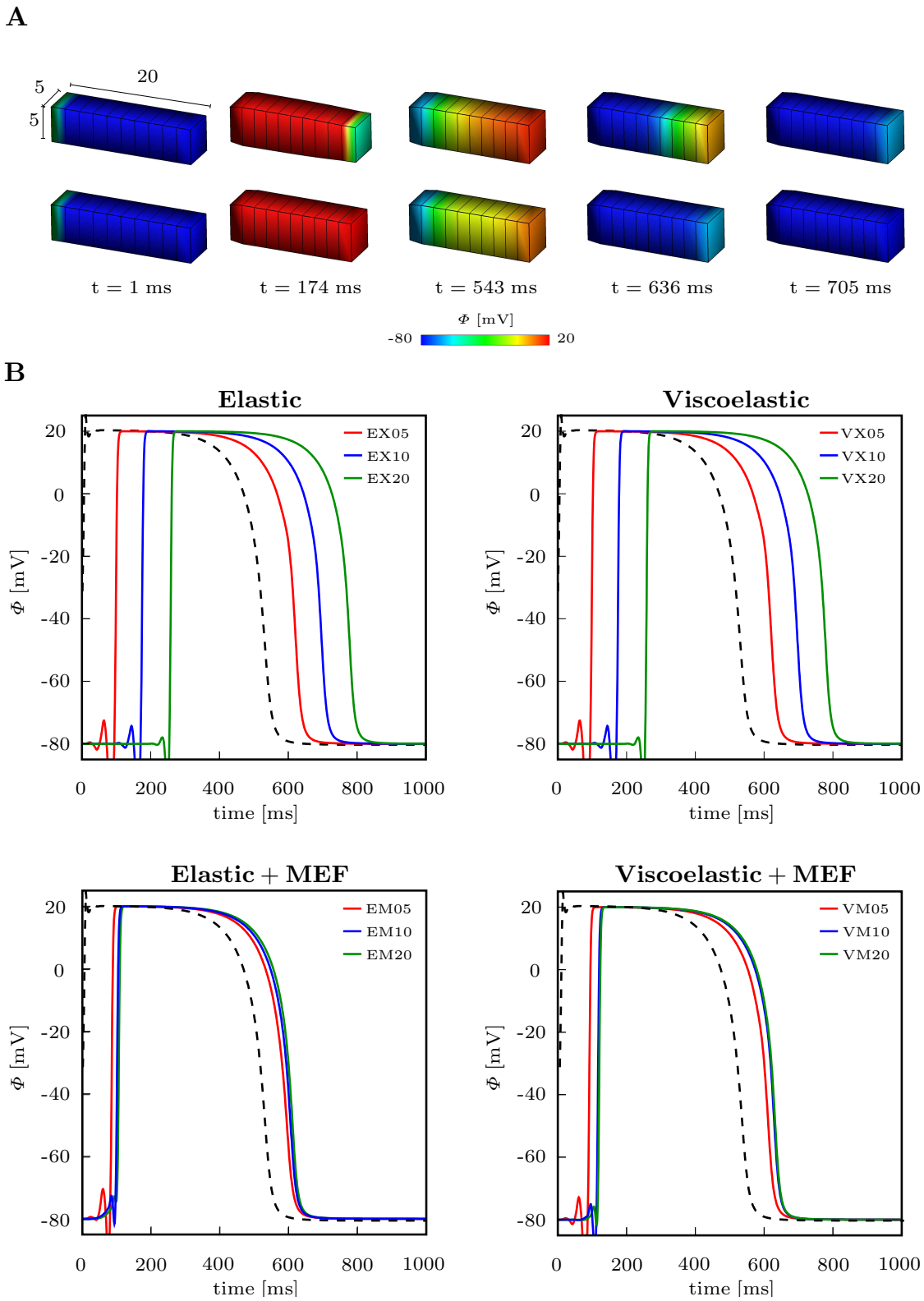

Figure 4.1: **A** : Polarization of the viscoelastic 10 element bar tissue without MEF effect (top panel) and with MEF effect (bottom panel). **B** : Cardiac APs. A family of curves describing cardiac AP are plotted in each graph. The AP drawn with black-dashed line represents 3 AP curves occuring at the first node of 3 different geometries. Solid-colored lines represent the AP occuring at the nodes placed at the end of the segment. The gap between colored-solid lines and the black-dashed line means the DR. When MEF adopted, due to the reduction of the dispersion, the cells are contrating in more coordinated and synchronized way.

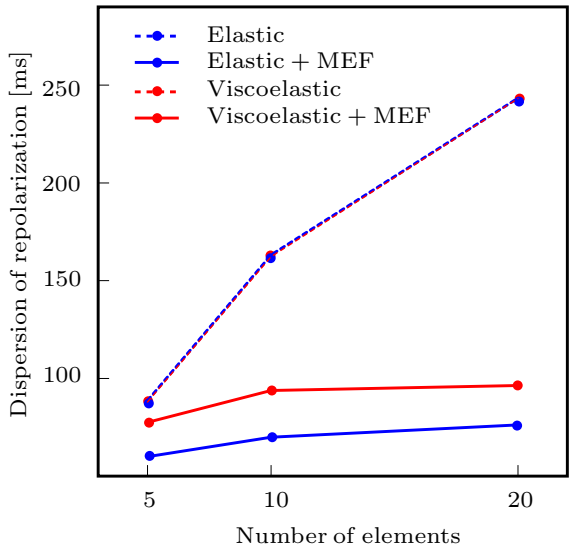

Figure 4.2: Result of the DR study. Regardless of the material property, finer mesh has more significant increase in the DR. However, when MEF is considered, the decline of the DR is observed. The values are displayed in Table 4.2.

To do so, two APs are considered: First one occurring at the first node located at the left edge ($x = 0\,\text{mm}$), and an AP occuring at the last node located at the right edge ($x = 20\,\text{mm}$). The implementation of the AP of the first node gives the shortest repolarization time and the other AP provides the latest repolarization time, which enables to monitor that how long it takes to activate the entire bar and the DR. As mentioned in section 4.1, the excitation of the bar is commenced at the first node so the last node located farthest will be the last one to be activated. Note that one of the critical features of the myocardium that the cell depolarized earlier will be repolarized later [49] is not implemented. The implemented APs of the four different sets are shown in Figure 4.1**B** in which the colored-solid lines represent the AP with different refinement level occuring in the last element and the black-dashed line depicts the AP in first element. The APs recorded in the first node are the same regardless of the discretization level. So, in each figure, only one AP was drawn for the first nodes on behalf of the three discretization level's APs. First, in the both "Elastic" and "Viscoelastic" cases in which MEF was not engaged in Figure 4.1**B**, the DR is increased as the geometry becomes finer despite the same length of the bar. The snapshots of the transmemembrane potential by the simulations of VX10 (top) and VM10 (bottom) are depicted in Figure 4.1**A** and each corresponding AP is depicted in the top-right and bottom-right panel with blue-solid color in Figure 4.1**B**, respectively. In the simulations of VX10, the first node is depolarized at time $t = 1\,\text{ms}$ and then starts to activate the adjacent nodes. The last element starts to depolarize 174 ms later than the first node. At $t = 542.3\,\text{ms}$, the transmembrane potential of the first node decreases to 80% of its peak value and the APD80 of the last node occurs at $t = 704.5\,\text{ms}$ therefore the DR is $162.2\,\text{ms}$ $(704.5 - 542.3)$ in the bar tissue (VX10). However, if MEF operates, the electrophysiology of the bar changes. As the first element begins to contract at time $t = 1\,\text{ms}$, the contraction causes stretch all elements over the bar tissue and then the adjacent elements also causes stretch all elements. This mechanism sequentially takes place on every element. Consequently, the resultant stretch developed in the last element drives the voltage-charged ion flux into myocyte through SACs, which does not develop in the absence of MEF effect. In the VM10 bar, APD80 of the first node occurs at $t = 542.3\,\text{ms}$ and the APD80 of the last node occurs at $635.5\,\text{ms}$ therefore the DR is

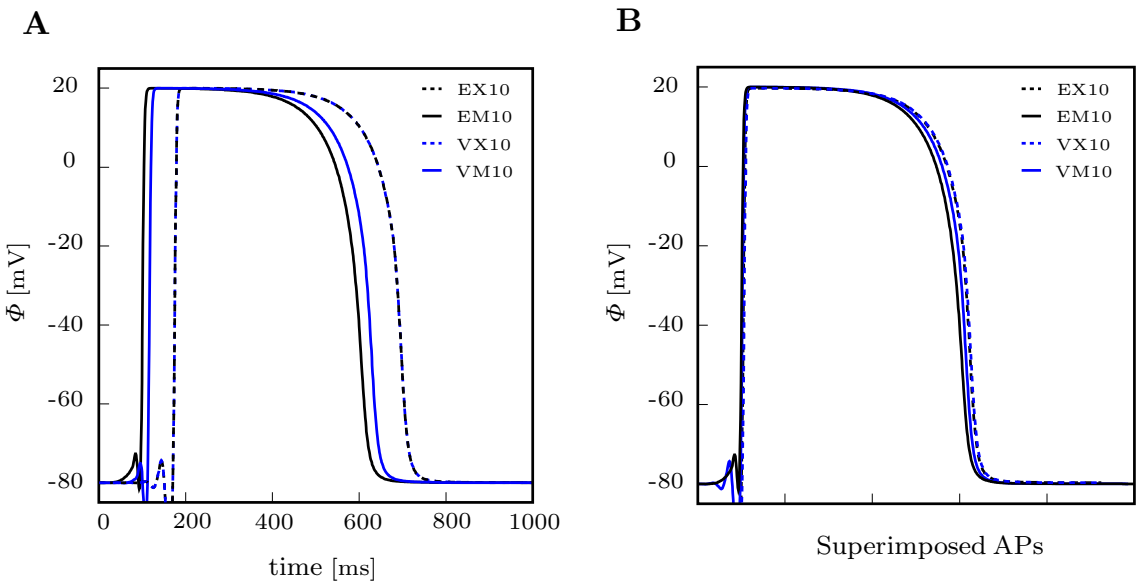

Figure 4.3: **A** : AP simulations with 10 elements bar tissue. Solid lines represent the MEF applied simulations. APs with dashed lines are from simulation without MEF. Excluding MEF effect, APs are nearly the same regardless of material properties. However, when MEF operates, the small discrepancy occurs due to the delayed response of viscoelastic cardiomycytes. Since the elastic myocardium immediately responses to the stretch, the depolarization by SACs occurs slightly earlier than the dipolarization of the viscoelastic one. **B** : In order to compare the morphology and the AP duration, the APs were superimposed. The two APs with MEF effect have the shorter APD than the other two cases without MEF. Also, the steeper repolarization gradients are observed. Between the APs with MEF, the APD of viscoelastic formulation is longer than that of the elastic one. The changes affect the ECG.

93.2 ms (635.5 − 542.3). Hence, the time to activate the entire bar is decreased and the reduced DR is obtained when considering MEF. The DR can be observed in the other sets of simulations as well, which are summarized in Table 4.2 and in the Figure 4.2. In the simulations without MEF, only cell-to-cell conduction is responsible for the activation of the bar. Therefore, the DR increases as the mesh is refined. Under MEF effect, the bar is activated not only by the cell-to-cell conduction but also by SACs due to the mechanical deformation, which leads to reduction of the time to activate whole bar, the decline in the DR, and consequently the more coordinated contraction. SACs due to MEF in the myocardium depolarize the near elements while the triggered stretch does not affect the excitation of the elements in the absence of MEF. The stretches affect the electrical activity in all elements over the bar almost simultaneously. Therefore, all elements undergo the contraction and the relaxation in more synchronized and coordinated way regardless of the segment's level of discretization. The harmonized contraction of the heart is one of the important factor to circulate blood through whole body, and MEF contributes to the coordination by decreasing the DR.

4.1.2 Impact of material property

In the previous subsection, it is explained how MEF influences on the AP and DR. In this subsection, the impact of material properties on the electrophysiological events of the bar tissue is evaluated according to existence of MEF. The results are plotted in Figure 4.3 in which solid-blue and solid-black represent viscoelastic formulation with MEF and elastic one with MEF, respectively. Dashed-blue and dashed-black represent viscoelastic formulation without MEF and elastic one without MEF, respectively. If MEF is not operated,

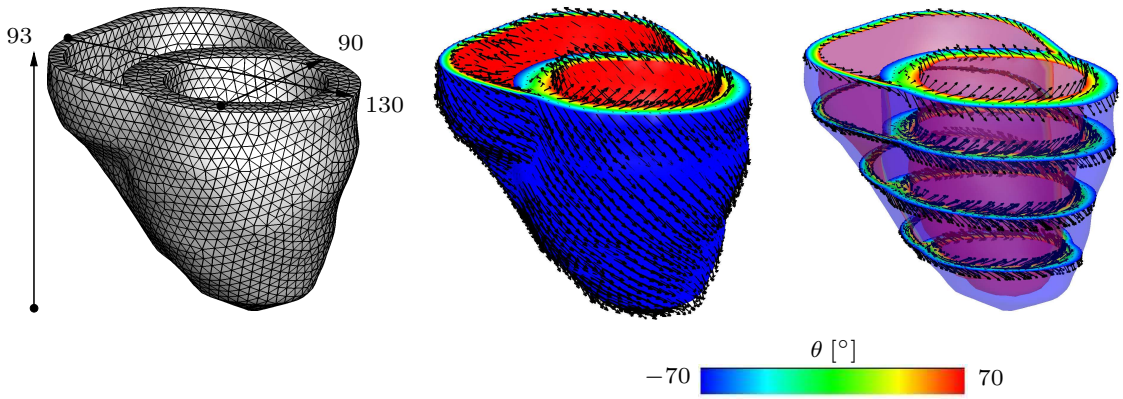

Figure 4.4: The virtual biventricular model of a healthy person, discretized by 25366 tetrahedral elements over 6270 nodes with 1758 triangular surface elements on the endocardial inner surface. A 38 years old healthy volunteer's (male) biventricles are virtualized. All lengths are in millimetres. Fiber angle at epicardial surface is set to $-70°$. Endocardial surface's fiber angle is $70°$. The fiber angle values between epicardium and endocardium are interpolated by Equation (4.1).

there is hardly any differences found between the elastic formulation and viscoelastic one as it can be seen that the two APs with dashed-lines are the same. In contrast, when comparing the simulations under MEF effect, the small difference is observed between viscoelastic and elastic formulations. It can be noticed that the electrophysiological events of elastic material occurs earlier than viscoelastic one. The depolarization of the last node is developed by SACs. In elastic formulation, the tension is developed as soon as the contraction occur. In viscoelastic formulation, the opening of SACs is delayed due to the delayed response to the tension, thereby the depolarization and repolarization are started later than elastic formulation. Furthermore, the graphs are superimposed in Figure 4.3**B** in order to investigate the AP morphology and the APD. The two solid lines, where MEF is considered, have the shorter APD with the steeper gradient in the repolarization phase than the APD observed in the two dashed lines. Under MEF, the material property also alters the AP morphology. In the elastic case (EM10), it is possible to observe the more shortened duration of plateau and the slightly ealier start of repolarization with the steeper gradient. Although they are not remarkable in a single cardiac cell level, the features could affect the electrophysiological behaviour of heart consisting of numerous cardiac cells. For example, the steeper gradient of repolarization and the shortend plateau in AP could shorten the QT interval in ECG.

4.2 MEF with biventricular heart model

MEF, the process by which mechanical forces on the myocardium can alter its electrical properties, is known to underlie many cardiac arrhythmia associated with pathological conditions [8, 9]. In this section, the simulations using the finite element framework of a biventricular heart model of a healthy person are presented. The biventricular heart geometry virtualized through cardiac magnetic resonance imaging (cMRI) is adopted to the analysis in the section. The geometry in Figure 4.4 is discretized by 25366 tetrahedral elements over 6270 nodes. Also, the model includes 1758 triangular surface elements on the endocardial surface of its left ventricle for measuring the volume cavity. The fiber orientation angle (θ) at material level devised by linear interpolation, thereby the myofiber alignment is varied from $70°$ in the endocardium, the inner wall $-70°$ in the epicardium,

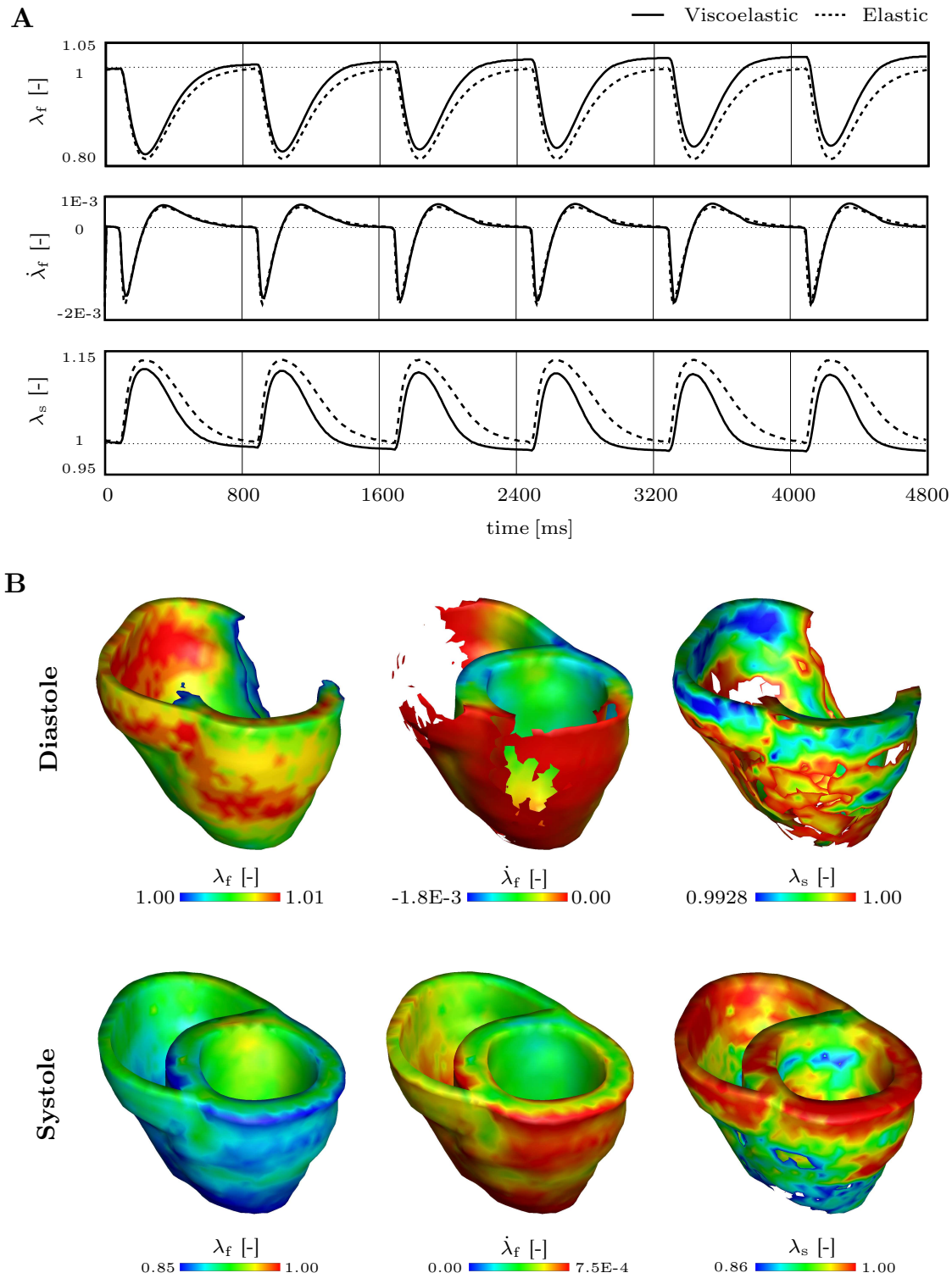

Figure 4.5: **A** : A single cell simulation located at the epicardial surface of LV for the exemplificaion of how λ_f, $\dot{\lambda}_f$ and λ_s stabilize over the normal cardiac cycles. The excitation is initiated with an external stimulus I = 5 [-] every 800ms. The variation of stretch is repeated as cycles proceed in elastic formulation. In viscoelastic formulation, the degree of stretch varied as cycles proceed due to the residual stretched brought by viscous effect. The stretch is saturated after enough cycles. **B** : The regions that contribute to MEF in which the contour shows λ_f, $\dot{\lambda}_f$ and λ_s at certain time during diastole (top) and systole (bottom). In diastolic state the regions undergo the tension in fiber direction ($\lambda_f > 1$) are coincides with the regions that experience the positive strain rate in fiber direction ($\dot{\lambda}_f < 0$) and the compression in the cross fiber direction ($\lambda_s < 1$). The opposite occurs in the systole state.

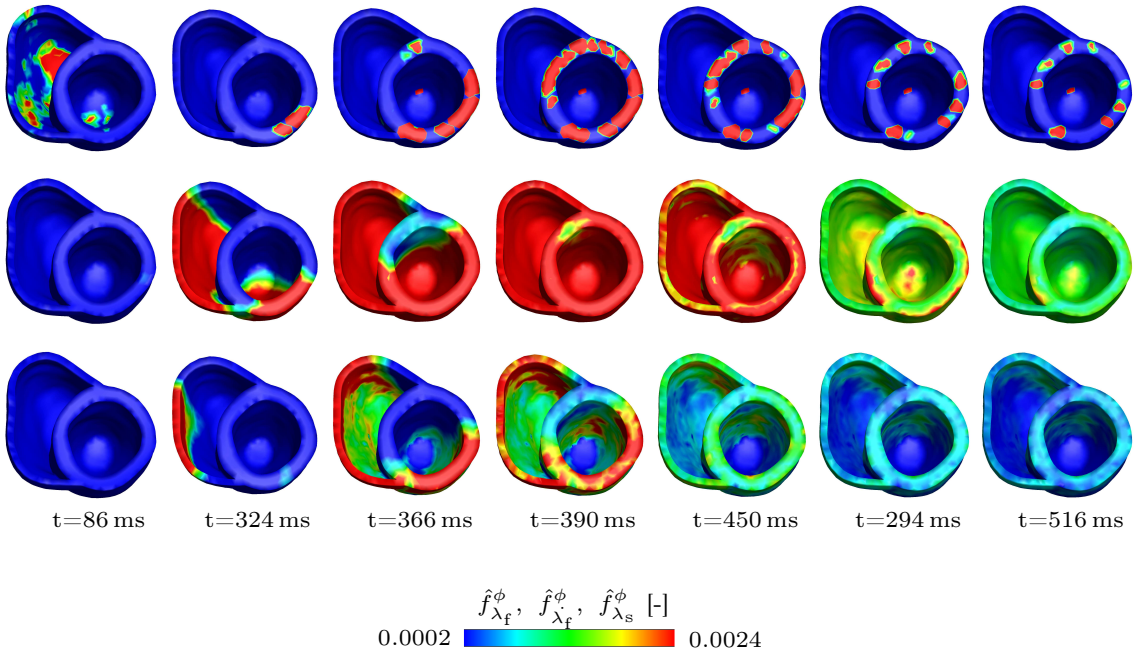

Figure 4.6: Snapshots of the contour at different time during the normal cardiac cycle are generated based on the three MEF cases: $\hat{f}^{\phi}_{\lambda_f}$ (first row), $\hat{f}^{\phi}_{\dot{\lambda}_f}$ (second row) and $\hat{f}^{\phi}_{\lambda_s}$ (third row). They are activated in the varied regions at the same time, which consequnetly affects the cardiac electrophysiology.

the outer wall. The angle is calculated by using the following formulation

$$\theta = \theta_{\text{en}} + (\theta_{\text{ep}} - \theta_{\text{en}}) \frac{d_{\text{en}}}{d_{\text{en}} + d_{\text{ep}}}, \tag{4.1}$$

where θ_{en} and θ_{ep} are the fiber angle prescribed on the endocardium and epicardium surface, while d_{en} and d_{ep} represent the distance to the endocardium and epicardium, correspondingly. Initially all the myocardial tissue is electrically in the resting state $\Phi_0 = -80\,\text{mV}$. Occurence of electrical stimulus ($I = 5$) triggering heart contraction is set every 800 ms for 10 ms on the nodes placed upper part of the septum corresponding AV node. A constant time-step is set as $\Delta t = 2\,\text{ms}$ in all simulations. Linear springs are attached to the nodes at basal and epicardial surface, having stiffness values, respectively, $k_{\text{x}} = k_{\text{y}} = k_{\text{z}} = 10^{-3}\,\text{N/mm}$ at the nodes basal surface $z = 0$, and $k_{\text{x}} = k_{\text{y}} = k_{\text{z}} = 10^{-4}\,\text{N/mm}^2$ at the nodes corresponding to the epicardium. The normal cardiac cycles are simulated with the biventricular model in order to investigate the influence of MEF on the intact heart in Section 4.2.1. In Section 4.2.2, ventricular fibrillation (VF) by "Commotio cordis" is simulated on the biventricular heart and the termiation of VF is simulated afterwards by precordial mechanical impact as well.

4.2.1 Influence of MEF on normal cardiac cycles

In this section, MEF effect on a intact biventricular heart is evaluated during normal cardiac cycles with the elastic and the viscoelastic material properties. During each simulation the corresponding ECGs and v-t curves are recorded with the different G_{s} values. Therefore, it can be scrutinized that the clinical contribution of MEF on normal cycles of intact heart. Before appliying MEF effect on the heart, it is required to saturate the

primary field variables on the material points to a closely constant value. This process is conducted first in the transmembrane potential field. To perform this, 6 cycles were performed with all nodes mechanically constrained. After the cycles, the electrical field is stabilized and the field variable becomes nearly the same with the previous cycle. Also, a regular ECG is observed. Then, the mechanical deformation field is saturated without the constraints until the electromechanical state of the material points is almost the same with the previous cycle. The variations of λ_{f}, $\dot{\lambda}_{\mathrm{f}}$ and λ_{s} at the single cell located in the epicardial surface of LV are obtained and illustrated in Figure 4.5**A**. While the same values are repeated every cycle in all elastic formulation, viscoelasticity of the myocardium causes the residual stretches that induce the gradual increase in λ_{f} and the gradual decrease in λ_{s} approaching asymptotic values. Moreover, it is observed that the range of $\dot{\lambda}_{\mathrm{f}}$ becomes wider. Also, the horizontal symmetry is observed between λ_{f} and λ_{s} because the decreases in the fiber spacing occur as the fibers lengthen.

It is worth to reformulate MEF in terms of $\dot{\lambda}_{\mathrm{f}}$ and λ_{s} and to compare the results with the MEF formulated in terms of λ_{f} adopted in most studies. The virtualized biventricular heart model exhibits that most of its regions with λ_{f} in tension are not always consistent with the regions with positive $\dot{\lambda}_{\mathrm{f}}$. The areas under compression undergo a positive $\dot{\lambda}_{\mathrm{f}}$ while the regions under tension experience negative $\dot{\lambda}_{\mathrm{f}}$. These inconsistency is more clearly visible especially under viscoelastic formulations due to its time-dependent response. Also, the mathematical model for SACs is reformulated by considering λ_{s} based on the studies that reveal λ_{s} might also contribute to MEF, especially in the presence of the infarcted regions [44]. The contour plots of λ_{f}, $\dot{\lambda}_{\mathrm{f}}$ and λ_{s} are shown in Figure 4.5**B** in which the top panel shows the contour of λ_{f}, $\dot{\lambda}_{\mathrm{f}}$ and λ_{s} in diastolic state. The left shows the contour plot of λ_{f} where most cells undergo tension along $\boldsymbol{f}$ ($\lambda_{\mathrm{f}} > 1$). However, the elements have negative $\dot{\lambda}_{\mathrm{f}}$ value (middle) and are under compression in the direction of $\boldsymbol{s}$ ($\lambda_{\mathrm{s}} < 1$) at the same time. The bottom panel shows the heart model experiencing the systole. Similarly, the elements are in compression along $\boldsymbol{f}$ (left), have positive strain rate along $\boldsymbol{f}$ (middle) and in tension along $\boldsymbol{s}$ (right). Therefore, the introduction of $\dot{\lambda}_{\mathrm{f}}$ and λ_{s} into MEF may manifest different characteristics than MEF in terms of λ_{f}, with which finally the heart will behave electrophysiologically in different way.

With the electromechanically saturated heart after sufficient cycles, the Equation (3.65) and Equation $(3.66)_2$ are modified. Finally, for viscoelastic simulation, the $\hat{f}^{\phi}_{\mathrm{m}}$ in terms of λ_{f}, $\dot{\lambda}_{\mathrm{f}}$ and λ_{s} are respectively,

$$\begin{aligned} \hat{f}^{\phi}_{\lambda_{\mathrm{f}}} &= G_s \left\langle \lambda_{\mathrm{f}} - \lambda'_{\mathrm{f}} \right\rangle (\phi_s - \phi), \\ \hat{f}^{\phi}_{\dot{\lambda}_{\mathrm{f}}} &= G_s \left\langle \dot{\lambda}_{\mathrm{f}} \right\rangle (\phi_s - \phi) \quad \text{and} \\ \hat{f}^{\phi}_{\lambda_{\mathrm{s}}} &= G_s \left\langle \lambda_{\mathrm{s}} - \lambda'_{\mathrm{s}} \right\rangle (\phi_s - \phi). \end{aligned} \tag{4.2}$$

Therein, λ'_{f} and λ'_{s} are the saturated stretch values achieved at the beginning of a certain cycle having different value in every element. The 1 representing the initial fiber length in the Equation (3.65) and Equation $(3.66)_2$ are replaced by the saturated stretch because each fiber does not return to the initial state due to the residual stretch and does not have the same values in each element. With Equation (4.2) at hand, the three cases of MEF are applied on the biventricular heart during normal cycles. The cycles with MEF application are also simulated until the electromechanical values are stabilized. As expected, the three MEF based on λ_{f}, $\dot{\lambda}_{\mathrm{f}}$ and λ_{s} affects locally the different regions of the heart model during the cycle. MEF formulated by λ_{f} mostly affect the right ventricle during diastole and the base to which the stiffer spring attached during systole. MEF in terms of $\dot{\lambda}_{\mathrm{f}}$ and λ_{s} also have impacts on heart differently as shown in Figure 4.6.

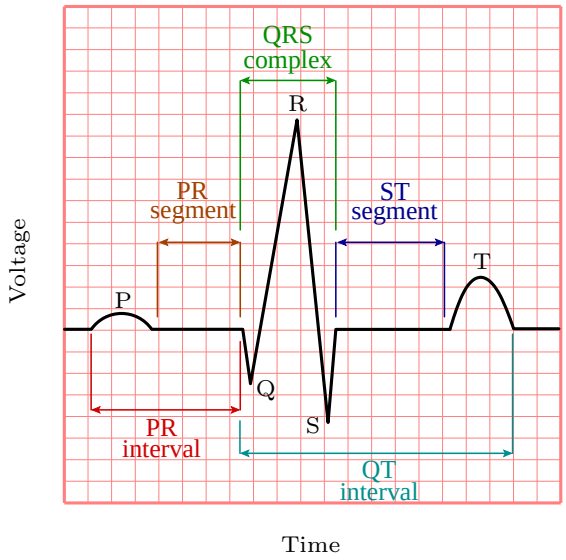

Figure 4.7: Schematic representation of ECG. The first deflection (P wave) is associated with right and left atrial depolarization. In the thesis, the heart models without atria does not show P wave The QRS complex representing ventricular depolarization. ST segment is the reflection of the current flow associated with phase 2 of ventricular repolarization. Since there is no current flow during this plateau phase of repolarization, the ST segment is normally isoelectric with the baseline ($\Phi = 0\,\mathrm{mV}$). The T wave means the current of rapid phase 3 ventricular repolarization.

Simulation of ECG

The electrical activity of heart can be visualized by the non-invasive technique, Electrocardiogram (ECG). The analysis of ECG is widely used for the diagnostic of cardiac diseases [50]. The sooner is the detection of arrhythmias, the greater is the chance of recovery because life-threatening arrhythmias were usually preceded by less-severe premonitory arrhythmias [51, 52]. A typical ECG is shown in Figure 4.7. It is known that the changes in duration of the QT interval are related to certain pathologies. The duration of QRS complex is concerned with the status of the myocardial conduction system. The measurements on the ECG are mostly defined by the characteristic extrema, amplitudes, wave morphologies and intervals of time between extrema points [50]. The ECG curves are generated by the integration of the electric flux $\boldsymbol{q}$ at all over the domain in actual configuration, i.e $\int_{\mathcal{B}_t} \boldsymbol{q} dv$. The projection of the heart vector changing over time onto different directions produces the differnt shape of ECGs. In the thesis, all the ECGs are recorded along lead II vector from the base of the septum to the apex. In the real heart, the APD of cardiac muscle cells in the endocardium is almost twice as large as the APD of epicardial cells [49]. Therefore, the cells nearby AV node will be the last cells repolarize and the outer lying cells have shorter APD. In order to establish this crucial feature of the AP of cardiac cells, the scaling factor β_t is formulated as

$$\beta_t = 12.9 \left[1 - t^{\mathrm{act}} \frac{0.6}{100} \right]. \tag{4.3}$$

Therein, t^{act} is the elapsed time the transmembrane potential reaches -50 mV after the excitation at AV node. The cell to which the wave front reaches sooner has the smaller t^{act} and the bigger β_t, which allows the APD of the cell to be longer. As shown in Figure 4.8**A**, the cells at the varied area of the heart are depolarized at different time as the front wave begins to travel at the AV node. The cell located nearby AV node starts to depolarize

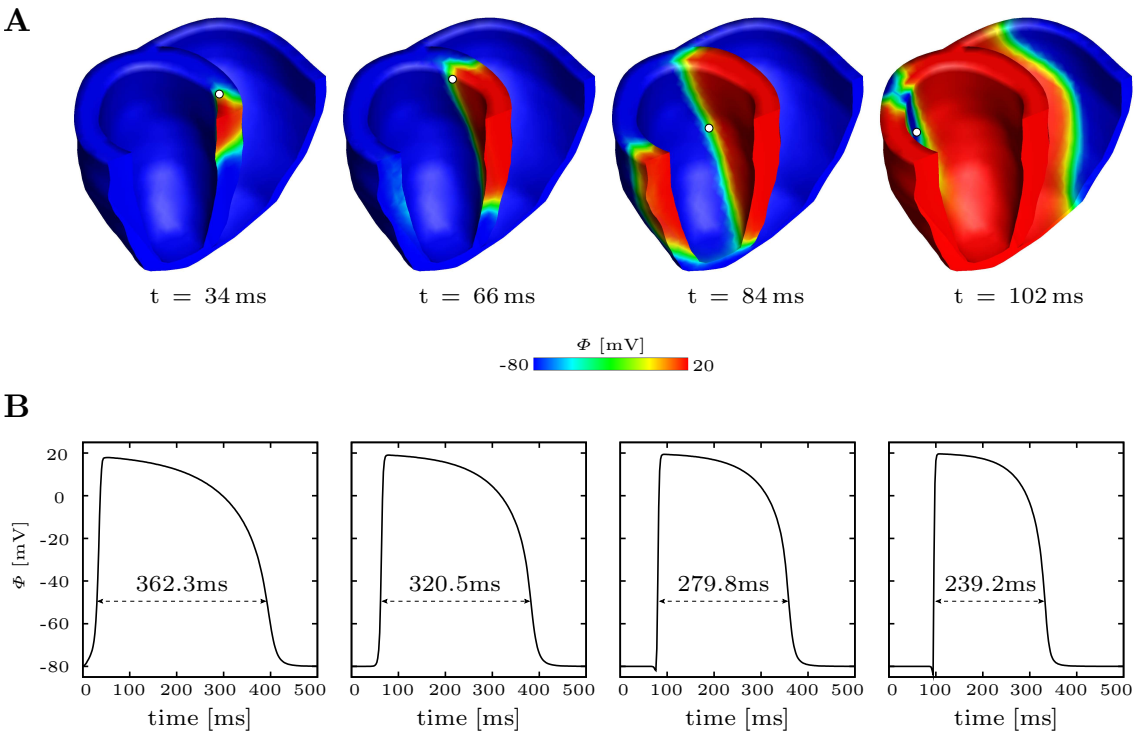

Figure 4.8: **A**: The cross section of the biventricular heart model depicting the transmembrane potential Φ at various time.One of the cells to which the wave front reach at each time is marked. At the marked cells, APs are implemented to compare. **B**: The corresponding APs are obtained from each node marked in **A**, which shows that the cell depolarized later has the longer APD.

relatively earlier than other cells. Each AP obtained at the cells marked with white dot in Figure 4.8**A** is plotted in Figure 4.8**B**, which shows that the earlier the cell depolarize, the longer APD the cell has. For example, the wave front reaches to the the cell located nearby the AV node at time $t = 34\,\text{ms}$, where the APD70 is 362.3 ms. The cell to which the wave front reaches at $t = 102\,\text{ms}$ has the shorter APD70 (239.2 ms).

With this feature, the regular cardiac cycles with MEF effect in terms of λ_f, $\dot{\lambda}_\text{f}$ and λ_s are simulated and the corresponding ECGs are recorded as shown in Figure 4.10. The different G_s were applied to the viscoelastic simulations and the elastic simulations, respectively. Note that the plotted ECGs are obtained after several cycles, so the electromechanical state of the material points is almost same with the previous cycle. The difference in QRS complexes are imperceptible in all 3 MEF cases, while ST segment differs in each ECG. ST segment in ECG corresponds to the plateau phase of AP in which no current flow through transmembrane. Therefore, ST segment is isoelectric ($\Phi = 0\,\text{mV}$) in normal healthy heart beat. The ECGs regarding $\hat{f}^{\phi}_{\lambda_\text{f}}$ and $\hat{f}^{\phi}_{\lambda_\text{s}}$ show non-isoelectric ST segment while $\hat{f}^{\phi}_{\dot{\lambda}_\text{f}}$ shows relatively isoelectric ST segment. The ECG recorded by the elastic formulation has bigger amount of deviation of the ST segment than the ECG by viscoelastic formulation despite the equivalent amount of G_s. For example, the speedier repolarization is observed, which decreases the risk of an irregular heartbeat such as long QT-syndrome [53]. The relatively shortend AP plateau and the steeper gradient of repolarization in AP causes this phenomenon (See Figure 4.3). This influence of MEF is consistent with the results of studies that include [8, 43, 54]. Figure 4.10**B** shows how the MEF in terms of $\dot{\lambda}_\text{f}$ is influencial on the ECG of the heart during normal cardiac cycle. As G_s increases, the T

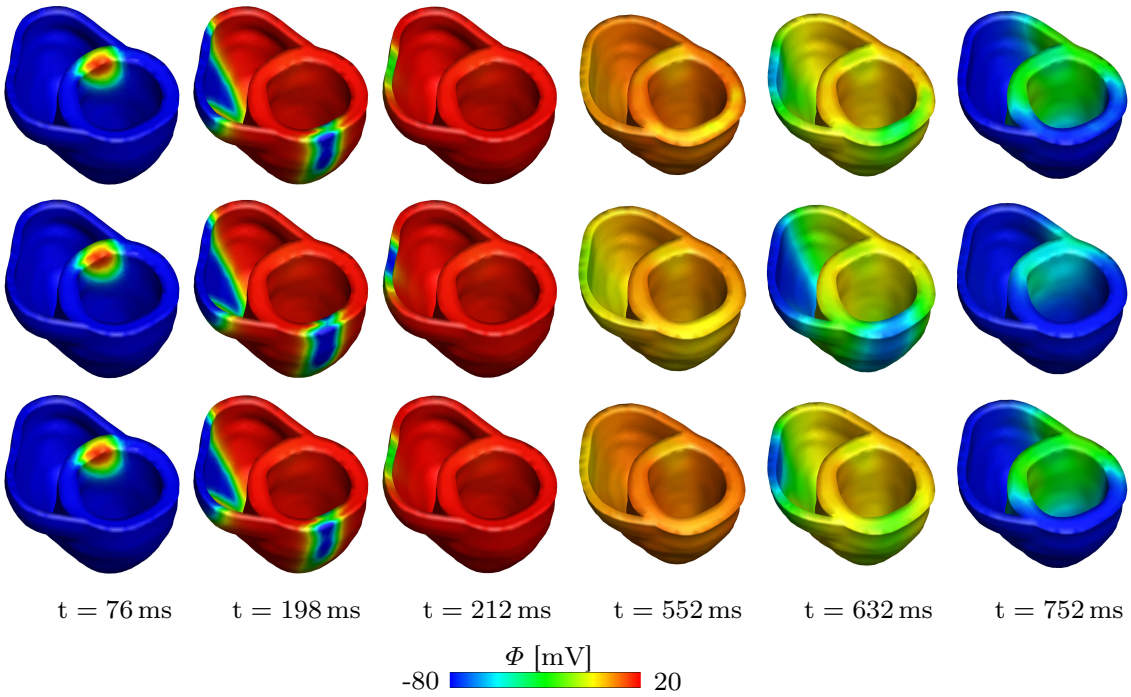

Figure 4.9: Illustration of the transmembrane potential distribution under MEF considering $\hat{f}^{\phi}_{\lambda_{\mathrm{f}}}$ (first row), $\hat{f}^{\phi}_{\dot{\lambda}_{\mathrm{f}}}$ (second row) and $\hat{f}^{\phi}_{\lambda_{\mathrm{s}}}$ (third row) with viscoelastic formulation. 3 MEF cases affect the cardiac electrophysiology.

wave develops earlier, which is more clearly visible in case of elastic formulations. Also, it is discovered the ST segment is in isoelectric state. The set of ECGs in Figure 4.10**C**, in which MEF was reformulated in terms of λ_{s}, is sensitive to a small increase of G_s. These reformulations of MEF alter the tramsmembrane potential of the heart. Figure 4.9 shows the snapshots of the transmembrane potential contour obtained by applying MEF in terms of λ_{f}, $\dot{\lambda}_{\mathrm{f}}$ and λ_{s}. The difference is more clearly visible in the diastole.

Simulation of volume-time curve

The v-t curve exhibits the volume change of the left ventricle as a function of time during a single cardiac cycle. Although ECG is useful tools being capable of providing non-invasively continuous measurement of the electric activity of the heart, it is not capable of recording information about the actual blood volume passing through the heart. Electrophysiological data from ECG need to be combined with hemodynamic data for a more comprehensive evaluation of the cardiac function. Therefore, in this respect, deviations in the v-t curves may be useful in the screening and monitoring of patients with a cardiac disease [55]. Indeed, early detection and regular monitoring using the v-t curve, may prevent progression of disease [56, 57]. In this part, the regular cardiac cycles for elastic and viscoelastic cases are simulated with the varied G_s and each corresponding LV v-t curve is recorded as represented in Figure 4.10. The LV volume information was recorded simulataneously with the aforementioned simulations of the ECGs . Each surface element located in the endocardium of the LV forms triangular pyramid of which the height is the distance to a particular node to the basal surface. The volume integration of all the deformed triangular pyramid is recorded as the LV volume at each time. Initial LV volume is 109.54 ml. In the analyses ventricular pressure evolution is not taken into account. The

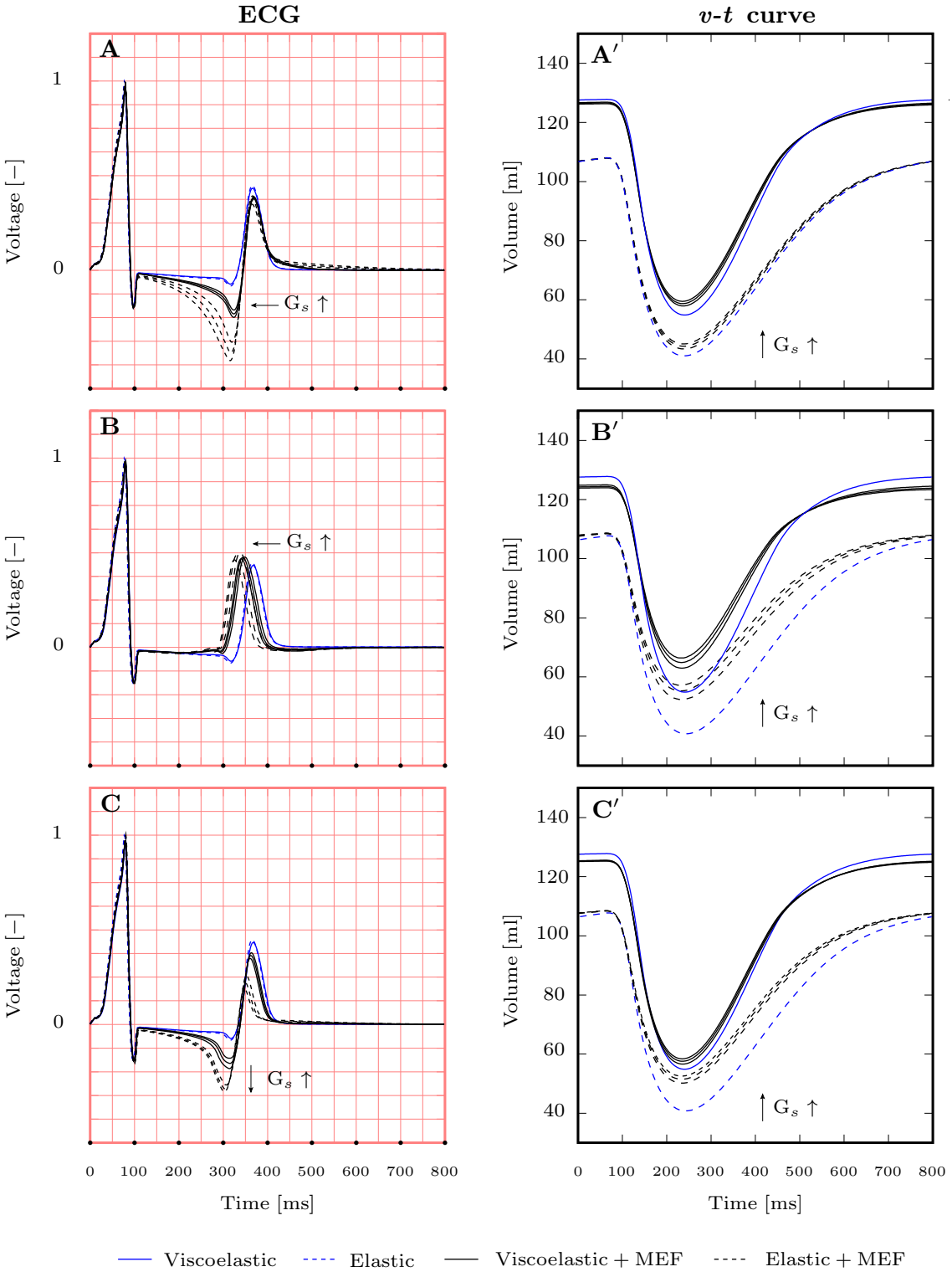

Figure 4.10: The ECGs and v-t curves recorded during normal cardiac cycle using the biventricular heart model where MEF applied with considering λ_{f}, $\dot{\lambda}_{\mathrm{f}}$ and λ_{s}. Top : **A** and **A′** are shown as results of MEF by λ_{f} ($G_s : 0, 40, 50, 60$). Middle : **B** and **B′** are shown as results of MEF by $\dot{\lambda}_{\mathrm{f}}$ ($G_s : 0, 10, 15, 20$). Bottom : **C** and **C′** are shown as results of MEF by λ_{f} ($G_s : 0, 0.06, 0.08, 0.10$). The dotted-black lines and the solid-black lines are recorded from the elastic and viscoelastic formulation with MEF, respectively. The ECGs obtained by the elastic and viscoealstic simulation where MEF is not considered are displayed with the dotted-blue lines and the solid-blue lines, respectively.

Cardiac	$\mathbf{A}'$ ($f^{\phi}_{\lambda_f}$)			$\mathbf{B}'$ ($f^{\phi}_{\dot{\lambda}_f}$)			$\mathbf{C}'$ ($f^{\phi}_{\lambda_s}$)		
output	G_s	SV [ml]	EF [%]	G_s	SV [ml]	EF [%]	G_s	SV [ml]	EF [%]
E_0	-	67.32	62.44	-	67.30	62.43	-	67.30	62.43
E_1	40	64.55	59.80	10	55.83	51.49	0.08	58.21	53.71
E_2	50	63.64	58.93	15	53.12	48.93	0.10	56.94	52.51
E_3	60	62.87	58.19	20	51.43	47.34	0.12	55.94	51.55
VE_0	-	73.37	57.32	-	73.45	57.36	-	73.09	57.20
VE_1	40	73.29	57.35	10	61.76	49.43	0.08	68.55	54.20
VE_2	50	73.28	57.35	15	59.50	47.80	0.10	67.50	53.48
VE_3	60	73.28	57.34	20	57.47	46.37	0.12	66.37	52.71

Table 4.3: G_s, SV and EF values of the v-t curves in Figure 4.10 ($\mathbf{A}', \mathbf{B}'$ and $\mathbf{C}'$) are shown for elastic (E) and viscoelastic (VE) cases. The subscripts 0 indicate the blue curves ($G_s = 0$). The subscripts 1, 2 and 3 indicate black curves obtained with MEF application, which have the different G_s values from smallest to largest. The cardiac outputs are obtained during the normal cycles with the different MEF formulation in terms of $f^{\phi}_{\lambda_f}$, $f^{\phi}_{\dot{\lambda}_f}$ and $f^{\phi}_{\lambda_s}$.

simulation results reveal conspicuous distinctions between the elastic and viscoelastic formulations with different G_s. After the subsequent cycles the initial LV volumes saturated to different values for elastic and viscoelastic cases. Residual stretches induce bigger EDV in viscoelastic cases due to viscous effects. Ascending limb of the curves in elastic case is flatter which might cause abnormal filling characteristics [58]. The higher G_s causes less EDV which sequentially causes less SV values. Also, the higher G_s induces less contraction so that higher ESV occurs which causes less SV leading to less EF. However, the elastic curve is more like shifted upwards with a slight increase in EDV and a big increase in ESV. The biggest deviation in ESV is observed in $\mathbf{B}'$ where $\hat{f}^{\phi}_{\dot{\lambda}_f}$. In all types of MEF simulation, the amount of blood pumped by LV (SV) is reduced.

4.2.2 Commotio cordis

Arrhythmias such as the tachycardia and fibrillation tend to be generated in the heart that suffers an acute myocardial infarction or ischaemia [59], but the VF is one of the most critical arrhythmias which causes the uncoordinated heart beats and this rhythm is reponsible for the sudden cardiac death (SCD).

Secondly, it is investigated how MEF plays a role in intact heart under pathological disturbance, *Commotio cordis* (Latin: 'disturbance of heart'). Commotio cordis is an uncommon but fatal mechano-electric syndrom, being increasingly reported world wide as a well documented cause of death, most commonly in young males who are involved in sporting activities [16]. The phenomenon is defined as mechanical stimulation of the heart by non-penetrating, impulse-like impact to the precordium that, through intrinsic cardiac mechanisms, gives rise to disturbances of cardiac rhythm of varying type, duration, and severity, including sudden cardiac death, in the absence of structural damage [17]. The MEF is thought to be responsible for Commotio cordis, a condition in which the precordial impact of an object may trigger ventricular fibrillation (VF) [7, 35, 19, 16, 60, 61, 62, 63]. In the section, VF is simulated by moderate impact on the intact heart. Afterward, it is also simulated that the obtained VF is reverted by a chest thump. To do so, we first simulate two regular heart beats. Then, during the vulnerable phase of cardiac repolarization in $3rd$ cycle, the impact is applied on the LV region to trigger ectopic excitation

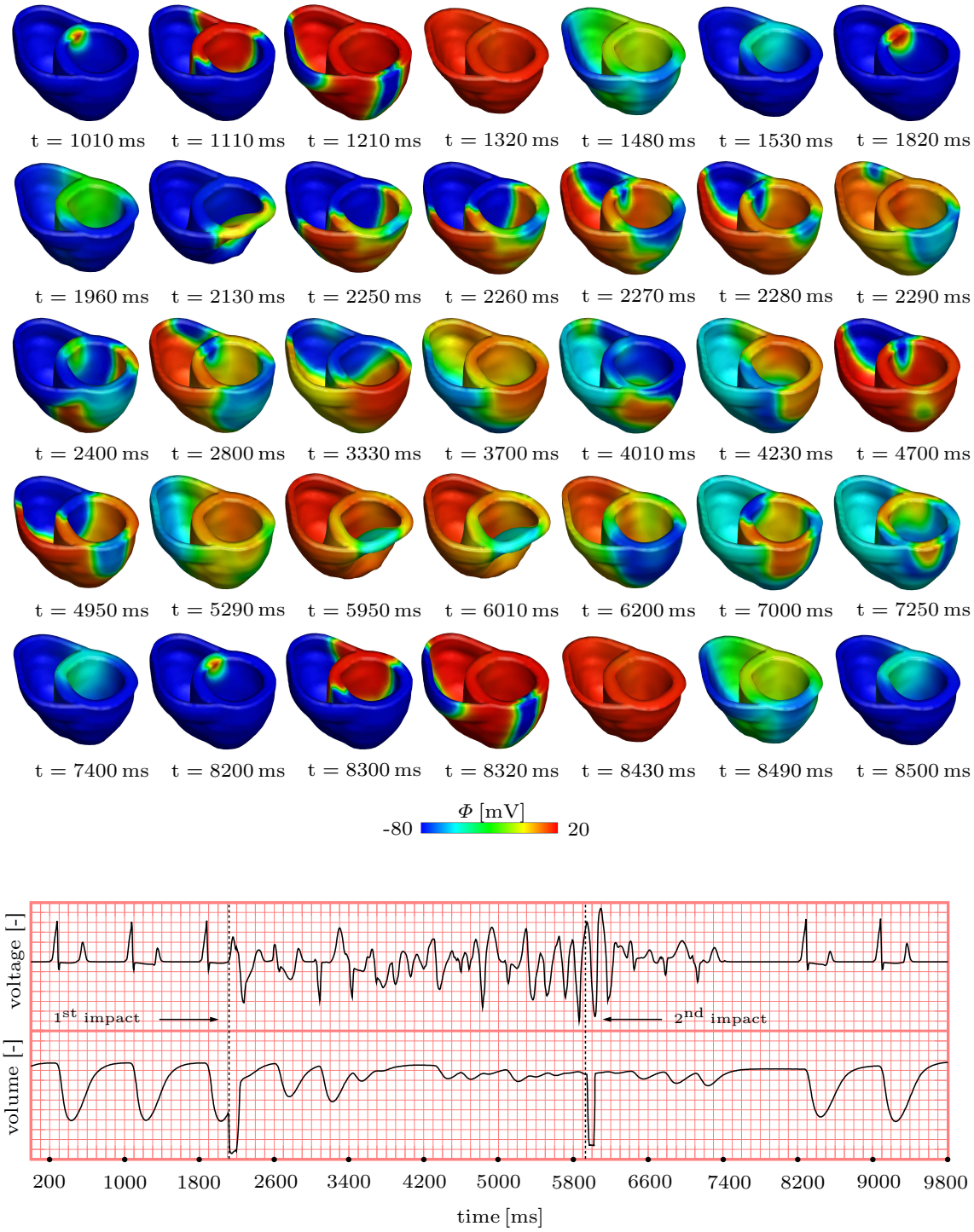

Figure 4.11: Simulation of VF by commotio cordis and its termination by precordial thump. After normal thw cycles, a mechanical impact is externally applied on the precordial region at $t = 2110$ms which cause re-entrant wave on the heart for subsequent 4 cycles. Simulataneously, ECG and v-t curve are recorded. During fibrillation, the heart does not function properly as it is fluttering. ECG is fluctuating abnormally and EF value dips as low as almost zero. Precordial thump applied to terminate the arrhythmia at $t = 5910$ms. The heart returns to the resting state and starts normal sinus beat again.

that may lead to VF. For the spring stiffness for the constrained state of the ventricle, respectively, $k_{\mathrm{x}} = k_{\mathrm{y}} = k_{\mathrm{z}} = 2 \cdot 10^{-3}\,\mathrm{N/mm^2}$ at the nodes basal surface $z = 0$, and $k_{\mathrm{x}} = k_{\mathrm{y}} = k_{\mathrm{z}} = 2 \cdot 10^{-4}\,\mathrm{N/mm^2}$ at the epicardium are used. Pressure evolution is not considered. For the SACs, $(f^{\phi}_{\lambda_{\mathrm{f}}})$ in Equation (3.65) is considered.

The snapshots of the numerical analysis are represented in Figure 4.11 along with the corresponding ECG and v-t curve. In the 3^{rd} cycle, the impact on the LV is applied at time 2110 ms around ventricular repolarization for 70 ms. As the region at which the impact applied deforms, the cardiac cells start to be excited through the electrical source term Equation (3.65). The excitation leads to depolarization of the heart from the basal surface where stiffer springs are attached. Consequently re-entrant waves and arrhythmia are generated. Hence, the oscillation pattern of ECG from this time on becomes highly fluctuating and unpredictable. Also it is found that the EF value drops to zero as the heart starts to flutter instead of contracting, therefore the heart becomes incapable of pumping proper stroke volume. Afterwards, the termination of ventricular fibrillation "Precordial thump" [64] is simulated by applying a mechanical force. The effectiveness of termination of arrhythmia varies, depending on the character of arrhythmia [15]. In comparison to the effective treatment of ventricular arrhythmias by controlled mechanical stimulation, the reports on successful reversal of ventricular fibrillation by chest thump are relatively rare. Still, mechanical stimulation of precordial regions of the chest has the potential to reinstate normal heart beat. Precordial thump is a simple and readily available means for the termination of arrhythmia [15, 64]. The mechanical stimulation is applied at time $t = 5910$ ms for 80 ms and interrupts the re-entry, by which the arrhythmia is terminated and the heart moves on to the resting state. Later, the function of heart is fully reverted by the depolarization of ventricle. ECGs and v-t curves show the normal behavior of the heart.

4.3 MEF with LV heart model

4.3.1 Hemodynamically-induced disturbance of heart rhythm

In the previous section, the intact heart was disturbed by the mechanical loading. In this section, it is illustrated how the heart behaves when the acutely altered hemodynamic loading applied. To do so, two simulations are performed and compared: one in which the sudden increase of preload takes place and the other without preload variation. Here, the blood pressure evolution is incorporated to the finite element formulation developed in Chapter 3 using the surface elements responsible for imitating the existence of blood as pressure load applying the inner ventricular boundaries, which enables to achieve information of the intraventricular pressure. The used geometry for the simulation is shown in Figure 4.12, which is discretized by 11737 tetrahedral elements over 2632 nodes as well as 894 triangular surface elements. Fiber angle is calculated by the linear interpolation as explained in Equation (4.1). Myocardiac tissue is electrically in a resting state $\Phi_0 = $ -80 mV at time $t = 0$ ms. The parameters are taken from Table 4.1 except for $\xi = 0.103\,[-]$, $b = 0.15\,[-]$, $\mu_1 = 0.12\,[-]$, $G_s = 5.0\,[-]$, $d_{\mathrm{iso}} = 0.15\,\mathrm{mm^2/ms}$ and $d_{\mathrm{ani}} = 15.0\,\mathrm{mm^2/ms}$. Before applying a transient hemodynamic disturbance, it is required to obtain the heart where the electromechanical state of the material points is almost the same with the previous cycle. To do this, the values in transmembrane potential field first are saturated with all nodes constrained where the pressure evolution is not implemented. Then, the deformation field is saturated until $\lambda'_{\boldsymbol{f}}$ in Equation (4.2) is obtained with the pressure loading. After-

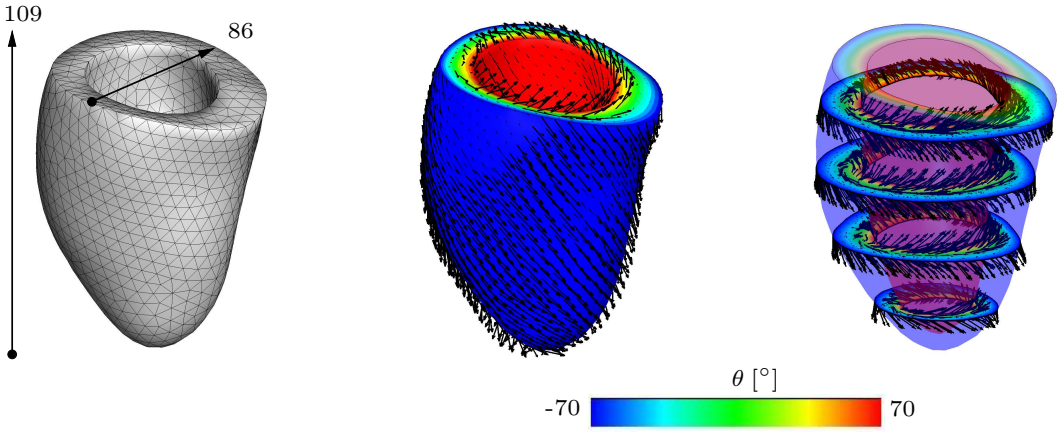

Figure 4.12: The virtual left ventricular model of a healthy person. A 38 years old healthy volunteer's (male) left ventricle was virtualized. Fiber angle at epicardial surface is set to $-70°$. Endocardial surface's fiber angle is $70°$. The fiber angle values between epicardium and endocardium are interpolated by Equation (4.1). All lengths are in millimetres.

wards, the normal cardiac cycles are additionally simulated with G_s to stabilize the heart with MEF effect. Excitations (I = 10 [−]) at AV node are generated every 800 ms. The constrained state of the LV is imitated by the attached springs at the nodes at basal and epicardial surface having stiffness values, respectively $k_x = k_y = k_z = 3 \cdot 10^{-3}\text{N/mm}^2$ at the nodes basal surface $z = 0\,\text{mm}$ and $k_x = k_y = k_z = 10^{-4}\text{N/mm}^2$. A constant time step $\Delta t = 2\,\text{ms}$ is used during the simulation. The scaling factor β_t is calculated as Equation (4.3). This stabilized LV with $p_1 = 10\,\text{mmHg}$ is hemodynamically disturbed by applying $p_1 = 15\,\text{mmHg}$ for 5 cycles. The cardiac outputs obatined during the cardiac cycles are displayed in Table 4.4 and Figure 4.13. In Figure 4.14, the PV loops recorded during both the cardiac cycle with and without the preload disturbance are shown. Figure 4.15**A** shows the pressure-time curve, v-t curve and ECG which are obtained during the simulation. In each graph, the solid lines are for the LV simulation with acute disturbance of preload and the dashed-lines represent the simulation without any disturbance. Until the first cycle, preload 10 mmHg is maintained thereby the PV loops are the same in Figure 4.14. From the 2^{nd} cycle the preload 10 mmHg is suddenly increased to 15 mmHg. The change of preload starts to take effect when the cardiac phase is moving on to the 4^{th} phase (filling) from 3^{rd} phase (isovolumetric relaxation) because of the varied switch value

Cardiac outputs	1st cycle	2nd cycle	3rd cycle	4th cycle	5th cycle	6th cycle
SV [ml]	140.596	143.398	61.413	163.577	3.167	170.228
EF [%]	55.194	55.275	24.811	62.285	1.334	65.207
EDV [ml]	254.732	259.425	247.527	262.625	237.469	261.057
ESV [ml]	114.136	116.027	186.114	99.049	234.301	90.829
EDP [mmHg]	31.637	37.004	23.976	41.315	15.368	39.533
ESP [mmHg]	123.137	124.126	97.376	127.535	79.801	125.575
Phases of cardiac cycle [ms]						
Iso.Contraction	124	68	72	76	78	118
Ejection	92	92	88	90	78	88
Iso.Relaxation	118	114	136	106	264	102
Filling	522	524	500	530	338	482

Table 4.4: Cardiac indices from the LV simulation

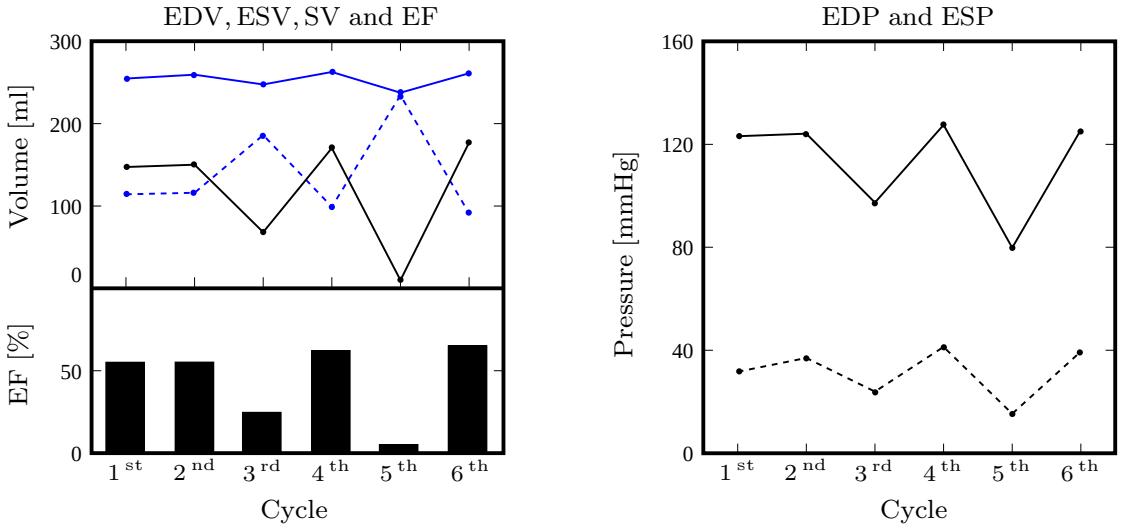

Figure 4.13: Left: Volume-related cardiac outputs (EDV, ESV, SV and EF) obtained in each cycle. The blue-solid and blue-dashed lines represent EDV and ESV, respectively. SV is depicted by the black-solid line. In the 3^{rd} and 5^{th} cycles, the decreased EFs are observed due to the hemodynamical disturbance. These reduction of EFs are mainly due to the less contraction and the increased ESV because there was no large EDV change. In the 4^{th} and 6^{th} cycles, the increased EF values are observed. Right: Pressure-related cardiac outputs (ESP and EDP). The black-solid and black-dashed lines represent EDP and ESP, respectively. It is shown that these two graphs are in inverse proportion to ESV.

in Figure 3.2 which imitates the increased atrial pressure. Also, the varied switch value lets the heart move on the filling phase earlier with the reduced isovolumetric relaxation duration as well as the higher EDV. It is observed that the LV is filled with the blood under high pressure (see the filling phase in 2^{nd} cycle of Figure 4.14). As a result, the LV undergoes significantly increased diastolic stretch during filling in its 2^{nd} cycle, which simultaneously causes MEF effect. The additionally caused current due to MEF interrupts the depolarization wave of the subsequent cycle. The MEF due to diastolic stretch has greater effect in 2^{nd}, 4^{th} and 6^{th}, which influences the next cycles (3^{rd} and 5^{th}) as shown in Figure 4.15**B**. As a result it is observed the less EF and the inverted T wave. In 3^{rd} cycle, it is found that the steeper gradient of ascending limb of QRS curve, the inverted T wave, less ESP, less EF (28.25%) as well as the smaller area within PV loops in Figure 4.14 which means the less ventricular stroke work. The reduced EF is mainly attributed to the increased ESV. In light of the fact that healthy human being's EF is normally more than 50%, the heart is not pumping properly. Also the reduced EDV is obtained, which causes less MEF effect on the LV. The less MEF due to less EDV cause the graphs of cardiac function in the 4^{th} to return to the normal. Also, EF recovers the normal range as well by contracting more (EF=59.98%). As the volume of LV increases in the end of the filling phase, which produces increased stretch, MEF effect increases enough to disturb the subsequent cycle again. Hence, this normal pumping alternates with improper pumping, which is similar to Bigeminy. Bigeminy is a heart rhythm problem which has a continuous alternation of normal and ectopic heart beats [65]. Ectopic beat is a disturbance of the cardiac rhythm frequently related to the electrical conduction. An ectopic beat can be further classified as either a premature ventricular contraction, or a premature atrial contraction. Postextrasystolic potentiation (PESP), the increase in contractility that follows an ectopic beat is also observed. Each ectopic beat has less EF which is compensated in the subsequent beat where EF is higher as shown in Table 4.4.

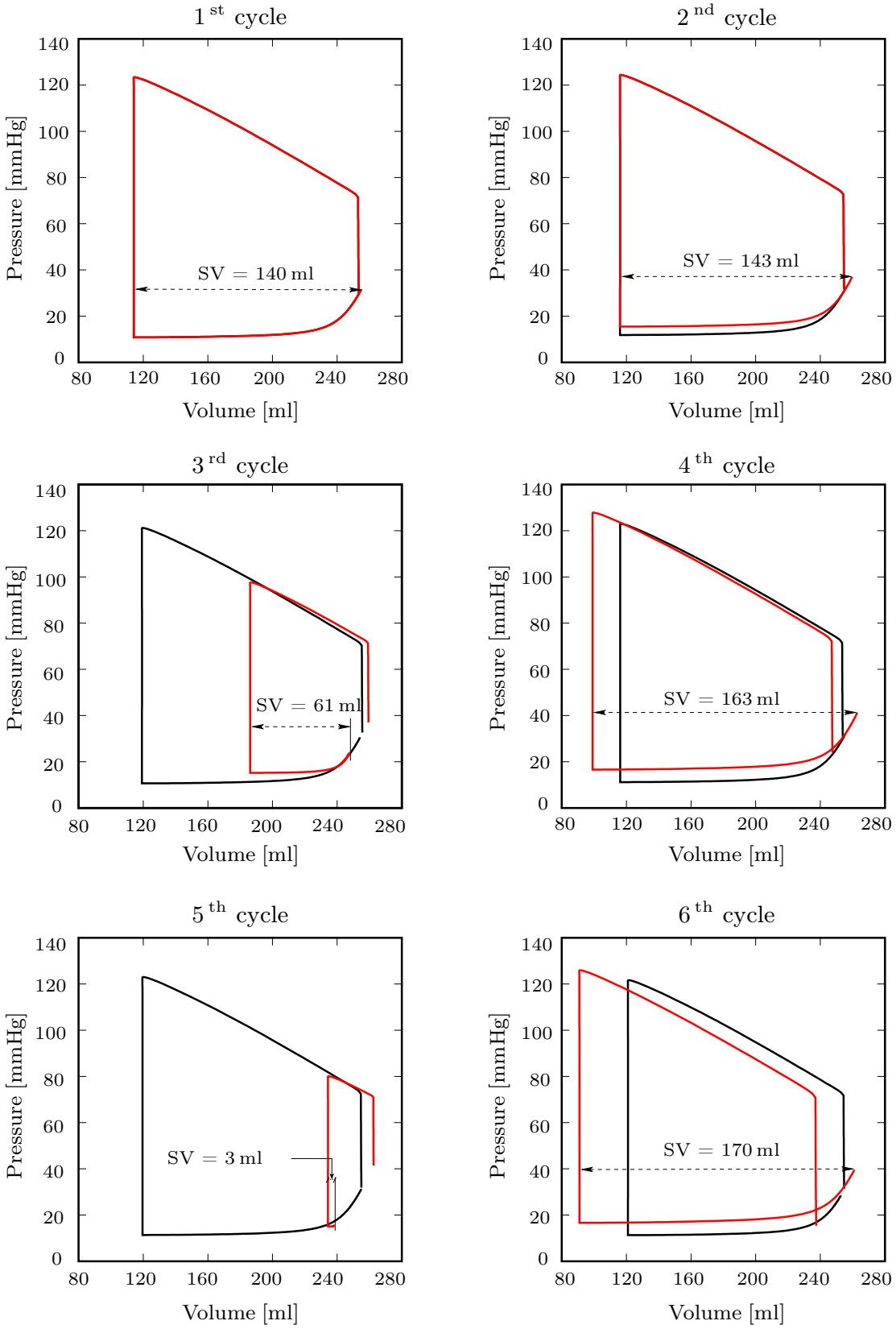

Figure 4.14: PV loops obtained in each cycle. The red curve represents the simulation with the acute preload increase. The black curves are obtained by the simulation without the variation of preload. In the 2^{nd}, $4^{th}$and 6^{th} cycle, the increased SV and EDV are observed. In the 3^{rd} and 5^{th} cycle, it is shown that decreased SV and the smaller area within PV loops which means the less ventricular stroke work.

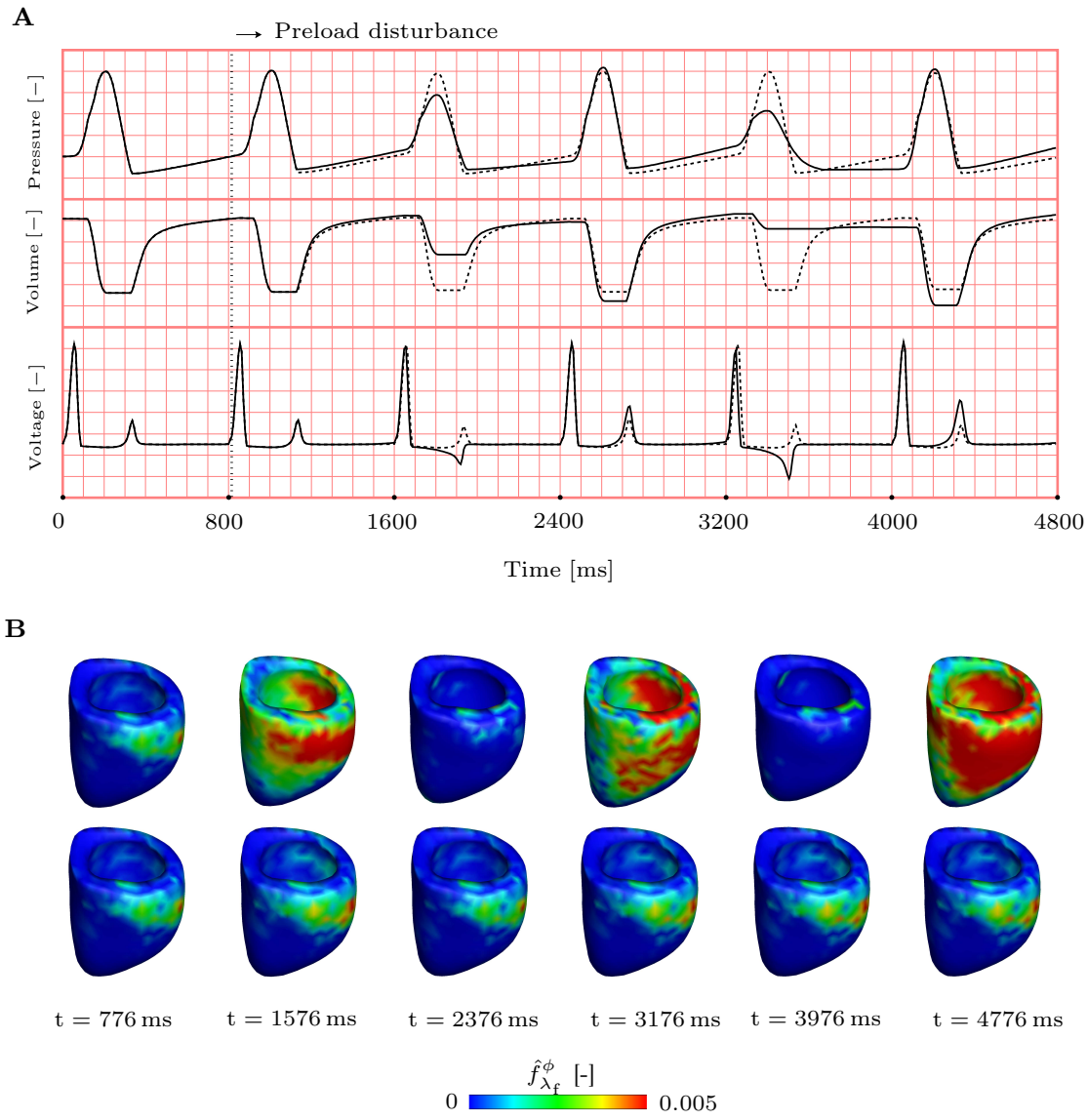

Figure 4.15: **A**: Pressure-time curve, v-t curve and ECG recorded during the cardiac cycles. The solid lines represent the simulation of LV with the sudden increase of preload (10 mmHg → 15 mmHg). The dashed lines represent the normal sinus beat without the variation of preload. In the 3^{rd} and 5^{th} cycles, the inverted T-wave, the reduced ESP and the reduced ESV are clearly observed. In 4^{th} and 6^{th} cycles, the LV contract more strongly than the contraction in normal situation, which imitates PESP. **B**: the contour of MEF ($\hat{f}^{\phi}_{\lambda_f}$) at a certain time during diastole phase in each cycle. Top row represents the contours obtained from the simulation where the sudden increase of preload applied. The MEF contour snapshots in the bottom row are obtained without the application of the acute preload variation. Higher EDV in 2^{nd}, 4^{th} and 6^{th} cycle due to the higher preload lengthen the stretch in the myocardium, which creates the additional current through MEF ($\hat{f}^{\phi}_{\lambda_f}$), see the contour at time 1576 ms, 3176 ms and 4776 ms. These effects cause the less contraction and the less relaxation at each subsequent cycle. The less relaxation does not turn MEF on strongly, which recover the pumping of the heart in 3^{rd} and 5^{th} cycles with the increased EF. This phenomenon mimics PESP.

5 Conclusion

The thesis investigated MEF using the numerical tools for electromechanical coupling in the myocardial tissue in monodomain setting. On material level a modified Hill model was adopted to take the orthotropic electro-visco-elastic response of the cardiomyocytes, where the rheology is decomposed into both electrical deformation and visco-elastic deformation in a multiplicative way. The incorporation of stretch-induced currents (SACs) enables the FEM model to have a two way coupling; excitation-induced contraction and deformation-induced generation of excitation. Several numerical experiments were performed via above-mentioned numerical tools.

In the numerical experiments with the cardiac tissue bar, it was found that MEF quite can reduce the time to activate whole tissue. As soon as the regional stretch by the depolarization was developed, the cells placed in remote region were brought under tension. If MEF is considered, the magnitude of the current due to SACs was enough to depolarize the remote cell so that the dispersion of electrical activity in the tissue bar decreases. Also the influence of MEF varied depending on the material types with which the experiments were performed. While the tissue bar with the elastic material immediately responds to mechanical contraction, the bar with the viscoelastic material has certain time gap between the contraction and active force, which varied the electrophysiology of cardiac cells in the simulation. Furthermore, the reason of the different electrophysiology might be due to the fact that λ_f in f_m^{ϕ} was altered when the viscoelastic formulation is considered. Also, the viscoelasticity affected the conductivity tensor $\boldsymbol{D}$ through the term $\boldsymbol{f} \otimes \boldsymbol{f}$. In turn, $\boldsymbol{D}$ subsequentially altered the deformation domain in comparison with the elastic cases. It seems that viscoelasticity altered the two way coupling reciprocally.

With the biventricular model, two different mathematical models for SACs were suggested and compared with the original SACs model. While the original is computed in terms of the λ_f, the suggested models consider $\dot{\lambda}_\mathrm{f}$ and λ_s instead of the λ_f. They were suggested based on the fact that the region in which λ_f was positive and the areas where $\dot{\lambda}_\mathrm{f}$ and λ_s had positive value were not identical in the biventricular heart model. Moreover, there are a lot of studies showing that MEF affected not only by the stretch itself but also the velocity at which the stretch is applied. The suggested SACs model indicated that the electrophysiological behavior of the heart was also different than that of the original. The SACs model regarding λ_f mostly turned on at diastole especially in the right ventricle. In contrast, SACs in terms of $\dot{\lambda}_\mathrm{f}$ affected mostly the basal surface region. Immediately after the initiation of excitation, $\dot{\lambda}_\mathrm{f}$ at the basal region started to generate MEF, which does not occur in the case of λ_f. Also, the MEF regarding λ_s has shown that the MEF affects the different of region. Only normal healthy heart model was used to carry out the simulations, but if some regions of the heart are not healthy, such as a regional myocardial infarction, MEF may affect critically the cardiac electophysiology in heart. Probably it is worth to suggest a new SACs model where λ_f, $\dot{\lambda}_\mathrm{f}$ and λ_s are considered together. Furthermore, in the thesis, in order to make it easier to explore the MEF effect, the values for G_s which determines the magnitude of MEF were set differently and arbitrarily so these G_s could be too much greater than the realistic value. As the value increases, the T wave representing the ventricular repolarization became more inverted shape. So in order to use MEF clinically G_s must be decided in advance.

VF due to a moderate impact on the normal healthy heart also simulated with the biventricular heart model. To create self-sustained scroll wave a mechanical impact was applied on the left ventricular region. One of the important factor for the re-entry wave is the timing of force generating the stretch. If the stretch is applied when the myocardium is in depolarized state, it is not possible to create re-entry. In the simulations, the area at which the force was applied was too wide and the magnitude of force were unnecessarily too big. It could have been possible to achieve VF with the smaller force with narrower area.

The pressure-volume relationship is explored with LV model. In the simulations, the surface element formulation to imitate the blood pressure evolution was incorporated during the normal cardiac cycles. By increasing suddenly the preload it was possible to achieve the result similar to the premature ventricular contraction. The ectopic beat and the normal sinus beat are repeated every two cycle. Postextrasystolic potentiation (PESP) is also observed in the result, that is, the reduced SV in the ectopic beats is compensated by the increased SV in the subsequent the normal beats.

5.1 Limitations and outlook

- MEF mainly induces the speedier time of repolarization which will increase the heart beat rate. Also, some studies [15, 66, 67, 68] report MEF is capable of regulating the heart beat rate. However, in this work, the rate is constant because the excitation at AV node is set to generate every 800 ms.
- In Section 4.3.1, MEF generates additional currents out of the AV node. If the Purkinje fiber was considered, the current generated by MEF could pass through the fiber, so it might have been possible to obtain more realistic results.
- In Section 4.3.1, the LV is filled with the higher blood pressure, which causes not only the greater fiber lengthening but also the rapider lengthening. The consideration of MEF in terms of $\dot{\lambda}_\mathrm{f}$ could affect the cardiac electrophysiology.
- Stretching of cardiac cells or tissues implies an increase in the diastolic free Ca^{2+} concentration [69], which increases the contractility of the heart. In section 4.1, the peak value of calcium concentration was lower in the simulation with MEF. Also Section 4.2.1 shows that as G_s increases, ESV is increased.
- The suggested reformulations of SACs in section 3.6 consider $\dot{\lambda}_\mathrm{f}$ and λ_s individually. The SACs may includes λ_f, $\dot{\lambda}_\mathrm{f}$ and λ_s in order to experss more realistic MEF effect on normal heart with the help of further experiments.
- Springs attached to LV epicardium should have different stiffness due to the different surroundings.

Bibliography

[1] Cansiz, B.; Dal, H.; Kaliske, M.: "Computational cardiology: A modified Hill model to describe the electro-visco-elasticity of the myocardium". *Computer Methods in Applied Mechanics and Engineering* 315 (2017), pp. 434–466.

[2] Cansiz, B.; Dal, H.; Kaliske, M.: "Computational cardiology: the bidomain based modified Hill model incorporating viscous effects for cardiac defibrillation". *Computational Mechanics* (2017), pp. 1–19.

[3] Markhasin, V. S.; Solovyova, O.; Katsnelson, L. B., et al.: "Mechano-electric interactions in heterogeneous myocardium: Development of fundamental experimental and theoretical models". In: *Progress in Biophysics and Molecular Biology*. Vol. 82. 1-3. 2003, pp. 207–220.

[4] Riemer, T. L.; Sobie, E. A.; Tung, L.: "Stretch-induced changes in arrhythmogenesis and excitability in experimentally based heart cell models." *The American journal of physiology* 275.2 Pt 2 (1998), H431–42.

[5] Eckardt, L.; Kirchhof, P.; Mönnig, G., et al.: "Modification of Stretch-Induced Shortening of Repolarization by Streptomycin in the Isolated Rabbit Heart". *Journal of cardiovascular pharmacology* 36 (2001), pp. 711–721.

[6] Reiter, M. J.; Synhorst, D. P.; Mann, D. E.: "Electrophysiological effects of acute ventricular dilatation in the isolated rabbit heart". *Circulation Research* 62.3 (1988), pp. 554–562.

[7] Pfeiffer, E. R.; Tangney, J. R.; Omens, J. H., et al.: "Biomechanics of Cardiac Electromechanical Coupling and Mechanoelectric Feedback". *Journal of Biomechanical Engineering* 136.2 (2014), p. 021007.

[8] Lab, M. J.: "Mechanoelectric feedback (transduction) in heart: Concepts and implications". *Cardiovascular Research* 32.1 (1996), pp. 3–14.

[9] Lab, M. J.: "Mechanosensitivity as an integrative system in heart: An audit". *Progress in Biophysics and Molecular Biology* 71.1 (1999), pp. 7–27.

[10] Benjamin, E. J.; Virani, S. S.; Callaway, C. W., et al.: "Heart Disease and Stroke Statistics—2018 Update: A Report From the American Heart Association". *Circulation* 137.12 (2018), e67–e492.

[11] Bers, D. M.; Despa, S.: "Cardiac Excitation-Contraction Coupling". *Encyclopedia of Biological Chemistry: Second Edition* (2013), pp. 379–383.

[12] Quinn, T. A.; Kohl, P.: "Rabbit models of cardiac mechano-electric and mechanomechanical coupling". *Progress in Biophysics and Molecular Biology* 121.2 (2016), pp. 110–122.

[13] Lerman, B. B.; Burkhoff, D.; Yue, D. T., et al.: "Mechanoelectrical feedback: Independent role of preload and contractility in modulation of canine ventricular excitability". *Journal of Clinical Investigation* 76.5 (1985), pp. 1843–1850.

[14] Franz, M. R.; Burkhoff, D.; Yue, D. T., et al.: "Mechanically induced action potential changes and arrhythmia in isolated and in situ canine hearts". *Cardiovascular Research* 23.3 (1989), pp. 213–223.

[15] Kohl, P.; Hunter, P.; Noble, D.: "Stretch-induced changes in heart rate and rhythm: Clinical observations, experiments and mathematical models". *Progress in Biophysics and Molecular Biology* 71.1 (1999), pp. 91–138.

[16] Menezes, R. G.; Fatima, H.; Hussain, S. A., et al.: "Commotio cordis: A review." *Medicine, science, and the law* 57 3.3 (2017), pp. 146–151.

[17] Nesbitt, A. D.; Cooper, P. J.; Kohl, P.: "Rediscovering commotio cordis". *Lancet* 357.9263 (2001), pp. 1195–1197.

[18] Orini, M.; Nanda, A.; Yates, M., et al.: "Mechano-electrical feedback in the clinical setting: Current perspectives". *Progress in Biophysics and Molecular Biology* 130 (2017), pp. 365–375.

[19] Kohl, P.; Nesbitt, A. D.; Cooper, P. J., et al.: "Sudden cardiac death by Commotio cordis : role of mechano – electric feedback". *New England Journal of Medicine* 50 (2001), pp. 280–289.

[20] Link, M. S.; Wang, P. J.; Pandian, N. G., et al.: "An Experimental Model of Sudden Death Due to Low-Energy Chest-Wall Impact (Commotio Cordis)". *New England Journal of Medicine* 338.25 (1998), pp. 1805–1811.

[21] Lee, L. C.; Genet, M.; Dang, A. B., et al.: "Applications of computational modeling in cardiac surgery". *Journal of Cardiac Surgery* 29.3 (2014), pp. 293–302.

[22] Keldermann, R. H.; Nash, M. P.; Panfilov, A. V.: "Pacemakers in a Reaction-Diffusion Mechanics System". *Journal of Statistical Physics* 128 (2007), pp. 375–392.

[23] Panfilov, A. V.; Keldermann, R. H.; Nash, M. P.: "Self-organized pacemakers in a coupled reaction-diffusion-mechanics system". *Physical Review Letters* 95.25 (2005).

[24] Zienkiewicz, O.; Taylor, R.: *The finite element method: solid mechanics*. 2nd ed. Butterworth-heinemann, 2000.

[25] Cherubini, C.; Filippi, S.; Nardinocchi, P., et al.: "An electromechanical model of cardiac tissue: Constitutive issues and electrophysiological effects". *Progress in Biophysics and Molecular Biology* 97.2-3 (2008), pp. 562–573.

[26] Sansour, C.: "On the spatial description in elasticity and the Doyle-Ericksen formula". *Computer Methods in Applied Mechanics and Engineering* 107.1-2 (1993), pp. 239–249.

[27] Holzapfel, G. A.; Ogden, R. W.: "Constitutive modelling of passive myocardium: a structurally based framework for material characterization". *Philosophical Transactions of the Royal Society A: Mathematical, Physical and Engineering Sciences* 367.1902 (2009), pp. 3445–3475.

[28] Cansiz, F. B. C.; Dal, H.; Kaliske, M.: "An orthotropic viscoelastic material model for passive myocardium: theory and algorithmic treatment". *Computer Methods in Biomechanics and Biomedical Engineering* 18.11 (2015), pp. 1160–1172.

[29] Biot, M. a.: *Mechanics of Incremental Deformation*. Vol. 32. 4. 1965, p. 957.

[30] Ashikaga, H.; Coppola, B. A.; Hopenfeld, B., et al.: "Transmural Dispersion of Myofiber Mechanics. Implications for Electrical Heterogeneity In Vivo". *Journal of the American College of Cardiology* 49.8 (2007), pp. 909–916.

[31] Gurev, V.; Constantino, J.; Rice, J. J., et al.: "Distribution of electromechanical delay in the heart: Insights from a three-dimensional electromechanical model". *Biophysical Journal* 99.3 (2010), pp. 745–754.

[32] Aliev, R. R.; Panfilov, A. V.: "A Simple Two-variable Model of Cardiac Excitation". *Chaos, Solitons and Fractals* 7.3 (1996), pp. 293–301.

[33] Akay, M.; Craelius, W.: "Mechanoelectrical Feedback in Cardiac Myocytes from Stretch-Activated Ion Channels". *IEEE Transactions on Biomedical Engineering* 40.8 (1993), pp. 811–816.

[34] Quinn, T. A.: "Cardiac mechano-electric coupling: A role in regulating normal function of the heart?" *Cardiovascular Research* 108.1 (2015), pp. 1–3.

[35] Trayanova, N. A.; Rice, J. J.: "Cardiac electromechanical models: From cell to organ". *Frontiers in Physiology* 2 AUG (2011).

[36] Sachse, F. B.; Hunter, G. A. M.; Weiss, D. L., et al.: "A Framework for Modeling of Mechano-Electrical Feedback Mechanisms of Cardiac Myocytes and Tissues". *Engineering in Medicine and Biology Society, 2007. EMBS 2007. 29th Annual International Conference of the IEEE* (2007), pp. 160–163.

[37] Craelius, W.; Chen, V.; El-Sherif, N.: "Stretch activated ion channels in ventricular myocytes". *Bioscience Reports* 8.5 (1988), pp. 407–414.

[38] Kim, D.: "A mechanosensitive K+ channel in heart cells. Activation by arachidonic acid". *J. Gen. Physiol.* 100.6 (1992), pp. 1021–1040.

[39] Hu, H.; Sachs, F.: "Stretch-activated ion channels in the heart". *Journal of Molecular and Cellular Cardiology* 29.6 (1997), pp. 1511–1523.

[40] Franz, M. R.; Cima, R.; Wang, D., et al.: "Electrophysiological effects of myocardial stretch and mechanical determinants of stretch-activated arrhythmias [published erratum appears in Circulation 1992 Nov;86(5):1663]". *Circulation* 86.3 (1992), pp. 968–978.

[41] Lu, F.; Jun-Xian, C.; Rong-Sheng, X., et al.: "The effect of streptomycin on stretch-induced electrophysiological changes of isolated acute myocardial infarcted hearts in rats". *Europace* 9.8 (2007), pp. 578–584.

[42] Nishimura, S.; Kawai, Y.; Nakajima, T., et al.: "Membrane potential of rat ventricular myocytes responds to axial stretch in phase, amplitude and speed-dependent manners". *Cardiovascular Research* 72.3 (2006), pp. 403–411.

[43] Stacy, G. P.; Jobe, R. L.; Taylor, L. K., et al.: "Stretch-induced depolarizations as a trigger of arrhythmias in isolated canine left ventricles". *American Journal of Physiology - Heart and Circulatory Physiology* 263.2 (1992), H613–H621.

[44] Wall, S. T.; Guccione, J. M.; Ratcliffe, M. B., et al.: "Electromechanical feedback with reduced cellular connectivity alters electrical activity in an infarct injured left ventricle: a finite element model study". *AJP: Heart and Circulatory Physiology* 302.1 (2012), H206–H214.

[45] Burton, F. L.; Cobbe, S. M.: "Dispersion of ventricular repolarization and refractory period". *Cardiovascular Research* 50.1 (2001), pp. 10–23.

[46] Kamkin, A.; Kiseleva, I.: *Mechanosensitivity and Mechanotransduction*. 2011.

[47] Surawicz, B.: "Ventricular fibrillation and dispersion of repolarization." *Journal of cardiovascular electrophysiology* 8 (1997), pp. 1009–1012.

[48] Kuo, C. S.; Munakata, K.; Reddy, C. P., et al.: "Characteristics and possible mechanism of ventricular arrhythmia dependent on the dispersion of action potential durations." *Circulation* 67.6 (1983), pp. 1356–1367.

[49] Kotikanyadanam, M.; Göktepe, S.; Kuhl, E.: "Computational modeling of electrocardiograms: A finite element approach toward cardiac excitation". *International Journal for Numerical Methods in Biomedical Engineering* 26.5 (2010), pp. 524–533.

[50] Risk, M. R.; Bruno, J. S.; Soria, M. L., et al.: "Measurement of QT interval and duration of the QRS complex at different ECG sampling rates". *Computers in Cardiology* 32.May 2014 (2005), pp. 495–498.

[51] Luz, E. J. d. S.; Schwartz, W. R.; Cámara-Chávez, G., et al.: "ECG-based heartbeat classification for arrhythmia detection: A survey". *Computer Methods and Programs in Biomedicine* 127 (2016), pp. 144–164.

[52] Gayathri, S.; Suchetha, M.; Latha, V.: "ECG arrhythmia detection and classification using relevance vector machine". *Procedia Engineering* 38 (2012), pp. 1333–1339.

[53] Bai, J.; Wang, K.; Liu, Y., et al.: "Computational cardiac modeling reveals mechanisms of ventricular arrhythmogenesis in long QT syndrome type 8: CACNA1C R858H mutation linked to ventricular fibrillation". *Frontiers in Physiology* 8.OCT (2017), pp. 7713389–771.

[54] Kelly, D.; Mackenzie, L.; Hunter, P., et al.: "Proceedings of the Australian Physiological Society (AHMRC) Symposium : Stretch Activated Ion Channels gene expression of stretch-activated channels and mechanoelectric feedback in the heart". *Clinical and Experimental Pharmacology and Physiology* 33 (2006), pp. 642–648.

[55] Konings, M. K.; Jansen, R.; Bosman, L. P., et al.: "Non-invasive measurement of volume-time curves in patients with mitral regurgitation and in healthy volunteers, using a new operator-independent screening tool". *Physiological Measurement* 38.2 (2017), pp. 241–258.

[56] Montalescot, G.; Sechtem, U.; Achenbach, S., et al.: "2013 ESC guidelines on the management of stable coronary artery disease - addenda". *European Heart Journal* 34.38 (2013), pp. 2949–3003.

[57] Nakae, I.; Matsuo, S.; Matsumoto, T., et al.: "Clinical significance of diastolic function as an indicator of myocardial ischemia assessed by 16-frame gated myocardial perfusion SPECT". *Annals of Nuclear Medicine* 22.8 (2008), pp. 677–683.

[58] Zeidan, Z.; Erbel, R.; Barkhausen, J., et al.: "Analysis of global systolic and diastolic left ventricular performance using volume-time curves by real-time three-dimensional echocardiography." *Journal of the American Society of Echocardiography : official publication of the American Society of Echocardiography* 16.1 (2003), pp. 29–37.

[59] Koplan, B. A.; Stevenson, W. G.; Cardiovascular, O. N.: "Ventricular Tachycardia and Sudden Cardiac Death". *Mayo Clinic Proceedings* 84.3 (2009), pp. 289–297.

[60] Farrokhian, A. R.: "Commotio Cordis and Contusio Cordis : Possible Causes of Trauma-Related Cardiac Death". *Arch Trauma Res* 5.4 (2016), pp. 4–5.

[61] Collet, A.: *Numerical modeling of the cardiac mechano-electric feedback within a thermo-electro-mechanical framework Study of its consequences on arrhythmogenesis.* PhD thesis. Wallonia-Europe University Academy, 2015.

[62] Trayanova, N. A.: "Whole-heart modeling : Applications to cardiac electrophysiology and electromechanics". *Circulation Research* 108.1 (2011), pp. 113–128.

[63] Tusscher, K. H. W. J. ten: "Alternans and spiral breakup in a human ventricular tissue model". *AJP: Heart and Circulatory Physiology* 291.3 (Sept. 2006), H1088–H1100.

[64] Cave, D. M.; Gazmuri, R. J.; Otto, C. W., et al.: "Part 7: CPR techniques and devices: 2010 American Heart Association Guidelines for Cardiopulmonary Resuscitation and Emergency Cardiovascular Care". *Circulation* 122.SUPPL. 3 (2010), pp. 720–729.

[65] Langendorf, R.; Pick, A.: "Mechanisms of intermittent ventricular bigeminy. II. Parasystole, and parasystole or re-entry with conduction disturbance." *Circulation* 11.3 (1955), pp. 431–439.

[66] Coumel, P.; Maison-Blanche, P.; Badilini, F.: "Dispersion of Ventricular Repolarization". *Circulation* 97.25 (1998), pp. 2491–2493.

[67] Kohl, P.; Bollensdorff, C.; Morad, M.: "Progress in Biophysics and Molecular Biology of the Beating Heart". *Progress in Biophysics and Molecular Biology* 110.2-3 (2012), pp. 151–153.

[68] Bernardi, L.; Salvucci, F.; Suardi, R., et al.: "Evidence for an intrinsic mechanism regulating heart rate variability in the transplanted and the intact heart during submaximal dynamic exercise?" *Cardiovascular research* 24 (1991), pp. 969–981.

[69] White, E.; Le Guennect, J.-Y.; Nigrettoi, J. M., et al.: "The effects of increasing cell length on auxotonic contractions; membrane potential and intracellular calcium transients in single guinea-pig ventricular myocytes." *Experimental Physiology* 78 (1993), pp. 65–78.